الجمهورية الجزائرية الديمقراطية الشعبية
People's Democratic Republic of Algeria
وزارة التعليم العالي والبحث العلمي
Ministry of Higher Education and Scientific Research
جامعة الشهيد الشيخ العربي التبسي - تبسة

Thesis

Submitted in order to obtain a
Master's degree
Specialization: Mechanical Construction
Field: Mechanical Engineering

Applied Mathematical Methods for Vibration-Based Diagnosis of Rotating Machinery Faults

Presented by :

Labidi Toufik

Thesis Defended on June 9, 2026, Before the Examination Committee Composed of:

President:	DEGHBOUDJ Samir	Pr
Supervisor :	BOUAZIZ Khelifa	MCA
Co-Supervisor :	YOUNES Ramdane	Pr
Examiner :	ALIA Saief eddine	MCB

Academic year :2025/2026

Acknowledgements

First and foremost, I would like to express my deepest gratitude to Allah Almighty for granting me health, strength, patience, and perseverance to successfully complete this work.

I would like to extend my sincere and heartfelt thanks to my supervisor, Mr. BOUAZIZ Khelifa, and my co-supervisor, Mr. YOUNES Ramdane, for their valuable guidance, constant availability, insightful scientific advice, and the trust they placed in me throughout the completion of this dissertation.

I would also like to express my deep gratitude to the President of the jury, Mr. DEGHBOUDJ Samir, as well as to the examiner, Mr. ALIA Saief Eddine, for honoring me by accepting to evaluate this work and for dedicating part of their valuable time to its review and assessment.

Résumé

Les roulements constituent des composants essentiels des machines tournantes, dont la défaillance peut entraîner des arrêts de production coûteux voire des accidents graves. Dans ce travail, deux approches de traitement du signal sont comparées pour le diagnostic des défauts de roulement : la Transformée de Fourier Rapide (FFT) et la Transformée de Hilbert-Huang (HHT). La FFT, bien que largement répandue, présente des limitations intrinsèques face aux signaux non stationnaires et non linéaires. La HHT, fondée sur la Décomposition Modale Empirique (DME) suivie de l'Analyse Spectrale de Hilbert (ASH), constitue une approche entièrement adaptative ne nécessitant aucune base a priori. Les deux méthodes sont appliquées aux signaux vibratoires issus de la base de données de l'Université Case Western Reserve (CWRU) pour un roulement SKF 6205-2RS JEM, dans les conditions à vide et en charge. Les résultats montrent que la HHT offre une meilleure résolution spectrale et une identification plus précise des fréquences caractéristiques de défauts, notamment la visibilité des raies latérales et des harmoniques, par rapport à la FFT classique.

Mots-clés : défauts de Roulement, Transformée de Fourier Rapide (FFT), Transformée de Hilbert-Huang (HHT), Décomposition Modale Empirique (DME), Diagnostic de défauts.

Abstract

Rolling bearings are essential components of rotating machinery, whose failure can lead to costly production downtime or serious accidents. In this work, two signal processing approaches are compared for bearing fault diagnosis: the Fast Fourier Transform (FFT) and the Hilbert-Huang Transform (HHT). Although the FFT is widely used, it has inherent limitations when applied to non-stationary and nonlinear signals. The HHT, based on Empirical Mode Decomposition (EMD) followed by Hilbert Spectral Analysis (HSA), constitutes a fully adaptive approach requiring no a priori basis. Both methods are applied to vibration signals from the Case Western Reserve University (CWRU) bearing database for an SKF 6205-2RS JEM bearing, under no-load and loaded conditions. Results show that the HHT provides better spectral resolution and more accurate identification of fault-characteristic frequencies, particularly in terms of sideband and harmonic visibility, compared to classical FFT.

Keywords: Rolling bearing defect , Fast Fourier Transform (FFT), Hilbert-Huang Transform (HHT), Empirical Mode Decomposition (EMD), Fault diagnosis.

الملخّص

تُعدّ محامل الدوران من المكوّنات الأساسية في الآلات الدوّارة، وقد يؤدّي تعطلها إلى توقّف الإنتاج وحدوث أعطال جسيمة. في هذا العمل، تُجرى مقارنة بين طريقتين لمعالجة إشارات الاهتزاز المستخدمة في تشخيص أعطال المحامل :تحويل فوريه السريع (FFT) وتحويل هيلبرت–هوانغ (HHT) .يتميّز FFT بقدرته على تحليل الإشارات في المجال الترددي بكفاءة عالية، إلا أنه يواجه قيودًا عند التعامل مع الإشارات غير الخطية وغير المستقرة. في المقابل، يعتمد HHT على التحليل التجريبي للنمط (EMD)متبوعًا بـ تحليل طيف هيلبرت(HSA) ، مما يجعله أكثر ملائمة لتحليل الإشارات المعقدة وغير المستقرة.

طُبِّقت الطريقتان على إشارات اهتزاز مستخرجة من قاعدة بيانات Case Western Reserve University (CWRU) لمحمل SKF 6205-2RS JEM في حالتي التشغيل دون حمل وتحت الحمل. وأظهرت النتائج أن HHT يوفّر دقة طيفية أعلى وقدرة أفضل على تحديد الترددات المميّزة لأعطال المحامل، خاصةً في الإشارات غير المستقرة، كما يتيح تمثيلًا أوضح للتغيرات الزمنية–الترددية مقارنةً بتحليل FFT التقليدي. وعليه، يُعدّ HHT أداة أكثر فاعلية لتشخيص أعطال المحامل في البيئات التشغيلية المعقّدة.

الكلمات المفتاحية:
تحويل هيلبرت–هوانغ(HHT) ، تحويل فوريه السريع(FFT) ، أعطال محامل الدوران، تشخيص الأعطال، التحليل التجريبي للنمط(EMD) .

LIST OF FIGURES

Chapter I

Figure I.1. Imbalance types..... 06
Figure I.2. Misalignment types..... 06
Figure I.3. Common defects in a rolling element bearing..... 07
Figure I.4. Some common gear defects..... 07
Figure I.5. Diagnostic pipelines: feature engineering vs. feature learning..... 09

Chapter II

Figure II.1. Example spectrum of a rotating machinery vibration signal..... 14
Figure II.2. Illustration of an oscillatory signal's frequency spectrum..... 16
Figure II.3. Example of a spectrum with a gear defect..... 17
Figure II.4. Example of a Cepstrum..... 18
Figure II.5. Example of an Envelope Spectrum..... 20
Figure II.6. FFT analysis – imbalance defect..... 21
Figure II.7. FFT of angular misalignment..... 21
Figure II.8. Angular misalignment..... 22
Figure II.9. FFT of parallel misalignment..... 22
Figure II.10. Parallel misalignment..... 23
Figure II.11. FFT of small defects in the raceways of bearing..... 25
Figure II.12. FFT of an obvious wear in the form of pits..... 25
Figure II.13. FFT of clearly visible wear over the breadth of the bearing..... 26
Figure II.14. Severely damaged bearing in final stage of wear..... 27
Figure II.15. Normal vibration spectrum of gears..... 28
Figure II.16. Vibration spectrum of gear tooth wear..... 29
Figure II.17. Vibration spectrum of gear tooth load..... 29
Figure II.18. Vibration spectrum of gear eccentricity + backlash..... 30
Figure II.19. Vibration spectrum of gear misalignment..... 31
Figure II.20. Time waveform of a cracked or broken gear tooth..... 31

Figure II.21. Vibration spectrum of gear hunting problem..... 33

Chapter III

Figure III.1. Principle of estimation of instantaneous frequency and amplitude via analytic signal..... 44
Figure III.2. Block diagram of the DHT computation algorithm..... 46
Figure III.3. Computation of the analytic signal for a sinusoidal signal..... 47
Figure III.4. Composite test signal x(t) used to illustrate the EMD algorithm..... 50
Figure III.5. The three sinusoidal components constituting the test signal..... 50
Figure III.6. Upper envelope, lower envelope, and local mean of the test signal..... 51
Figure III.7. Sifting process iteration 0..... 51
Figure III.8. Three successive sifting iterations for extraction of IMF_1..... 52
Figure III.9. Representation of IMF1..... 53
Figure III.10. Representation of the residue after extraction of IMF1..... 53
Figure III.11. All IMFs and the final residue of the signal x(t)..... 54
Figure III.12. Upper and lower envelopes and the mean of a signal..... 54

Chapter IV

Figure IV.1. Bearing test rig..... 58
Figure IV.2. Sensor placement positions..... 59
Figure IV.3. Vibration signals for healthy and defective bearings..... 60
Figure IV.4. Geometric characteristics of a rolling bearing..... 61
Figure IV.5. Spectrum of the healthy bearing (no-load) with characteristic fault frequencies..... 64
Figure IV.6. Spectrum of the bearing with outer race fault (no-load), diameter 0.178 mm..... 65
Figure IV.7. Spectrum of the bearing with inner race fault (no-load), diameter 0.178 mm..... 65
Figure IV.8. Spectrum of the healthy bearing under 3 HP load..... 66
Figure IV.9. Spectrum of the bearing with outer race fault under 3 HP load, diameter 0.356 mm..... 67

Figure IV.10. Spectrum of the bearing with inner race fault under 3 HP load, diameter 0.356 mm..... 68
Figure IV.11. IMFs of the healthy bearing signal..... 69
Figure IV.12. IMFs of the inner race fault signal..... 69
Figure IV.13. IMFs of the outer race fault signal (6 o'clock position)..... 70
Figure IV.14. Hilbert spectrum of IMF1 – healthy bearing..... 71
Figure IV.15. Hilbert spectrum of IMF2 – healthy bearing..... 72
Figure IV.16. Hilbert spectrum of IMF1 – inner race fault 0.178 mm (no-load)..... 72
Figure IV.17. Hilbert spectrum of IMF2 – inner race fault 0.178 mm (no-load)..... 73
Figure IV.18. Hilbert spectrum of IMF1 – outer race fault 0.178 mm (no-load)..... 73
Figure IV.19. Hilbert spectrum of IMF2 – outer race fault 0.178 mm (no-load)..... 74
Figure IV.20. Hilbert spectrum of IMF1 – inner race fault 0.356 mm (3 HP)..... 74
Figure IV.21. Hilbert spectrum of IMF2 – inner race fault 0.356 mm (3 HP)..... 75
Figure IV.22. Hilbert spectrum of IMF1 – outer race fault 0.356 mm (3 HP)..... 75
Figure IV.23. Hilbert spectrum of IMF2 – outer race fault 0.356 mm (3 HP)..... 76

LIST OF TABLES

Chapter I

Table I.1. Advantages and disadvantages of classical and advanced approaches..... 09

Chapter II

Table II.1. Fault detection methods comparison..... 15

Chapter III

Table III.1. Standard Hilbert Transform pairs..... 44
Table III.2. EMD sifting process algorithm..... 49
Table III.3. Comparative analysis: Fourier, Hilbert, and HHT methods..... 55

Chapter IV

Table IV.1. Bearing characteristics of SKF 6205-2RS JEM..... 62
Table IV.2. Characteristic frequencies of the SKF 6205-2RS JEM bearing..... 62
Table IV.3. Theoretical and experimental values (no-load), fault diameter 0.178 mm.. 68
Table IV.4. Theoretical and experimental values under load (3 HP), fault diameter 0.356 mm..... 61
Table IV.5. Bearing fault frequencies used for HHT analysis..... 71
Table IV.6. Comparative results: FFT vs. HHT..... 77

TABLE OF CONTENTS

Acknowledgements..... i
Résumé..... ii
Abstract..... iii
ملخص..... iv
List of Figures..... v
List of Tables..... viii
Table of contents..... ix
List of Symbols xii
Abbreviations..... xiv
General introduction..... 1

CHAPTER I

I.1 Introduction..... 4
I.2 Generalities on Rotating Machinery..... 5
I.3 Typical Faults in Rotating Machinery..... 5
I.3.1 Imbalance..... 5
I.3.2 Misalignment..... 6
I.3.3 Bearing defects..... 7
I.3.4 Gear defects..... 7
I.3.5 Mechanical looseness..... 7
I.3.6 Shaft cracks..... 8
I.4 Condition-Based and Predictive Maintenance..... 8
I.5 Classical Approaches vs. Advanced Approaches..... 8
I.6 Recent Works on Vibration Analysis..... 10
I.7 Conclusion..... 11

CHAPTER II

II.1 Introduction 13
II.2 Fundamentals of Mechanical System Dynamics..... 14
II.3 Fundamentals of Vibration Analysis..... 15
II.3.1. Vibration Signals (Time Domain / Frequency Domain)..... 15
II.3.2. Fourier Transform (FFT)..... 16
II.3.3. Spectral Analysis..... 16

II.3.4. Cepstrum Analysis..... 17
II.3.5. Time-Frequency Analysis (Wavelet Transform)..... 18
II.4 Vibration Indicators for Fault Detection..... 18
II.4.1 RMS (Root Mean Square)..... 19
II.4.2 Kurtosis..... 19
II.4.3 Crest Factor..... 19
II.4.4 Envelope Spectrum..... 19
II.5 Vibration Signatures of Main Faults..... 20
II.5.1 Imbalance signature..... 20
II.5.2 Misalignment signature..... 21
II.5.3 Bearing fault signature..... 23
II.5.4 Gear fault signature..... 27
II.6. Conclusion..... 33

CHAPTER III

III.1 Introduction..... 35
III.2 Signal Representation and Mathematical Framework..... 36
III.3 Mathematical Modeling of Machinery Systems..... 36
III.4 Classical Signal Analysis: Fourier-Based Methods..... 37
III.4.1 Fourier Transform..... 37
III.4.2 Discrete Fourier Transform and FFT..... 39
III.4.3 Time–Frequency Analysis (STFT)..... 40
III.4.4 Wavelet Transform (CWT)..... 41
III.5 Hilbert Transform and Analytic Signal..... 41
III.5.1 Definition of the Hilbert Transform..... 41
III.5.2 Instantaneous Features..... 44
III.5.3 Applications in Fault Diagnosis – Envelope Detection..... 45
III.5.4 Discrete Hilbert Transform..... 46
III.6 The Hilbert–Huang Transform (HHT)..... 47
III.6.1 Motivation..... 47
III.6.2 Empirical Mode Decomposition and Hilbert Spectral Analysis..... 48
III.6.3 The Hilbert Spectrum..... 55
III.7 Conclusion..... 56

CHAPTER IV

IV.1 Introduction..... 57

IV.2 Bearing Under Study: SKF 6205..... 58
IV.3 Bearing System Under Study..... 58
IV.3.1 Bearing Data Center – Bearing Test Rig..... 58
IV.3.2 Dataset Construction..... 60
IV.4 Analysis Methods..... 61
IV.4.1 Frequency-Domain Descriptors..... 61
IV.5 Characterization of Spectral Signatures of Bearing Faults..... 62
IV.5.1 Spectral Signature of the Healthy Bearing (No-Load)..... 63
IV.5.2 Spectral Signature of the Outer Race Fault..... 64
IV.5.3 Spectral Signature of the Inner Race Fault..... 65
IV.5.4 Spectral Signature of the Healthy Bearing Under Load (3 HP)..... 66
IV.5.5 Spectral Signature of the Outer Race Fault Under Load (3 HP)..... 67
IV.5.6 Spectral Signature of the Inner Race Fault Under Load (3 HP)..... 67
IV.6 Fault Signal Analysis Using the Hilbert–Huang Method..... 68
IV.6.1 Fault Signature Evaluation via the Hilbert Spectrum..... 70
IV.7 Conclusion..... 75
General Conclusion..... 76
References……..... 77

LIST OF SYMBOLS

Symbol	Description
X(t)	Vibration déplacement signal
X(f)	Fourier spectrum of x(t)
F	Frequency
Fr	Shaft rotationnel frequency
ω	Angular frequency
ωn	Natural angular frequency
M	Mass
C	Damping coefficient
K	Stiffness
F(t)	External excitation force
fs	Sampling frequency
N	Number of FFT samples
Δf	Frequency resolution
BPFI	Ball Pass Frequency – Inner Race
BPFO	Ball Pass Frequency – Outer Race
BSF	Ball Spin Frequency
FTF	Fundamental Train Frequency (cage)
Nb	Number of rolling elements
Bd	Ball/roller diameter
Pd	Bearing pitch diameter
θ	Contact angle
y(t)	Hilbert Transform of x(t)
z(t)	Analytic signal
a(t)	Instantaneous amplitude (envelope)
θ(t)	Instantaneous phase
ω(t)	Instantaneous frequency
H(ω,t)	Hilbert spectrum
h(ω)	Marginal Hilbert spectrum

IMF	Intrinsic Mode Function
cj(t)	j-th IMF component
rn(t)	Final EMD residue
emax(t)	Upper envelope
emin(t)	Lower envelope
m(t)	Local mean envelope
ε	EMD stopping criterion threshold (≈ 0.2)
W(a,b)	Continuous Wavelet Transform coefficient
a	Wavelet scale parameter
b	Wavelet translation parameter
Pk	Power Spectral Density coefficient
Af	Spectral amplitude descriptor at frequency f
GMF	Gear Mesh Frequency
RMS	Root Mean Square

Abbreviations

Abbreviation	Full Term
CBM	Condition-Based Maintenance
CNN	Convolutional Neural Network
CWRU	Case Western Reserve University
CWT	Continuous Wavelet Transform
DFT	Discrete Fourier Transform
DHT	Discrete Hilbert Transform
EDM	Electrical Discharge Machining
EEMD	Ensemble Empirical Mode Decomposition
EMD	Empirical Mode Decomposition
FFT	Fast Fourier Transform
HHT	Hilbert–Huang Transform
HSA	Hilbert Spectral Analysis
HT	Hilbert Transform
IFT	Inverse Fourier Transform
IMF	Intrinsic Mode Function
LSTM	Long Short-Term Memory (neural network)
PdM	Predictive Maintenance
PSD	Power Spectral Density
RMS	Root Mean Square
RUL	Remaining Useful Life
SDOF	Single Degree of Freedom
STFT	Short-Time Fourier Transform
SVM	Support Vector Machine
WVD	Wigner–Ville Distribution

General introduction

Rotating machinery (including electric motors, pumps, compressors, turbines, and gearboxes) constitutes the backbone of modern industrial infrastructure. Their continuous and reliable operation is critical to productivity, safety, and economic efficiency. Among the various components that make up these machines, rolling element bearings are among the most frequently failing, accounting for a significant proportion of unplanned downtime in industrial facilities. Early detection of bearing faults before they propagate to catastrophic failure is therefore a major challenge in the field of condition monitoring and predictive maintenance.

Vibration analysis is the most widely used diagnostic modality for rotating machinery, owing to its sensitivity to incipient mechanical faults and the wealth of physical information contained in vibration signals. When a localized defect is present on a bearing race or rolling element, it generates a series of periodic impulses at characteristic frequencies that can be identified in the vibration spectrum. The classical approach to spectral analysis is the Fast Fourier Transform (FFT), which decomposes a signal into its constituent sinusoidal components and provides a global frequency representation. The FFT has been extensively validated in industrial practice and remains the standard tool in most condition monitoring systems.

However, the FFT rests on the assumption that the analyzed signal is stationary, its statistical properties do not change over time. Bearing vibration signals, particularly those generated by faults under variable-speed or variable-load conditions, are inherently non-stationary and nonlinear. Under such conditions, the FFT introduces artefacts such as spectral leakage and spurious harmonics, which can mask or distort the fault signatures. This fundamental limitation motivates the search for signal processing methods that are better adapted to non-stationary signals.

Several time–frequency analysis methods have been proposed to address this limitation, including the Short-Time Fourier Transform (STFT), the Continuous Wavelet Transform (CWT), and the Wigner–Ville Distribution (WVD). While each of these methods offers improvements over the FFT in specific respects, they all rely on predefined basis functions that are not intrinsic to the signal being analyzed. The STFT is constrained by a fixed time–frequency resolution; the CWT requires the prior selection of a mother wavelet; and the WVD suffers from cross-term interference in multi-component signals.

The Hilbert–Huang Transform (HHT), introduced by Huang et al. in 1998, represents a fundamentally different approach. It consists of two stages: Empirical Mode Decomposition

(EMD), which adaptively decomposes any signal into a set of Intrinsic Mode Functions (IMFs) that are intrinsic to the signal itself and require no predefined basis; and Hilbert Spectral Analysis (HSA), which applies the Hilbert Transform to each IMF to compute its instantaneous frequency and amplitude as functions of time. The resulting Hilbert spectrum provides a fully adaptive time–frequency–energy representation that is particularly well suited to nonlinear and non-stationary signals.

The objective of this work is to study the HHT method in depth and to evaluate its performance for rolling bearing fault diagnosis, in direct comparison with the classical FFT approach. The experimental validation is carried out using real vibration signals from the publicly available Case Western Reserve University (CWRU) Bearing Data Center, which has become the standard benchmark in the bearing fault diagnosis community. Signals corresponding to healthy bearings and bearings with outer race and inner race faults of different severity levels, under no-load and loaded operating conditions, are analyzed.

This dissertation is organized into four chapters. Chapter I presents the general context of rotating machinery fault diagnosis: the main fault types affecting induction motors and their causes, the statistical distribution of failure modes, and an overview of classical and advanced diagnostic methods, concluding with a critical review of recent works comparing FFT-based and HHT-based approaches. Chapter II establishes the theoretical foundations of vibration signal analysis, covering time-domain and frequency-domain indicators, the FFT and its limitations, and the main time–frequency analysis tools used as references. Chapter III develops the complete mathematical framework of the HHT: the Hilbert Transform and analytic signal, the Fourier Transform and its properties, the Short-Time Fourier Transform, the Continuous Wavelet Transform, the EMD algorithm with its stopping criteria and properties, and the Hilbert Spectral Analysis. Chapter IV presents the experimental application of both methods to the CWRU bearing dataset, providing a direct quantitative comparison of their fault detection performance.

Chapter I

Literature Review and Generalities on Rotating Machinery

I.1 Introduction

Rotating machinery plays a central role in modern industrial systems. Its performance and reliability directly affect productivity, safety, and maintenance costs. As industrial systems become more complex, ensuring the proper functioning of these machines has become increasingly important.

I.2 Generalities on Rotating Machinery

Rotating machines in this broad sense are devices like motors, generators, turbines, pumps and gearboxes that convert electrical energy to and from mechanical energy (and transmit power through shafts, gears and bearings). These machines are crucial in the applications of manufacturing, transportation, energy system such as wind, wave, and tidal energy as well as modern electric drives. An assembly generally consists of rotor (the shaft to be rotated and the parts mounted on the rotating shaft), a stator, bearings, couplings and sometimes one or several gear stages. These machines play a critical role in safety, productivity and maintenance costs, and their reliability and availability highly affect both [1]**.**

I.3 Typical Faults in Rotating Machinery

There are several fault types that remain the most critical and the most studied in both mechanical and electrical rotating machinery, and the following are the most fault [1] :

I.3.1. Imbalance

Imbalance occurs when the rotor's mass center does not coincide with its axis of rotation, generating a synchronous centrifugal force. It is widely recognized as the most common rotodynamic fault. In vibration spectra, imbalance generally manifests at 1× rpm [3].

There are two new terminologies used: one is rotating centerline and the other is geometric centerline. The rotating centerline is defined as the axis about which the rotor would rotate if not constrained by its bearings (also called the principal inertia axis or PIA). The geometric centerline (GCL) is the physical centerline of the rotor. When the two centerlines are coincident, then the rotor will be in a state of balance. When they are apart, the rotor will be Imbalanced. There are three types of imbalances that can be encountered on machines, and these are [4]:

a: Static imbalance: (PIA and GCL are parallel)
b: Couple imbalance: (PIA and GCL intersect in the center)
c: Dynamic imbalance: (PIA and GCL do not touch or coincide).

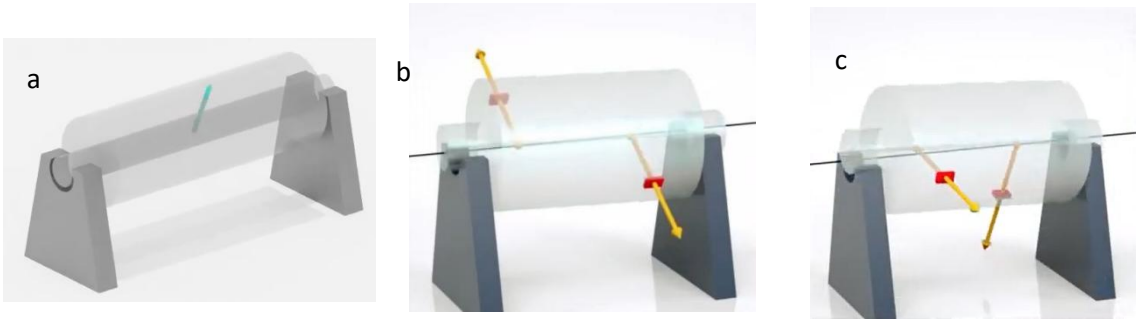


Figure I.1. Imbalance types [2]

I.3.2. Misalignment

Shaft misalignment (whether parallel, angular, or combined) can arise from installation errors, thermal expansion, wear, or insufficient maintenance. It is recognized as a major contributor to machine downtime, with studies estimating that nearly 30% of failures are linked to improper alignment. Misalignment leads to increased bearing loads and elevated vibration levels, typically observed at the fundamental rotational frequency (1×), its second harmonic (2×), and higher-order harmonics. These harmonics, defined as integer multiples of the fundamental frequency, originate from the nonlinear dynamic response of the system and are commonly used as diagnostic indicators of misalignment severity. Additionally, prolonged misalignment accelerates wear in couplings, gears, and bearings [3].

The different forms of shaft misalignment described previously are schematically illustrated in Figure I.2 highlighting parallel, angular, and combined misalignment configurations.

a : Parallel Misalignment

b : Angular Misalignment

c : Combined Misalignment

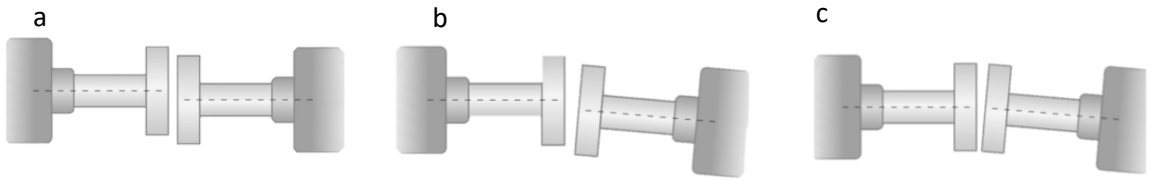


Figure I.2. Misalignment types

I.3.3. Bearing defects

Rolling element bearings constitute essential support components and are among the most frequently failing parts of rotating machinery. Common faults include spalls and cracks on the

inner or outer races or rolling elements, lubrication failures, contamination, and changes in. These faults generate characteristic impulsive vibration signatures and fault frequencies, which are extensively analyzed using advanced signal processing techniques, such as empirical mode decomposition and kurtogram-based methods clearance [6].

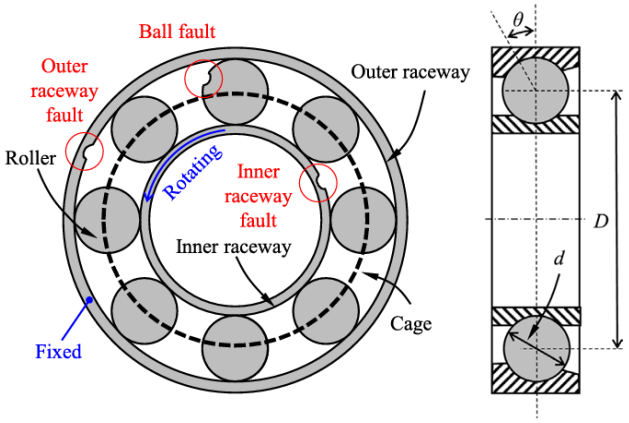


Figure I.3. Common defects in a rolling element bearing [4]

I.3.4. Gear defects

In geared drives, gearboxes are a common source of failure. Typical gear problems include worn, cracked, broken, or chipped teeth, as well as eccentricity and misalignment. These issues are often caused by overloading, poor lubrication, contamination, or errors in manufacturing or installation, as well as fatigue. Each type of fault shows a distinct vibration pattern that can be observed at the gear and shaft rotation frequencies. [3].

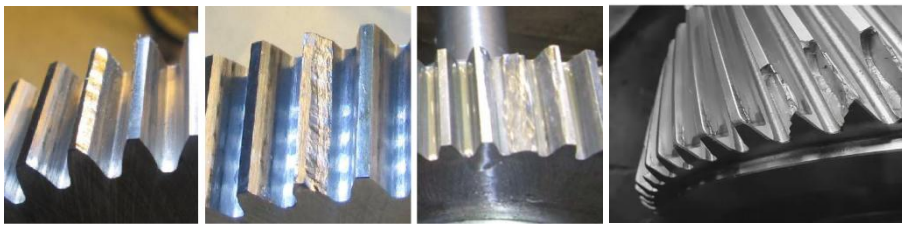


Figure I.4. Some common gears defects [17]

I.3.5. Mechanical looseness

Excessive mechanical clearances and looseness in components such as bearings, housings, foundations, or couplings can cause non-linear contact, intermittent impacts, and increased broadband vibration. Rotor-to-stator rubbing and structural looseness are considered key additive or multiplicative faults, and they often occur alongside imbalance or misalignment. If these faults go undetected, they can quickly lead to severe damage [5].

I.3.6. Shaft cracks

Shaft cracks, whether on the surface or across the shaft, reduce stiffness and cause a “breathing” motion when rotating. This leads to subharmonic and superharmonic vibration components. Although less common than imbalance or misalignment, shaft cracks are severe faults that can quickly lead to catastrophic failure [9].

I.4 Condition-Based and Predictive Maintenance

Condition-Based Maintenance (CBM) is based on regularly checking the actual condition of a machine using measurements such as vibration, electric current, and temperature. Instead of performing maintenance at fixed time intervals, maintenance is carried out only when these measurements show clear signs of deterioration beyond set limits. This approach helps ensure that maintenance is done only when necessary, avoiding both early and late interventions [6].
Predictive Maintenance (PdM) builds on this idea but goes a step further. It uses collected data and analytical tools to predict how a fault will develop in the future and to estimate how long the equipment can continue operating safely (Remaining Useful Life). This allows maintenance teams to plan repairs in advance, reduce unexpected breakdowns, and lower overall costs [7].

I.5 Classical approaches vs advanced approaches

Fault detection in signal processing has progressively evolved from traditional, expert-driven methodologies to data-driven machine learning and deep learning paradigms. Classical approaches typically rely on domain knowledge to manually extract discriminative features using time-domain, frequency-domain, or time–frequency analysis techniques such as FFT and wavelet transforms. These handcrafted features are subsequently processed by conventional classifiers, including support vector machines (SVM) and decision tree–based models. Such methods remain attractive due to their interpretability, lower data requirements, and solid theoretical grounding. However, their performance strongly depends on expert feature engineering and may degrade in the presence of non-stationary signals, high noise levels, or multiple concurrent faults [8].

In contrast, modern approaches rely on machine learning Figure I.5, especially deep learning models such as CNNs, LSTMs, and Transformers. Instead of manually designing features, these models learn useful patterns directly from raw or lightly processed data. In many experimental studies, they achieve very high fault detection accuracy, sometimes above 97–99% under

controlled conditions. They are also better at handling complex fault types, changing operating conditions, and combining data from multiple sensors [8].

However, these methods usually require large amounts of labeled data to work reliably. They can also be harder to interpret, meaning it is not always easy to understand how or why the model reached a specific decision compared to classical methods Table I.1[8].

Approach	Advantages	Disadvantages
Classical approaches	Interpretable; works with small datasets; low computational cost	Needs expert feature design; struggles with complex/multifault data
advanced approaches	High accuracy; automatic feature extraction; handles complex/multimodal data	Requires large labeled datasets; less interpretable; higher compute

Table I.1. Advantages and Disadvantages of the Classical and advanced approaches

Overall, comparative studies indicate that deep learning–based methods generally outperform traditional techniques in terms of accuracy [9], scalability, and robustness across diverse fault types. Despite these advancements, significant challenges remain, particularly regarding data efficiency, model explainability, standardization of evaluation benchmarks, and deployment reliability in real-world industrial environments. This review therefore synthesizes the theoretical foundations, methodological developments, strengths, limitations, and comparative performance characteristics of both classical and modern fault detection paradigms.

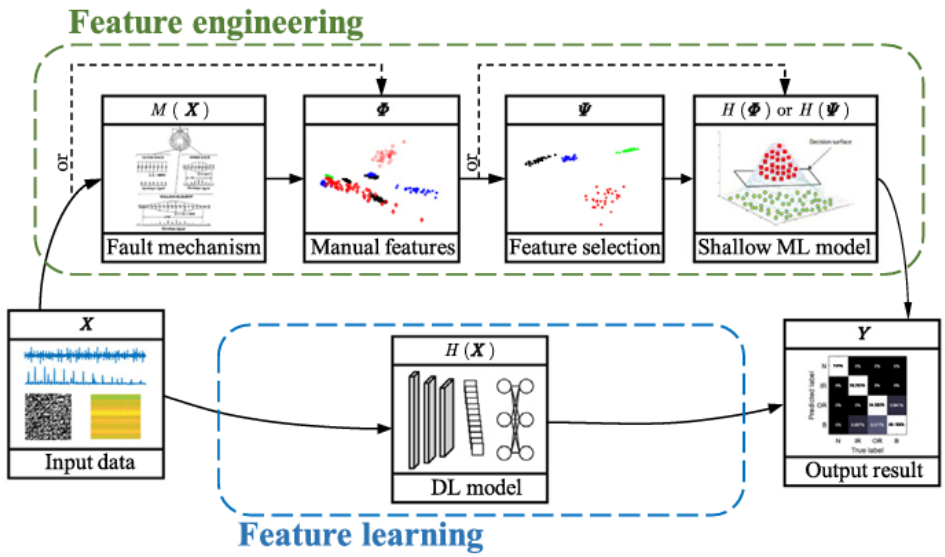


Figure I.5. Diagram of the two diagnostic pipelines : "feature engineering" and "feature learning" [4]

I.6 Recent works on vibration analysis

The studies examined in this section collectively map the current state of vibration-based fault diagnosis, from broad methodological surveys to focused comparisons between classical spectral analysis and modern data-driven approaches. Although they differ in scope and methodology, a common thread emerges: classical FFT-based techniques remain interpretable and computationally efficient, but their performance degrades significantly under non-stationary or noisy conditions. Deep learning models consistently outperform them in accuracy, yet at the cost of requiring large labelled datasets and reduced physical interpretability. This observation directly motivates the present work, which investigates whether adaptive time–frequency decomposition via HHT can bridge the gap between the two paradigms (retaining physical interpretability while improving robustness to non-stationarity) .

Abdullah et al. (2025) [14] provide a comprehensive survey of machine learning methods for rotating machinery fault diagnosis. While their findings confirm that deep learning models (CNN, LSTM, ResNet) achieve diagnostic accuracy up to 99.5%, they explicitly acknowledge that such performance is obtained under controlled laboratory conditions with balanced datasets. The review does not address the case of non-stationary or variable-speed signals — precisely the conditions under which classical FFT analysis is known to underperform and for which HHT-based decomposition is designed. This gap supports the methodological choice made in the present work.

Ahmad et al. (2024) [16] propose a graph convolutional network architecture for machine fault diagnosis that exploits spatial dependencies among sensor channels. Their experimental results on the CWRU bearing dataset (the same benchmark used in the present work) demonstrate improved generalization under variable-speed conditions compared to standard CNN baselines. While the model achieves high accuracy, it requires structured multi-sensor input and substantial training data. By contrast, the HHT-based approach adopted in this study operates on single-channel signals with no training phase, making it directly applicable to cases where labelled data are scarce or unavailable.

Saeed et al. (2024) [17] investigate bearing fault diagnosis under variable load conditions using convolutional neural networks combined with transfer learning. Their approach achieves strong classification accuracy on the CWRU dataset with limited labelled samples from the target domain. However, the study does not compare its results against signal-adaptive time–frequency methods such as HHT, leaving open the question of whether the observed performance gains arise from the learning architecture itself or from the implicit time–frequency decomposition performed

by the convolutional layers. This distinction motivates the explicit physical analysis pursued in the present work.

A second body of literature specifically addresses the comparison between FFT-based spectral analysis and HHT-based adaptive decomposition for rotating machinery fault diagnosis. Lei et al. [6] systematically reviewed thirty-one published studies applying EMD and HHT to bearing, gear, and rotor fault detection, and concluded that HHT consistently outperforms FFT in non-stationary and nonlinear signal environments by eliminating the spurious harmonics inherent to Fourier analysis. Feng et al. [46] further demonstrated, on both simulated and experimental bearing signals, that the Hilbert marginal spectrum derived from HHT localizes fault-characteristic frequency components with sharper spectral resolution than classical FFT, particularly under variable-speed and mixed-fault conditions. These findings are directly relevant to the present work and provide the comparative benchmark against which the experimental results of Chapter IV are interpreted.

I.7. Conclusion

This chapter established the theoretical and contextual foundations required for the subsequent analysis. The main categories of rotating machinery faults (imbalance, misalignment, bearing defects, gear damage, and mechanical looseness) were presented together with their characteristic vibration signatures, which constitute the physical basis for diagnostic feature extraction.

The literature review showed that deep learning-based approaches consistently achieve higher diagnostic accuracy than classical signal-processing methods, but at the cost of requiring large labelled datasets and reduced physical interpretability. Crucially, their performance advantages are most pronounced under stationary, controlled laboratory conditions; under non-stationary or variable-load operating regimes, the gap narrows considerably. The reviewed comparative studies [48, 49] further demonstrate that adaptive time–frequency decomposition via the Hilbert–Huang Transform (HHT) offers a physically interpretable alternative that is inherently suited to non-stationary signals, without requiring any prior labelling or training.

These conclusions motivate the methodological choice made in this work. Chapter II establishes the theoretical foundations of vibration signal analysis and introduces the classical spectral tools against which HHT will be benchmarked. Chapter III develops the mathematical framework of the HHT, covering Empirical Mode Decomposition (EMD) and Hilbert Spectral Analysis (HSA). Chapter IV then applies both methods to real bearing vibration signals from the CWRU dataset, enabling a direct experimental comparison of their fault detection capability under realistic operating conditions.

Chapter II

Theoretical Study of Vibration Analysis

II.1 Introduction

Building on the fault taxonomy and diagnostic context established in Chapter I, this chapter develops the theoretical foundations required for vibration-based fault diagnosis. It first introduces the fundamentals of mechanical system dynamics, showing how mass, stiffness, and damping govern the vibration response of rotating machines. The chapter then presents the principal signal analysis techniques, including time-domain and frequency-domain representations, the Fast Fourier Transform (FFT), spectral and cepstrum analysis, as well as wavelet-based time–frequency methods. Subsequently, the main scalar vibration indicators — such as RMS, kurtosis, crest factor, and the envelope spectrum — are described. Finally, the vibration signatures associated with the principal fault categories, namely imbalance, misalignment, bearing defects, and gear faults, are characterized. These elements collectively provide the diagnostic reference framework for the theoretical and experimental analyses carried out in the subsequent chapters.

II.2. Fundamentals of Mechanical System Dynamics

Mechanical vibrations are oscillatory motions of mechanical systems about an equilibrium position, caused by external excitations or initial disturbances. In practice, real machines can be modeled as lumped-parameter systems consisting of masses, stiffnesses, and damping elements, which lead to equations of motion describing the evolution of displacement, velocity, and acceleration over time [10].

These dynamic behaviors are governed by key concepts such as single- and multi-degree-of-freedom systems, natural frequencies, mode shapes, and various damping mechanisms, including viscous, Coulomb, and structural damping. Together, these parameters determine how mechanical systems respond under free and forced vibration conditions [10].

Within the context of condition monitoring, machine behavior is generally assumed to be linear around its operating point. This simplifying assumption allows the vibration response to be directly associated with excitation forces and the presence of faults, making vibration signals highly informative for diagnostic purposes [10].

Consequently, condition monitoring of rotating machinery relies on multiple diagnostic techniques, each providing specific insights into machine health. Parameters such as temperature, pressure, flow rate, and oil analysis can indicate certain types of degradation; however, their diagnostic capability is often limited to specific fault categories. In contrast, vibration analysis provides a more comprehensive representation of machine dynamics and remains the most sensitive and effective technique for detecting a wide range of mechanical faults.

To illustrate this, the following Table II.1. presents a comparative overview of common fault types and the monitoring techniques capable of detecting them.

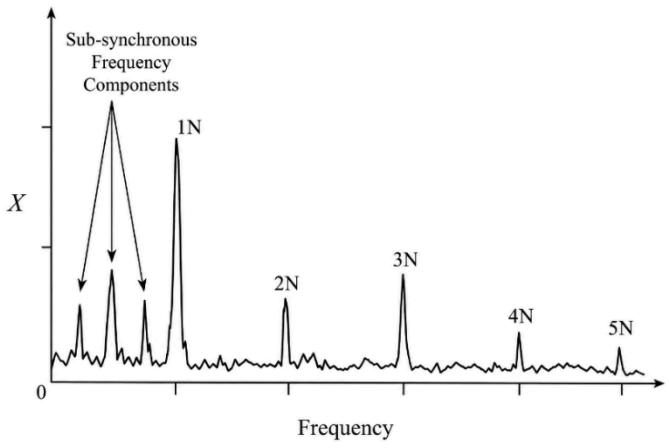


Figure II.1.Example spectrum of a rotating machinery vibration signal [24].

Fault Type	Temperature	Pressure	Flow	Oil Analysis	Vibration
Imbalance					X
Misalignment / Bent shaft	X				X
Damaged rolling element bearings	X			X	X
Damaged journal bearings	X	X	X	X	X
Damaged or worn gears				X	X
Mechanical looseness					X
Noise					X
Cracking					X

Table II.1. Fault Detection Methods Comparison [11].

As shown in the Table II.1 [11], vibration analysis stands out as the most versatile diagnostic tool, as it is capable of detecting nearly all major mechanical faults. This is due to its direct relationship with the dynamic response of the machine.

In contrast, other monitoring techniques (such as temperature, pressure, flow, and oil analysis) are generally limited to specific fault mechanisms and may fail to provide early or comprehensive detection. Therefore, vibration analysis plays a central role in modern condition-based and predictive maintenance strategies, enabling early fault identification, improving system reliability, and reducing maintenance costs.

II.3 Fundamentals of Vibration Analysis

Vibration analysis interprets measured motion to infer system condition. It relies on representing signals in different domains, each revealing specific information.

II.3.1. Vibration signals (time domain / frequency domain)

- **A time-domain signal**

Shows vibration amplitude versus time and reflects the overall transient behavior, impacts, and non-stationary events, but individual excitation sources are hard to separate [12].

- **A frequency-domain spectrum**

shows amplitude versus frequency and is obtained from the time signal using the Fast Fourier Transform (FFT). It displays discrete peaks at characteristic frequencies, which are crucial for identifying specific faults such as imbalance, misalignment, and bearing or gear defects [13].

II.3.2. Fourier Transform (FFT)

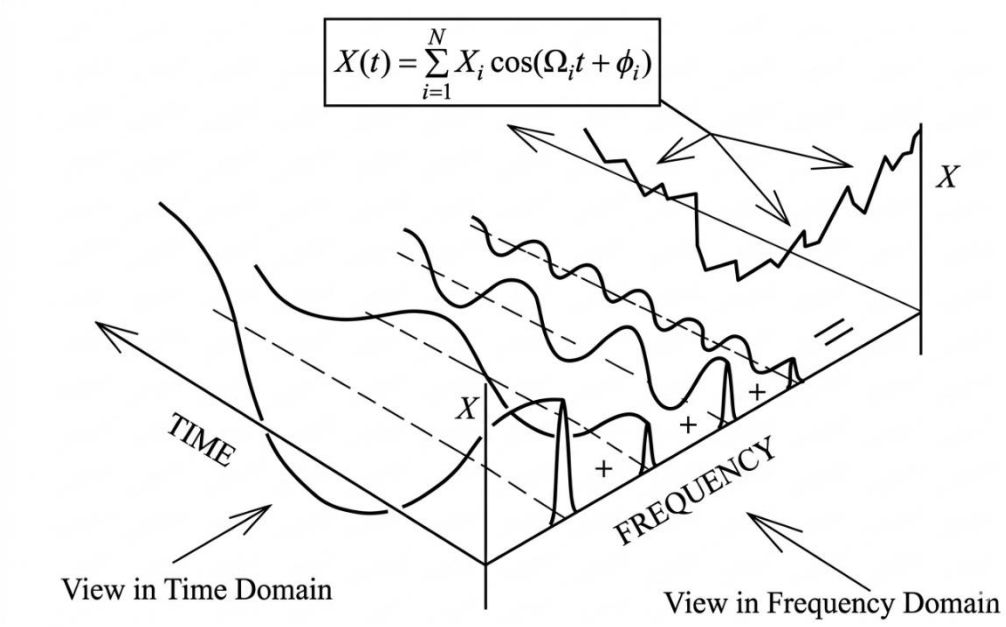


Figure II.2. Illustration of an oscillatory signal's frequency spectrum [24].

The Fourier Transform decomposes a signal into sinusoidal components providing its frequency content. In practice, the Discrete Fourier Transform is implemented efficiently as the FFT, enabling real-time spectral analysis in condition monitoring systems. FFT-based spectra and envelope spectra are standard tools for diagnosing rotating machinery and for deriving velocity and displacement from acceleration via frequency-domain integration [22].

II.3.3. Spectral analysis

Spectral analysis uses FFT and related tools to examine frequency content, harmonics, sidebands, and broadband components. It is fundamental for detecting periodic excitations, gear mesh frequencies, bearing defect frequencies, and resonance phenomena. High-resolution spectral methods can further enhance separation of closely spaced lines in complex machines [22].

In Figure II.3. the acceleration spectrum measured at bearing 3 of the gearboxes in the axial direction within the frequency band [0–25600 Hz]. The spectrum shows the appearance of the gear meshing frequency Fe = 6125 Hz and its harmonics 2Fe = 12250 Hz and 3Fe = 18375 Hz.

Based on zones 1 and 2, the sidebands presence around the meshing frequency and its harmonics, corresponding to the input shaft frequency of the gearbox Fr1 = 150 Hz and the output

shaft frequency Fr2 = 25 Hz. This indicates the presence of a defect in the teeth of the gear and the pinion. The decrease in the amplitudes of Fe and its harmonics 2Fe and 3Fe confirms the presence of gear tooth wear.

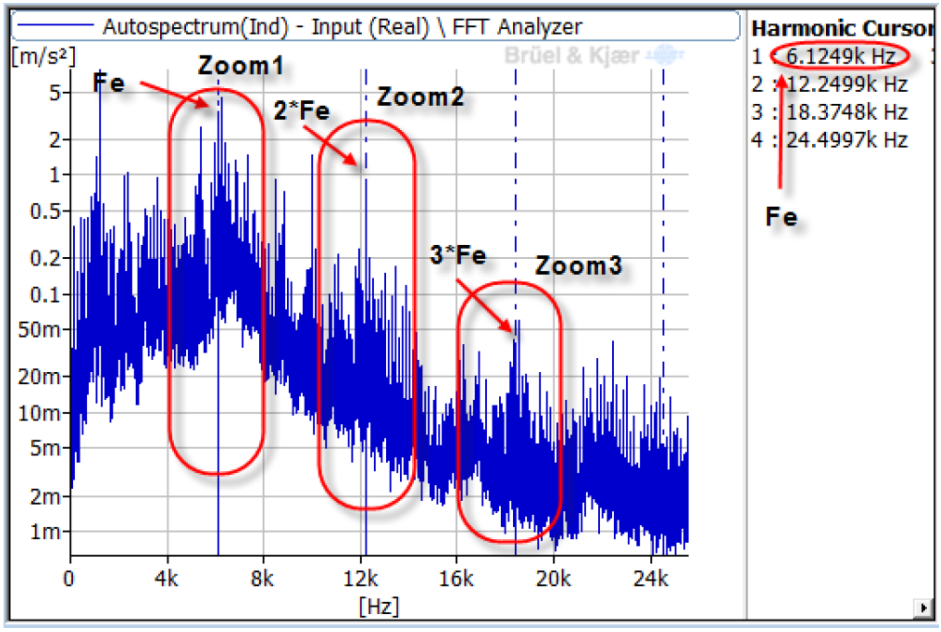


Figure II.3. Example of a spectrum with a gear defect.

II.3.4. Cepstrum analysis

Cepstrum analysis is obtained by applying the inverse Fourier Transform to the logarithm of the power spectrum. This approach is particularly useful for detecting weak periodic structures, such as sidebands generated by modulation in gearboxes, where overlapping components may obscure patterns in the original spectrum. By effectively “compressing” families of sidebands into single peaks at specific quefrencies, cepstrum analysis facilitates the identification of fault-related periodicities [22].

The Cepstrum representation of the same signal in Figure II.4. clearly shows the appearance of the two harmonic families of the input and output frequencies of the gearbox, with a decreasing comb pattern of these harmonics, which confirms the presence of a defect in the gear and pinion teeth.

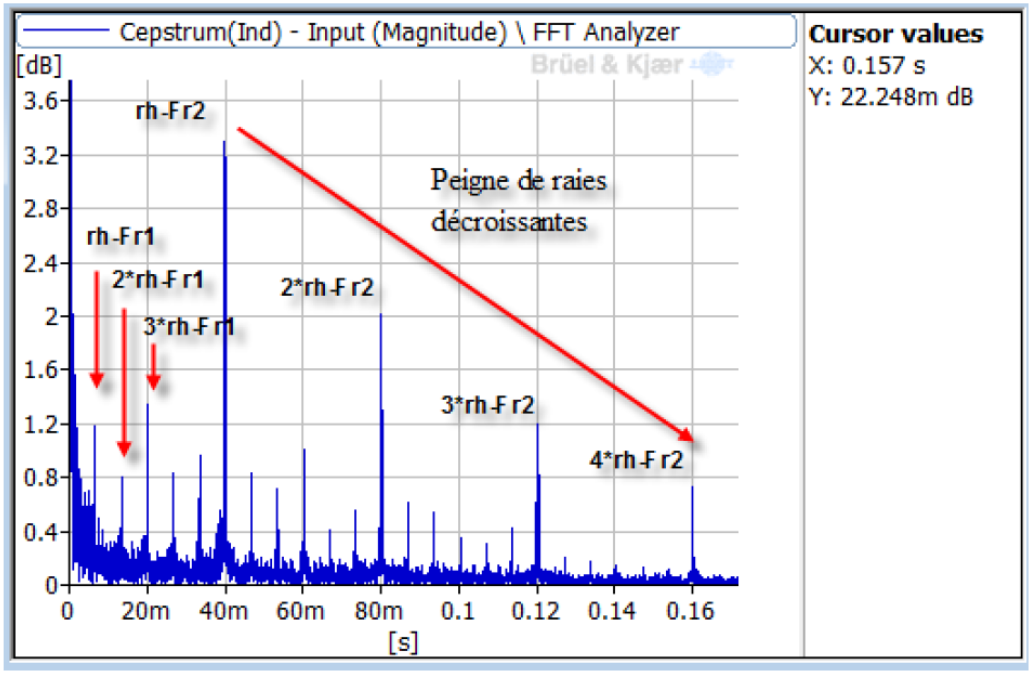


Figure II.4. Example of a Cepstrum.

II.3.5. Time-frequency analysis (Wavelet transform)

Many machine signals are non-stationary, so purely frequency-based methods can miss when certain components occur. Time–frequency methods, such as Short-Time Fourier Transform (STFT), Wigner–Ville distributions, and especially wavelet transforms, jointly describe how frequency content evolves over time [24].

The Continuous Wavelet Transform (CWT) provides multi-resolution analysis, offering good time resolution at high frequencies and good frequency resolution at low frequencies, making it effective for transient events like start-up, coast-down, or rubbing faults. Wavelet-based time–frequency maps have been shown to outperform STFT in resolving fast-changing or transient vibration responses in rotating and structural systems [24] .

Time–frequency and time–scale methods are now considered essential for extracting complex information from vibration signals, especially when combined with modern diagnostic and prognostic algorithms [20].

II.4. Vibration Indicators for Fault Detection

This section outlines widely used scalar indicators (RMS, kurtosis, crest factor, envelope spectrum) and how they relate to vibration signatures of key faults. These concepts are central for building reliable condition indicators and for interpreting spectra in practice.

II.4.1 RMS (Root Mean Square)

RMS represents the overall vibration energy of a signal. It is widely used for severity trending and long-term monitoring of machine health. However, it is generally less sensitive to early impulsive faults, since isolated transient events contribute little to the global energy level [26].

II.4.2 Kurtosis

Kurtosis measures the "peakedness" or impulsiveness of a signal. It is highly sensitive to shocks caused by early bearing or gear damage, and is therefore particularly valuable in the initial stages of fault development. In practice, kurtosis is often computed after band-pass filtering, Variational Mode Decomposition, or envelope filtering to isolate the frequency band of interest [27].

II.4.3 Crest Factor

The crest factor is defined as the ratio of the peak value of a signal to its RMS level. It increases when occasional high-amplitude peaks appear over a moderate background vibration level, making it a useful indicator for detecting early localized defects before they become severe enough to significantly raise the overall RMS [26].

II.4.4 Envelope Spectrum

The envelope spectrum is based on the demodulation of high-frequency structural resonance bands. It reveals characteristic fault frequencies and their sidebands associated with bearing and gear defects, even under noisy operating conditions. It is considered one of the most effective tools for localizing and identifying specific fault types in rotating machinery [28].

Figure II.5. shows the envelope spectrum of same signal. The rotation frequencies Fr1 and Fr2 and several of their harmonics clearly appear in the spectrum, which confirms the presence of a fault on the gear wheel and the pinion."

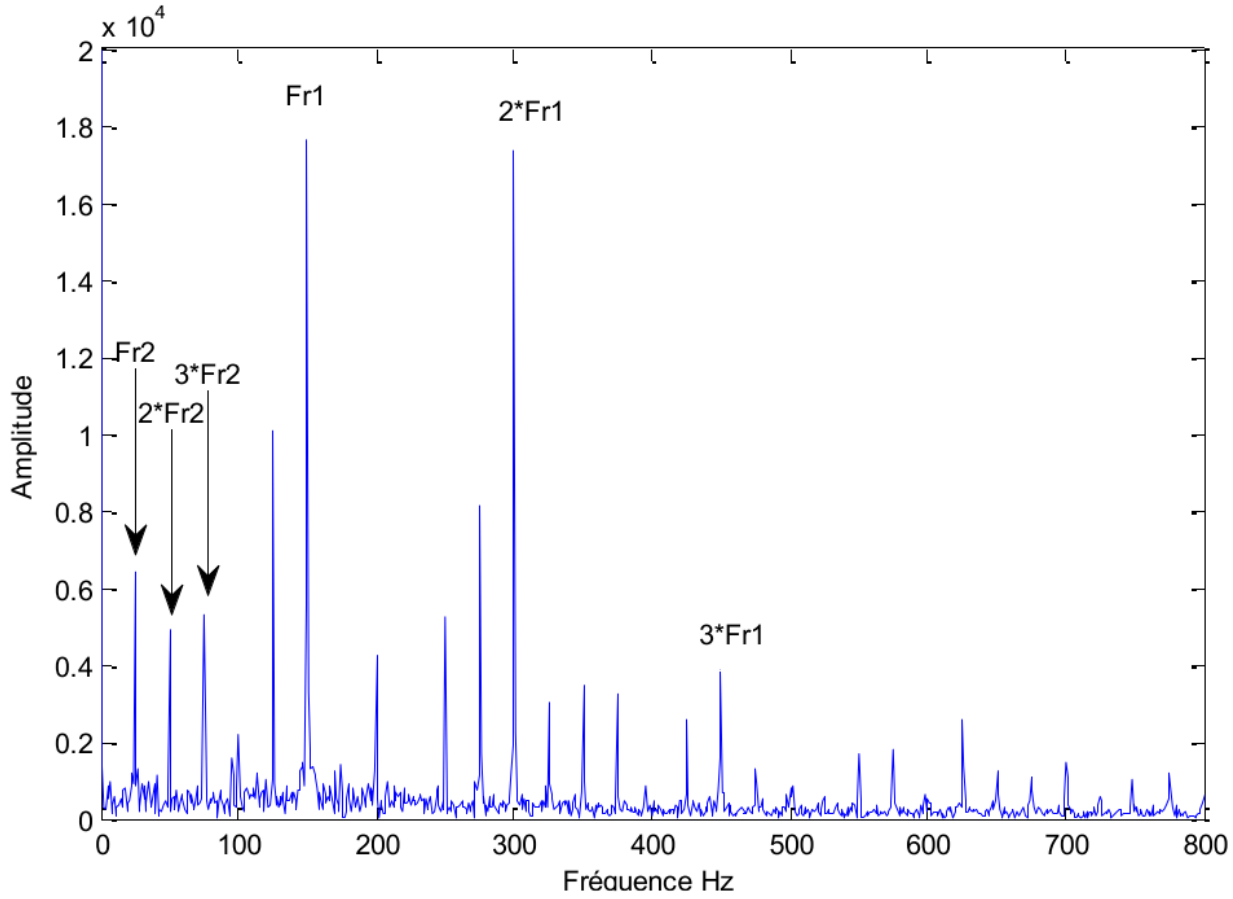


Figure II.5. Example of an Envelope Spectrum.

II.5Vibration Signatures of Main Faults

II.5.1. Imbalance signature

The vibration spectrum is characterized by a dominant component at the running speed 1×rpm, which typically governs the overall response. The vibration amplitude at this frequency increases proportionally with the square of the rotational speed. In the time domain, the signal is generally sinusoidal, especially in the absence of other faults [29].

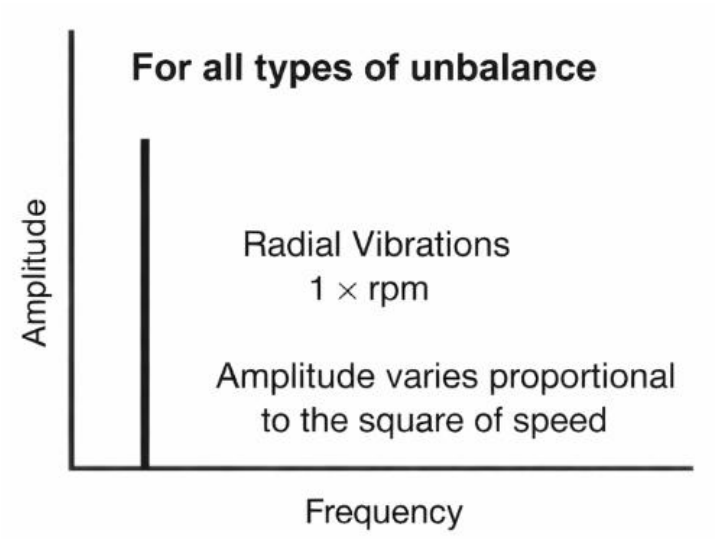


Figure II.6. FFT analysis – imbalance defect

II.5.2. Misalignment signature

The vibration spectrum typically exhibits elevated amplitudes at 1X and 2X, and sometimes 3X components Figure II.7 Axial vibration is often dominant, particularly in angular misalignment cases Figure II.8 [29].

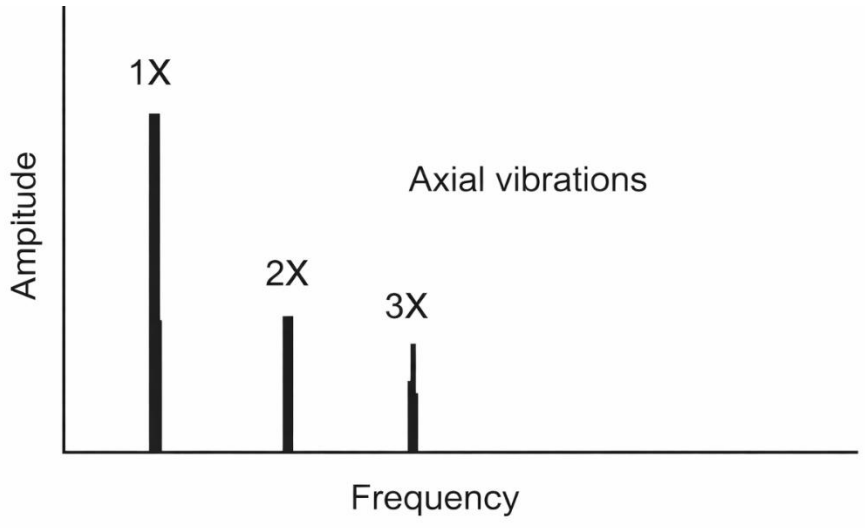


Figure II.7. FFT of angular misalignment

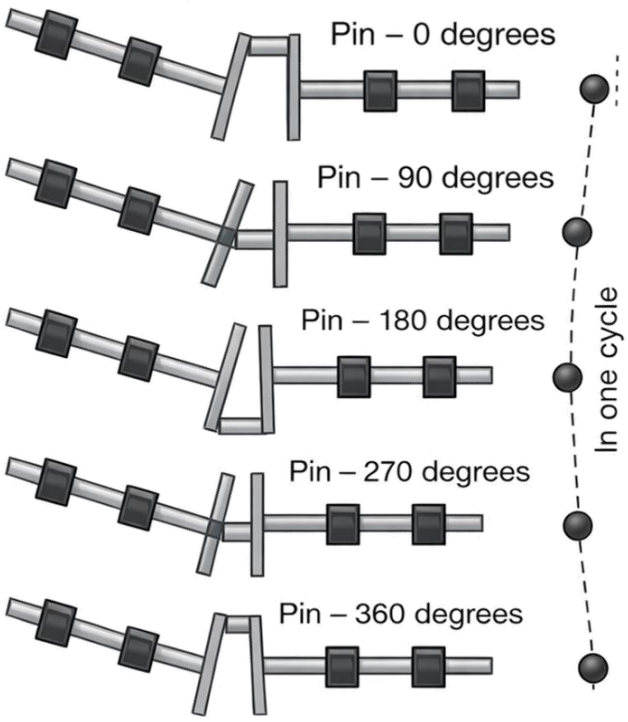


Figure II.8. Angular misalignment

Parallel misalignment tends to generate a strong 2X component due to twice-per-revolution excitation. In severe cases, higher harmonics may appear, along with an increase in overall vibration levels (RMS) [29].

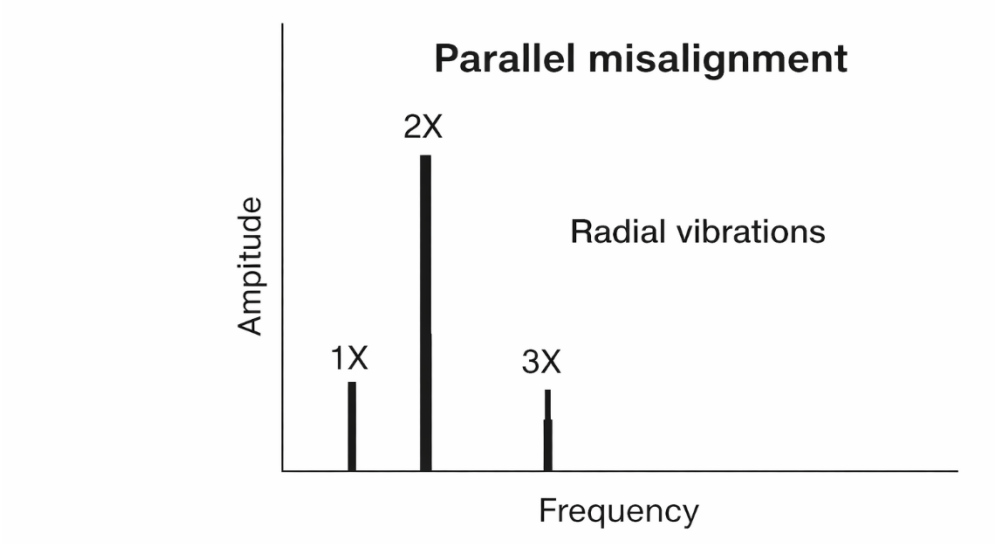


Figure II.9. FFT of parallel misalignment

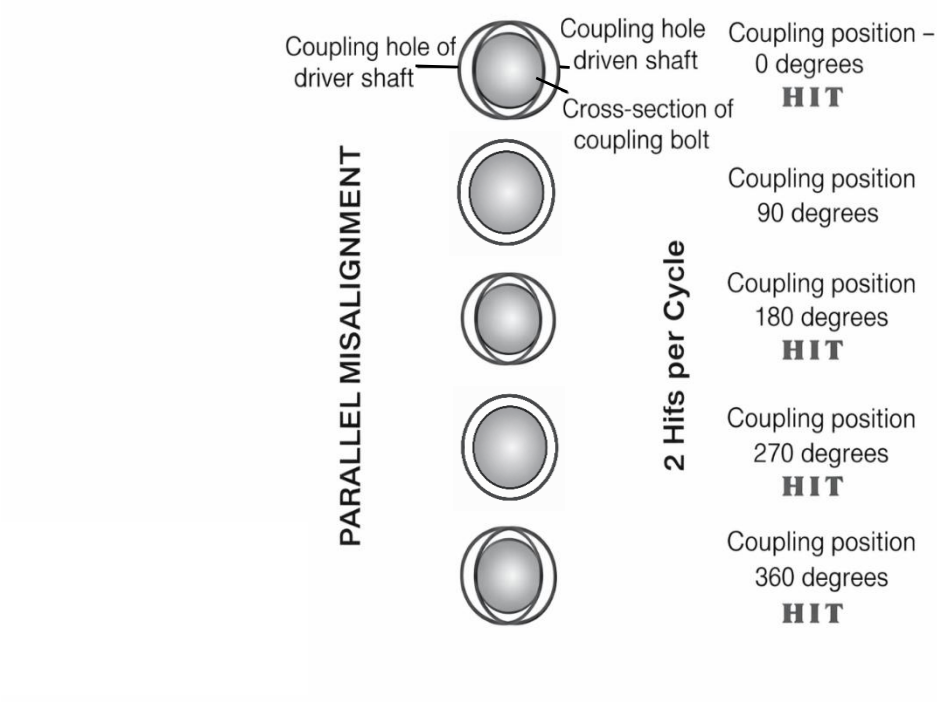


Figure II.10. Parallel misalignment

II.5.3. Bearing fault signature

Defects can occur in any of the parts of the bearing and will cause high-frequency vibrations. In fact, the severity of the wear keeps changing the vibration pattern. In most cases, it is possible to identify the component of the bearing that is defective due to the specific vibration frequencies that are excited. Raceways and rolling element defects are easily detected. However, the same cannot be said for the defects that crop up in bearing cages. Though there are many techniques available to detect where defects are occurring, there are no established techniques to predict when the bearing defect will turn into a functional failure [29].

Bearing defect frequencies are not integrally harmonic to running speed. However, the following formulas are used to determine bearing defect frequencies [29].

Equation II0.1. Ball pass frequency – Inner:

$$BPFI = \left(\frac{N_b}{2}\right) \times \left(1 + \left(\frac{B_d}{P_d}\right)\cos(\theta)\right) \times \mathrm{f_r} \qquad \text{(II.2)}$$

Equation II.3. Ball pass frequency – Outer:

$$BPFO = \left(\frac{N_b}{2}\right) \times \left(1 - \left(\frac{B_d}{P_d}\right)\cos(\theta)\right) \times \mathrm{f_r} \qquad \text{(II.2)}$$

Equation II.4. Fundamental train frequency (Cage):

$$FTF = \left(\frac{1}{2}\right) \times \left(1 - \left(\frac{B_d}{P_d}\right)\cos(\theta)\right) \times f_r \quad \text{(II.3)}$$

Equation II.5. Ball spin frequency (rolling element):

$$BSF = \left(\frac{P_d}{2B_d}\right) \times \left(1 - \left(\frac{B_d}{P_d} \times \cos(\theta)\right)^2\right) \times f_r \quad \text{(II.4)}$$

$\mathbf{f_r}$ = Rotational Frequency (Hz)

$\boldsymbol{N_b}$ = Number of balls or rollers

$\boldsymbol{B_d}$ = Ball/Roller diameter (mm)

$\boldsymbol{P_d}$ = Bearing pitch diameter (mm)

$\boldsymbol{\theta}$ = Contact angle (degrees)

It is very interesting to note that in an FFT, we find both the inner and outer race defect frequencies. Add these frequencies and then divide the result by the machine f_r – [(BPFI + BPFO)/ f_r]. The answer should yield the number of rolling elements.

Bearing deterioration progresses through four stages. During the initial stage, it is just a high-frequency vibration, after which bearing resonance frequencies are observed. During the third stage, discrete frequencies can be seen, and in the final stage high-frequency random noise is observed, which keeps broadening and rising in average amplitude with increased fault severity [29].

- **Stage 1 of bearing defect**

Machinery fault diagnosis using vibration analysis, The FFT spectrum for bearing defects can be split into four zones (A, B, C and D), where we will note the changes as bearing wear progresses. These zones are described as:

Zone A: machine rpm and harmonics zone

Zone B: bearing defect frequencies zone (5–30 kilo cycles per minute (kcpm))

Zone C: bearing component natural frequencies zone (30–120 kcpm)

Zone D: high-frequency-detection (HFD) zone (beyond 120 kcpm).

The first indications of bearing wear show up in the ultrasonic frequency ranges from approximately 20–60 kHz (120–360 kcpm). These are frequencies that are evaluated by high-frequency detection techniques. As Figure II.11 shows, the raceways or rolling elements of the bearing do not have any visible defects during the first stage. The raceways may no longer have the shine of a new bearing and may appear dull gray [29].

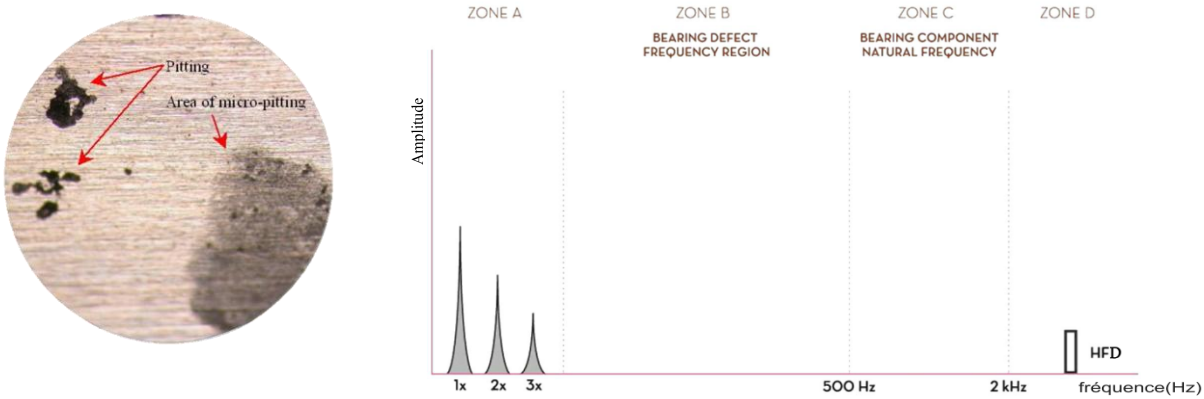


Figure II.11. FFT of Small defects in the raceways of bearing [29]

➢ **Stage 2 of bearing defect**

In the following stage Figure II.12. the fatigued raceways begin to develop minute pits. Rolling elements passing over these pits start to generate the ringing or the bearing component natural frequencies that predominantly occur in the 30–120 kcpm range. Depending on the severity, it is possible that the sideband frequencies (bearing defect frequency ± rpm) appear above and below the natural frequency peak at the end of stage two. The high-frequency detection (HFD) techniques may double in amplitude compared to the readings during stage one [14].

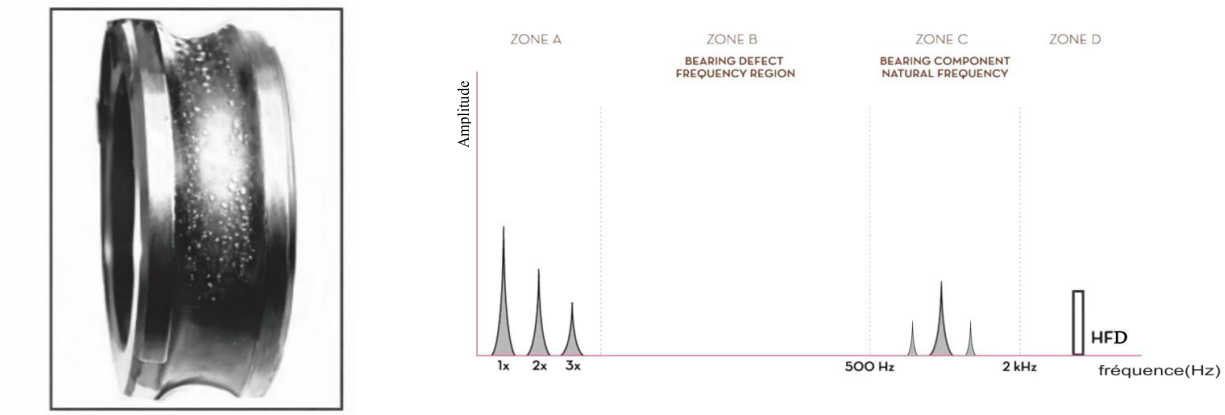


Figure II.12. FFT of an obvious wear in the form of pits

➢ **Stage 3 of bearing defect**

As we enter the third stage (Figure II.13), the discrete bearing frequencies and harmonics are visible in the FFT. These may appear with a number of sidebands. Wear is usually now visible on the bearing and may expand through to the edge of the bearing raceway.

The minute pits of the earlier stage are now developing into bigger pits and their numbers also increase. When well-formed sidebands accompany any bearing defect frequency or its harmonics, the HFD components have again almost doubled compared to stage three. It is usually advised to replace the bearing at this stage. Some studies indicate that after the third stage, the remaining bearing life can be 1 h to 1% of its average life [14].

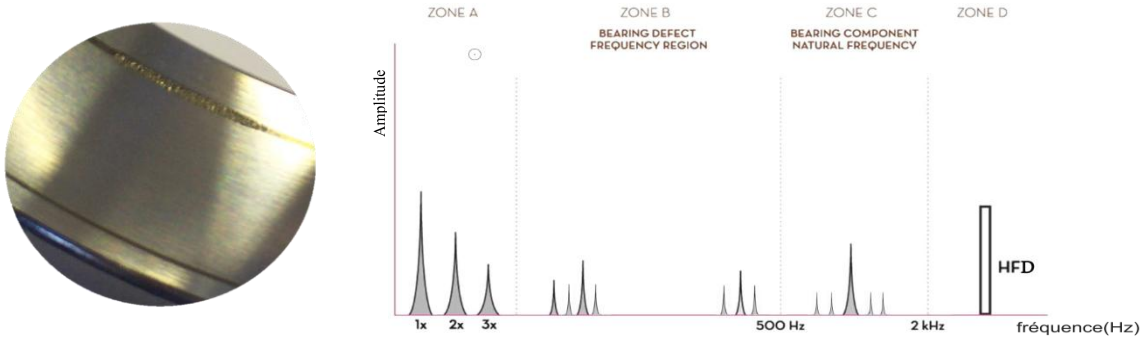


Figure II.13. FFT of a clearly visible wear over the breadth of the bearing.

➢ **Stage 4 of bearing defect**

In the final phase (Figure II.14), the pits merge with each other, creating rough tracks and spalling of the bearing raceways or/and rolling elements. The bearing is in a severely damaged condition now. Even the amplitude of the 1× rpm component will rise. As it grows, it may also cause growth of many running speed harmonics. It can be visualized as higher clearances in the bearings allowing a higher displacement of the rotor.

Discrete bearing defect frequencies and bearing component natural frequencies actually begin to merge into a random, broadband high-frequency ‘noise floor’. Initially, the average amplitude of the broad noise may be large. However, it will drop and the width of the noise will increase. In the final stage, the amplitude will rise again and the span of the noise floor also increases [14].

However, amplitudes of the high-frequency noise floor and some of the HFD may in fact decrease (due to pits flattening to become spalls), but just prior to failure spike energy will usually grow to extreme amplitudes

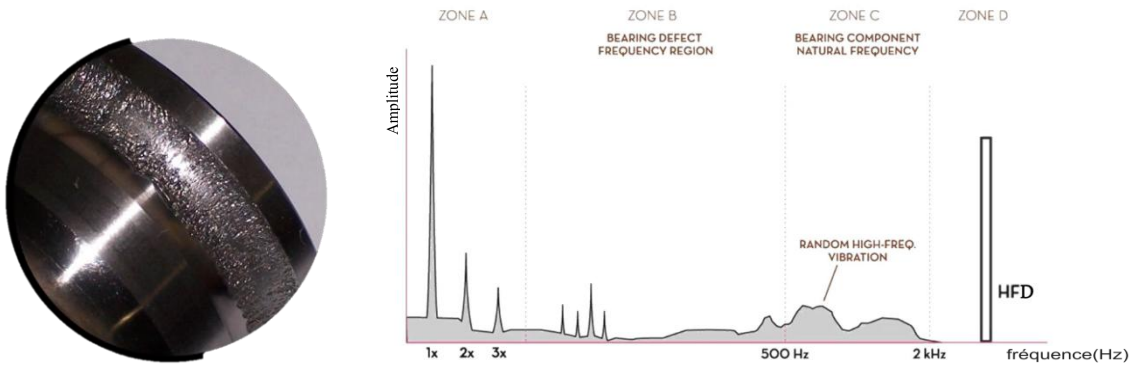


Figure II.14. Severely damaged bearing in final stage of wear

By this time, the bearing will be vibrating excessively; it will be hot and making lots of noise, if it is allowed to run further, the cage will break and the rolling elements will go loose. The elements may then run into each other, twisting, turning and welded to one another, until the machine will hopefully trip on overload. In all probability, there will be serious damage to the shaft area under the bearing [14].

II.5.4. Gear fault signature

A gearbox is a piece of rotating equipment that can cause the normal low-frequency harmonics in the vibration spectrum, but also show a lot of activity in the high frequency region due to gear teeth and bearing impacts. The spectrum of any gearbox shows the 1× and 2× rpm, along with the gear mesh frequency (GMF). The GMF is calculated by the product of the number of teeth of a pinion or a gear, and its respective running speed [14]:

Equation II.6. Gear mesh frequency:

$$GMF = \text{pinion rpm} \times \text{number of teeth on pinion} \quad \text{(II.5)}$$

The GMF will have running speed sidebands relative to the shaft speed to which the gear is attached. Gearbox spectrums contain a range of frequencies due to the different GMFs and their harmonics. All peaks have low amplitudes and no natural gear frequencies are excited if the gearbox is still in a good condition. Sidebands around the GMF and its harmonics are quite common. These contain information about gearbox faults Figure II.15.

Tooth wear and backlash can excite gear natural frequencies along with the gear mesh frequencies and their sidebands. Signal enhancement analysis enables the collection of vibrations from a single shaft inside a gearbox [14].

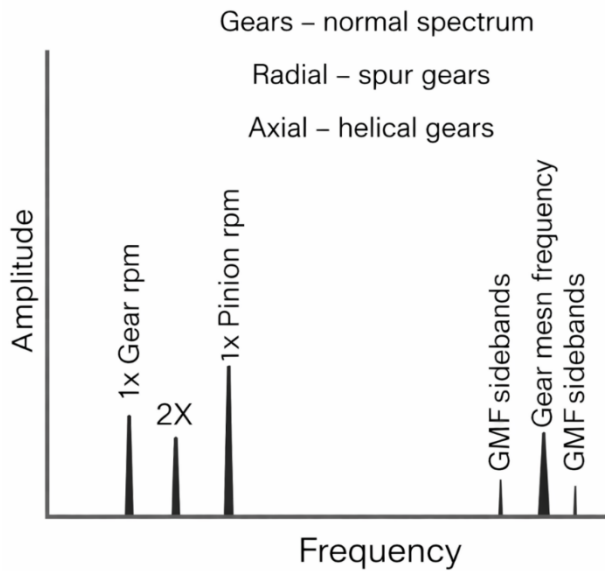


Figure II.15. Normal Vibration Spectrum of Gears

Distributed gear faults such as tooth wear and surface pitting will produce sidebands and harmonics that have high amplitude close to the tooth-mesh frequency. Localized faults such as a cracked tooth produce sidebands that are spread more widely across the spectrum [14].

- **Gear tooth wear**

An important characteristic of gear tooth wear is that gear natural frequencies are excited with sidebands around them. These are spaced with the running speed of the bad gear [14]. The GMF may or may not change in amplitude, although high-amplitude sidebands surrounding the GMF usually occur when wear is present. Sidebands are a better wear indicator than the GMF itself (Figure II.16).

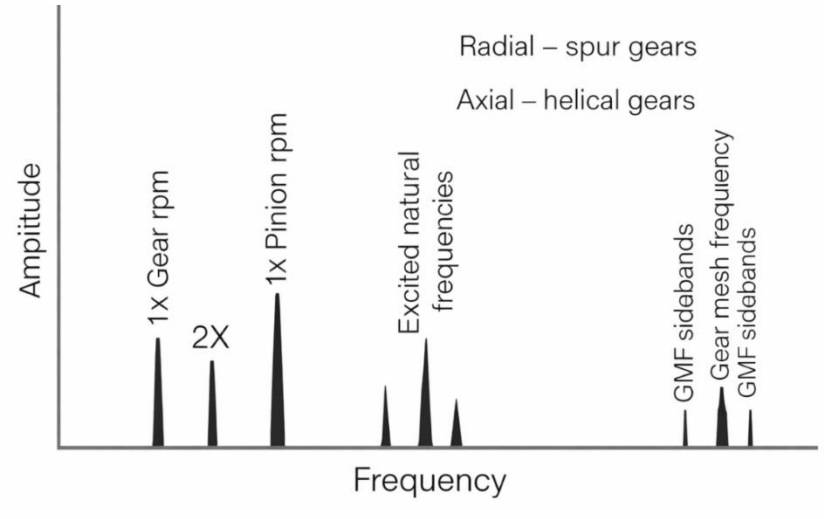


Figure II.16. Vibration spectrum of Gear Tooth Wear

- **Gear tooth load**

As the load on a gearbox increases, the GMF amplitude may also increase. High GMF amplitudes do not necessarily indicate a problem, particularly if sideband frequencies remain low and no gear natural frequencies are excited [14]. It is advised that vibration analysis on a gearbox be conducted when the gearbox is transmitting maximum power (Figure II.17).

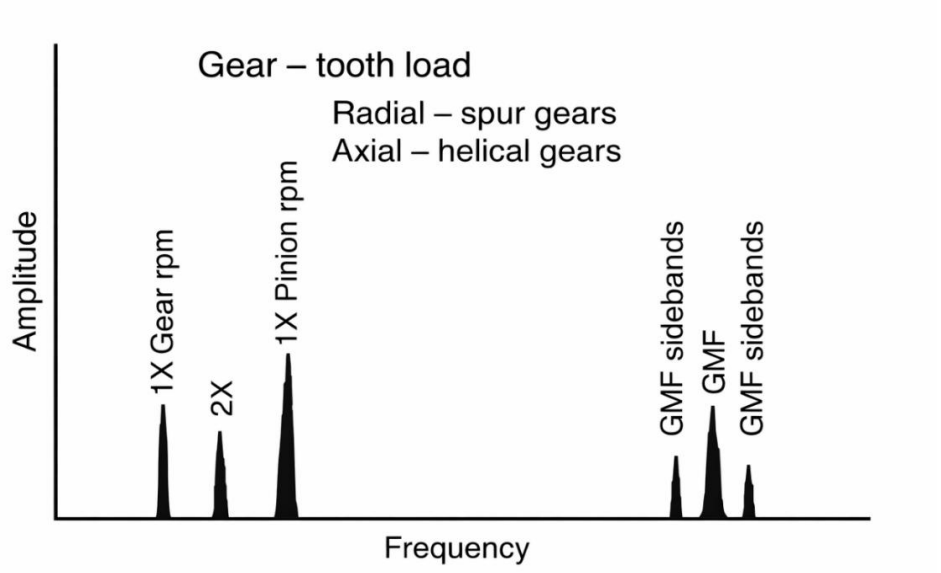


Figure II.17. Vibration spectrum of Gear Tooth load

- **Gear eccentricity and backlash**

Fairly high amplitude sidebands around the GMF often suggest gear eccentricity, backlash or non-parallel shafts. In these cases, the rotation of one gear may cause the amplitude of gear vibration to modulate at the running speed of the other. This can be seen in the time domain waveform. The spacing of the sideband frequencies indicates the gear with the problem. Improper backlash normally excites the GMF and gear natural frequencies. Both will have sidebands at 1× rpm. The GMF amplitudes will often decrease with increasing load if backlash is the problem (Figure II.18) [14].

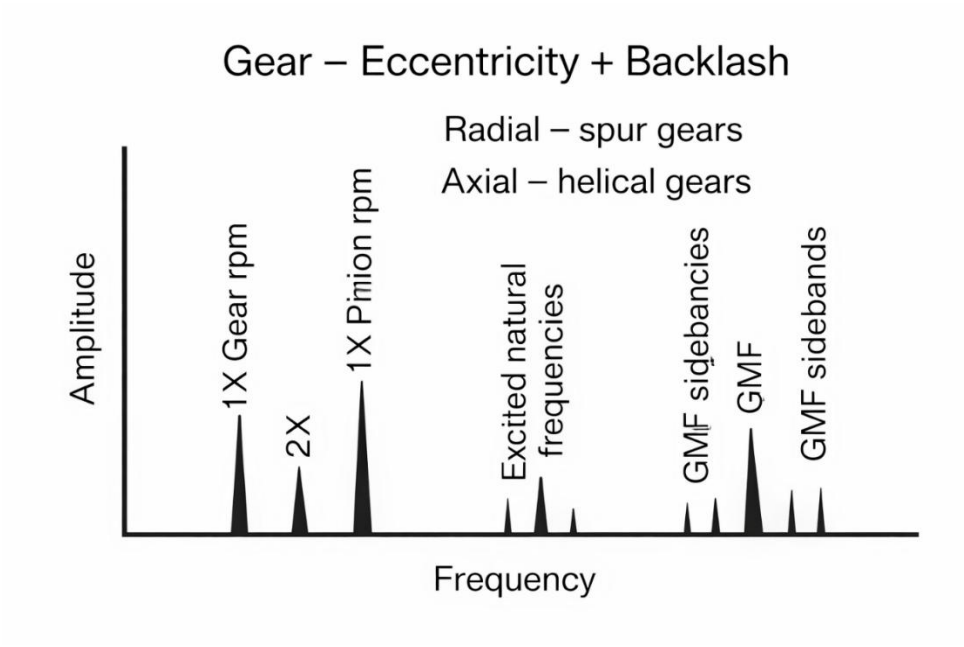


Figure II.18. Vibration spectrum of Gear eccentricity + backlash.

- **Gear misalignment**

Gear misalignment almost always excites second order or higher GMF harmonics, which will have sidebands spaced with the running speed. It will often show only small amplitudes at 1× GMF, but much higher levels at 2× or 3× GMF. It is important to set the F-max of the FFT spectrum to more than 3× GMF (Figure II.19) [14].

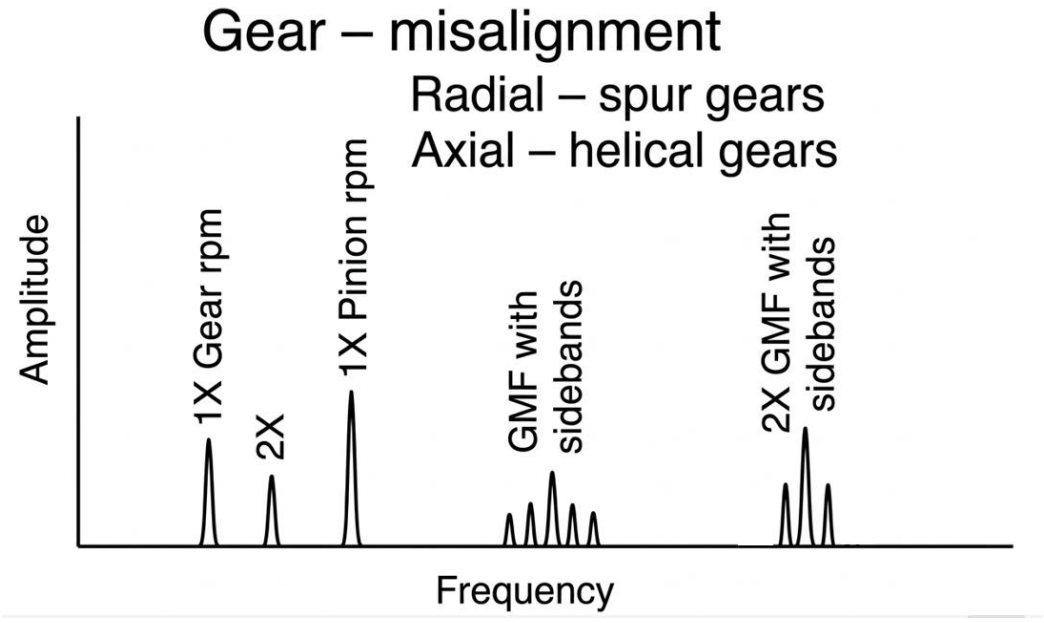


Figure II.19. Vibration spectrum of Gear misalignment

➢ **Gears – cracked or broken tooth**

A cracked or broken gear tooth will generate high amplitude at 1× rpm of this gear, plus it will excite the gear natural frequency with sidebands spaced with its running speed. It is best detected in the time domain, which will show a pronounced spike every time the problematic tooth tries to mesh with teeth on the mating gear. The time between impacts will correspond to 1/speed of the gear with the broken tooth. The amplitude impact spike in the time waveform will often be much higher than that of the 1× gear rpm in the FFT spectrum (Figure II.20) [29].

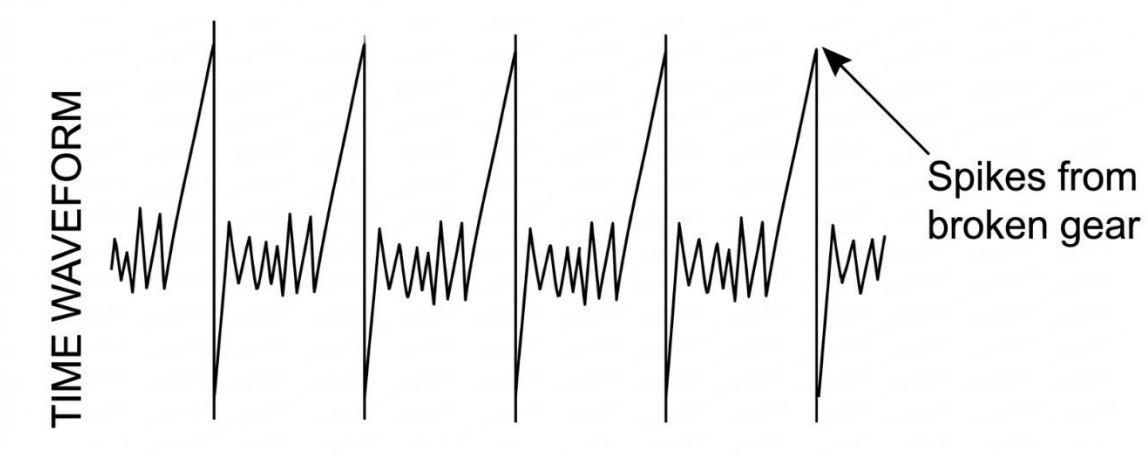


Figure II.20. Time waveform of a Gears – cracked or broken tooth

➢ **Gears – hunting tooth problems**

The gear hunting tooth frequency is particularly effective for detecting faults on both the gear and the pinion that might have occurred during the manufacturing process or due to mishandling. It can cause quite high vibrations, but since it occurs at low frequencies, predominantly less than 600 cpm, it is often missed during vibration analysis. The hunting tooth frequency is calculated with:

Equation 0.7. Hunting Tooth Frequency *(Fht)* :

$$\text{Fht} = \frac{GMF \times N}{(no.of\ pinion\ teeth) \times (no.of\ gear\ teeth)} \quad \text{(II.6)}$$

In the above equation, N is known as the assembly phase factor, also referred to as the lowest common integer multiple between the number of teeth on the pinion and gear. This hunting tooth frequency is usually very low [29].

For assembly phase factors (N > 1), every gear tooth will not mesh with every pinion tooth. If N = 3, teeth numbers 1, 4, 7, etc. will mesh with one another (however, gear tooth 1 will not mesh

with pinion teeth 2 or 3; instead, it will mesh with 1, 4, 7, etc.). For example, a gear with 98 teeth is running at 5528 rpm and is meshing with a pinion with 65 teeth and running 8334 rpm. The assembly phase factor is N = 1. The hunting tooth frequency (Fht) can be calculated as follows:

$$Fht = \frac{(98 \times 5528) \times 1}{98 \times 65} = 85\ cpm\ (1.42\ Hz)$$

Another formula is the rpm of the gear divided by the number of pinion teeth (5528/65 = 85 cpm). This is a special case and applies to a hunting tooth combination only when N = 1.

If the tooth repeat frequency is a problem (Figure II.21), one can usually audibly hear it since it is a beat frequency. A gearset with a tooth repeat problem normally emits a 'growling' sound from the driven end. Its repetition rate can often be established by simply counting the sounds using a stopwatch. The maximum effect occurs when the faulty pinion and gear teeth mesh at the same time (on some drives, this may occur once every 10 or 20 revolutions, depending on the Fht formula) [29].

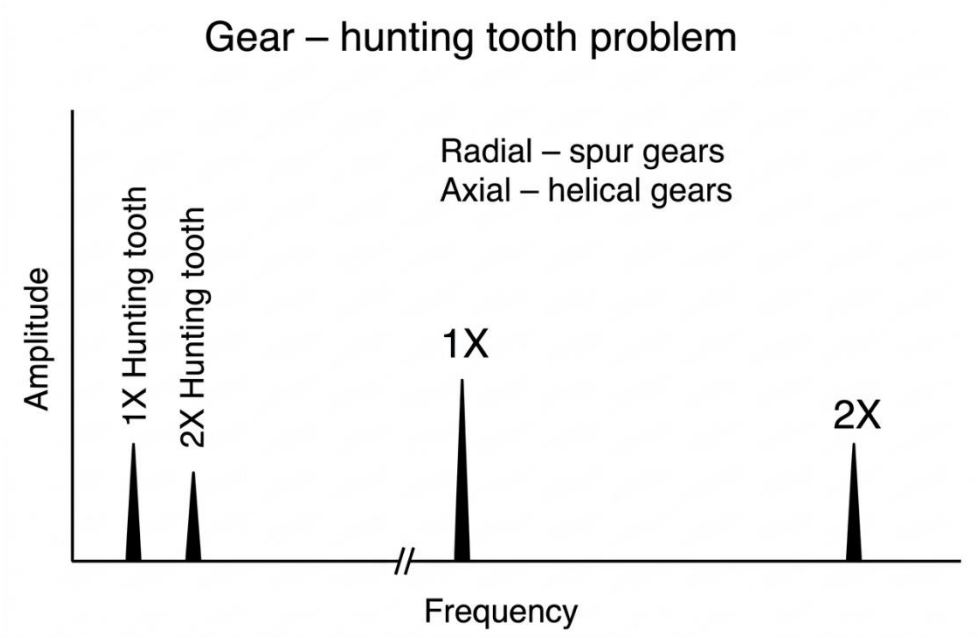


Figure II.21. Vibration spectrum of Gear hunting Problem.

II.6. Conclusion

This chapter presents the theoretical framework of vibration analysis as a fundamental tool for diagnosing faults in rotating machinery. The dynamic concepts governing the behavior of mechanical systems were first introduced, followed by their connection to signal analysis techniques in both the time and frequency domains, in addition to advanced methods such as cepstrum analysis and time–frequency analysis.

It was also demonstrated that vibration signals carry direct information about the nature of mechanical defects, as each fault manifests through a distinctive pattern in the spectrum or in the time waveform. Imbalance is typically associated with a component at running speed, misalignment appears through harmonics, while bearing and gear faults are characterized by specific frequencies and sidebands that can be accurately identified using spectral and envelope analysis techniques.

Furthermore, the study showed that accurate diagnosis does not rely on a single indicator, but rather on the integration of multiple analytical tools, including the Fast Fourier Transform (FFT), statistical indicators such as RMS and kurtosis, and time–frequency techniques for non-stationary signals. This integrated approach enables a deeper understanding of fault progression and its different stages.

Based on the above, this chapter establishes the necessary scientific foundation for vibration-based fault diagnosis and provides the theoretical basis for the practical implementation and experimental analysis presented in the subsequent chapters.

Chapter III

Mathematical Modeling and Signal Analysis for Machinery Fault Diagnosis

III.1. Introduction

Vibration signal analysis constitutes one of the most powerful and widely adopted approaches for the condition monitoring and fault diagnosis of rotating machinery. As established in the literature, vibration signals emitted by a machine carry rich information about the internal forces and mechanical state of its components. The accurate extraction of this information requires both a sound mathematical model of the dynamic system under investigation and robust signal processing tools capable of handling the inherent complexity of real-world vibration data.

This chapter develops the theoretical foundations underpinning the signal analysis methodology adopted in this work. It first presents the mathematical model of the machinery vibration system, followed by a review of classical Fourier-based signal analysis methods and their limitations. The chapter then introduces the Hilbert Transform and the analytic signal framework, including their application to envelope detection. Finally, the Hilbert–Huang Transform (HHT) and Empirical Mode Decomposition (EMD) are presented as the primary adaptive analysis tools employed in this study.

III.2. Signal Representation and Mathematical Framework

Before introducing the mathematical model of rotating machinery and the associated signal processing techniques, it is useful to define the mathematical space in which vibration signals are represented. In vibration analysis, the measured signals are generally assumed to be finite-energy signals, ensuring that they can be processed using classical and advanced spectral analysis methods. Such signals belong to the Hilbert space of square-integrable functions, denoted by $L^2(\mathbb{R})$.

A signal x(t) belongs to the space $L^2(\mathbb{R})$ if and only if:

Equation III.1. Finite Energy Condition:

$$\int_{-\infty}^{+\infty} |x(t)|^2 \, dt < +\infty \qquad \textbf{(III.1)}$$

III.3. Mathematical Modeling of Machinery Systems

Rotating machinery, including motors, gearboxes, pumps, and turbines, can be described in terms of mechanical vibration by modelling the structure as a dynamic system composed of mass, stiffness, and damping elements. Such models provide the theoretical basis for understanding the relationship between mechanical faults and the resulting vibration signatures measured at accessible points on the machine housing. It is well established that any real machine can be decomposed into one or more mass-spring-damper subsystems, each characterized by its natural frequency and damping ratio.

For a lumped-parameter single-degree-of-freedom (SDOF) mechanical system, the equation of motion governing the vibration response is expressed as [38, 42]:

Equation III.2. Equation of Motion (EOM):

$$M\ddot{x}(t) + C\dot{x}(t) + Kx(t) = F(t) \qquad \textbf{(III.2)}$$

where *M* is the mass matrix, *C* is the viscous damping coefficient, *K* is the stiffness, *x(t)* is the displacement response, and *F(t)* is the externally applied excitation force. For multi-degree-of-freedom (MDOF) systems, these scalar quantities become matrices and vectors of corresponding dimensions. The natural frequency of the undamped system is given by:

Equation III.3. Natural Frequency:

$$\omega_n = \sqrt{\frac{K}{M}} \quad (\textbf{\textit{III.3}}) \tag{III.3}$$

This natural frequency ω_n plays a critical role in the envelope detection methodology described in Section III.5, where the resonance band of the bearing housing is used as the demodulation carrier frequency. In practice, machinery faults such as bearing defects, gear tooth damage, or mass imbalance alter the effective stiffness, damping, or excitation forces within the system, thereby modifying the vibration response in characteristic and identifiable ways. The mathematical model thus provides the physical rationale for associating specific spectral features with particular fault types.

For rotating machinery, the primary excitation forces arise from the rotation of unbalanced masses, from gear meshing dynamics, and from the periodic impacts generated by defective rolling elements. Under steady-state operating conditions, the excitation force *F(t)* can be decomposed into harmonic components at integer multiples of the shaft rotational frequency, yielding a vibration spectrum whose dominant peaks correspond to known mechanical events. When a fault develops, additional frequency components (the characteristic defect frequencies) emerge in the spectrum and serve as diagnostic indicators [38, 42].

III.4. Classical Signal Analysis: Fourier-Based Methods

The vibration signal *x(t)* measured at the bearing housing constitutes a superposition of contributions from all active vibration sources within the machine. Extracting meaningful diagnostic information from this signal requires appropriate signal processing methods. The following subsections review the classical Fourier-based techniques, which form the foundation upon which more advanced methods are subsequently built.

III.4.1 Fourier Transform

The Fourier Transform (FT) provides a decomposition of a time-domain signal into its constituent frequency components and remains the most widely used tool in machinery vibration analysis. For a continuous signal *x(t)*, the Fourier Transform *X(f)* is defined as [38, 42]:

The Fourier Transform can be interpreted as the projection of the signal x(t) onto an orthogonal basis of complex exponentials $\{e^{-j2\pi ft}\}$. Each coefficient X(f) measures the 'similarity'

(in the inner product sense) between the signal and the corresponding basis function at frequency f, yielding a complete orthogonal decomposition of the signal energy across the frequency axis [38].

Equation III.4. Fourier Transform (FT):

$$X(f) = \int_{-\infty}^{+\infty} x(t) \cdot e^{-j2\pi ft}\, dt \qquad (\boldsymbol{III}.4)$$

where *f* is the frequency in hertz. The resulting spectrum *X(f)* expresses the energy distribution of the signal across the frequency domain. For the purpose of machinery diagnostics, spectral peaks at specific frequencies corresponding to the shaft rotational speed and its harmonics (as well as to the bearing characteristic defect frequencies (BPFI, BPFO, BSF, FTF)) serve as the primary indicators of mechanical condition. [42]

The Fourier Transform is invertible. Given the spectrum X(f), the original signal x(t) is recovered through the Inverse Fourier Transform (IFT) [38, 42]:

Equation III.5. Inverse Fourier Transform (IFT):

$$x(t) = \int_{-\infty}^{+\infty} X(f) \cdot e^{j2\pi ft}\, df \qquad (\boldsymbol{III}.5)$$

The FT and IFT pair establish a complete duality between the time domain and the frequency domain: any signal can be represented equivalently in either domain without loss of information [38].

The Fourier Transform satisfies several fundamental properties of direct relevance in signal processing [38, 42]:

(i) Linearity: The transform of a linear combination of signals equals the same linear combination of their individual transforms:

Equation III.6. Linearity:

$$\mathcal{F}\{\alpha\, x(t) + \beta\, y(t)\} = \alpha\, X(f) + \beta\, Y(f) \qquad (\text{III}.6)$$

(**II) Time Shift**: A time delay t_0 in the time domain corresponds to a phase shift in the frequency domain:

Equation III. 7. Time Shift:

$$\mathcal{F}\{x(t - t_0)\} = X(f) \cdot e^{-j2\pi f\, t_0} \qquad (\text{III}.7)$$

(III) Conservation of Energy (Parseval's theorem): The total energy of a signal is identical whether computed in the time domain or in the frequency domain:

Equation III.8. Parseval's Theorem (Energy Conservation):

$$\int_{-\infty}^{+\infty}|x(t)|^2\,dt = \int_{-\infty}^{+\infty}|X(f)|^2\,df \quad \text{(III.8)}$$

The fundamental limitation of the Fourier Transform, however, is its assumption of global stationarity: it assigns a single, time-invariant amplitude to each frequency component over the entire analysis window. Consequently, any time-localized event (such as an impulsive bearing fault impact that occurs and decays within a fraction of a revolution) is smeared across the entire frequency axis, reducing its detectability and yielding spurious harmonics. As demonstrated by Huang and Wu [33], this intrinsic limitation of Fourier-based representations is particularly severe when the signal is non-stationary and nonlinear, as is invariably the case for machinery vibration under realistic operating conditions.

III.4.2 Discrete Fourier Transform and FFT

In practice, vibration signals are acquired digitally at a sampling frequency *fs*, yielding a discrete time series. The Discrete Fourier Transform (DFT) adapts the continuous Fourier integral to this discrete context. For a sequence of *N* samples *x[n]*, the DFT is defined as [38]:

Equation III.9. Discrete Fourier Transform (DFT):

$$X[k] = \sum_{n=0}^{N-1} x[n] \cdot e^{-j2\pi\frac{kn}{N}},\ k = 0,1,\ldots,N-1 \quad \text{(III.9)}$$

where k indexes the discrete frequency bins. The Fast Fourier Transform (FFT) is an algorithmically efficient implementation of the DFT, reducing its computational complexity from $O(N^2)$ to O (N log N). It is the standard spectral analysis tool in digital vibration analysers and condition monitoring systems. The goal of spectral analysis in the context of rotating machinery is to identify the dominant frequency components and relate them to specific mechanical phenomena, thereby enabling the localization and characterization of faults.

An important practical consideration is the selection of the sampling frequency and the analysis window length. According to the Nyquist criterion, the sampling frequency must be at least twice the highest frequency of interest. The frequency resolution $\Delta f = fs / N$ is inversely proportional to the record length, which determines the ability to resolve closely spaced spectral lines corresponding to different fault frequencies.

The limitation of the standard FFT in analysing non-stationary signals motivates the use of time–frequency representations, which jointly characterise the spectral content of a signal as a

function of time. The Short-Time Fourier Transform (STFT) addresses this by computing the Fourier transform of successive short, windowed segments of the signal, yielding a two-dimensional time–frequency map. Whilst the STFT provides a practical compromise between time and frequency resolution, it is constrained by Heisenberg's uncertainty principle, which prevents the simultaneous attainment of arbitrarily fine resolution in both domains [38]. A fixed window length therefore implies a fixed time–frequency resolution trade-off, regardless of the local characteristics of the signal. For machinery fault signals, which may contain both low-frequency modulations and high-frequency transient impacts, this limitation can be significant.

III.4.3 Time–Frequency Analysis

The Fourier Transform, as established in Section III.4.1, assigns a single time-invariant amplitude to each frequency component and is therefore unable to describe signals whose spectral content evolves over time. To overcome this limitation, the Short-Time Fourier Transform (STFT) was introduced as the first practical time–frequency analysis tool [38]. The STFT divides the signal x(t) into successive short, overlapping segments using a sliding analysis window g(t) of fixed width, and computes the Fourier Transform of each segment independently. The result is a two-dimensional time–frequency representation defined as [38]:

Equation III.10. Short-Time Fourier Transform (STFT):

$$STFT\{x\}(t,f) = \int x(\tau) \cdot g(\tau - t) \cdot e\text{^}(-j2\pi f\tau)\, d\tau \qquad (\boldsymbol{III}.10)$$

Where g (τ − t) is the analysis window centered at time t, and τ is the integration variable. The squared modulus |STFT{x} (t, f) |² defines the spectrogram, a time–frequency energy map widely used in machinery vibration analysis to visualize how spectral components evolve during run-up, coast-down, or transient fault events [38].

The fundamental limitation of the STFT, however, is its fixed time–frequency resolution: once the window length is chosen, the time resolution Δt and frequency resolution Δf are fixed throughout the entire analysis, constrained by Heisenberg's uncertainty principle $\Delta t \cdot \Delta f \geq 1/(4\pi)$. A short window yields good time localization but poor frequency resolution; a long window yields good frequency resolution but poor time localization. For rotating machinery fault signals, which may simultaneously contain low-frequency amplitude modulations and high-frequency impulsive transients, this fixed-resolution trade-off constitutes a significant limitation. The Continuous

Wavelet Transform presented in the following section addresses this constraint through multi-resolution analysis.

III.4.4 Wavelet Transform

The Continuous Wavelet Transform (CWT) overcomes the fixed-resolution limitation of the STFT by employing a family of basic functions (the wavelets) that are scaled and translated versions of a prototype mother wavelet $\psi(t)$. The CWT of a signal $x(t)$ is defined as [39]:

Equation III.11. Continuous Wavelet Transform (CWT):

$$W(a,b) = \frac{1}{\sqrt{a}} \int x(t) \cdot \psi * \left(\frac{t-b}{a}\right) dt \quad \text{(III.11)}$$

Where $a > 0$ is the scale parameter (inversely proportional to frequency) and b is the translation parameter (temporal position). The asterisk denotes the complex conjugate. By dilating and compressing the mother wavelet, the CWT achieves a multi-resolution analysis: wide wavelets capture low-frequency trends, whilst narrow wavelets resolve high-frequency transients. This adaptability makes the wavelet transform particularly suitable for detecting the impulsive events generated by bearing defects, which are simultaneously localized in both time and frequency. [39, 40]

Despite these advantages, the wavelet transform retains a fundamental limitation: the basic functions are defined *a priori* and are independent of the signal under analysis. As argued by Huang et al. [32], there is no a priori guarantee that any pre-selected wavelet basis faithfully represents the underlying physical processes in a given signal. Furthermore, the use of an a priori basis inevitably introduces spurious harmonic artefacts when applied to genuinely nonlinear signals. These observations motivate the development of the fully adaptive methods presented in Sections III.5 and III.6.

III.5. Hilbert Transform and Analytic Signal

III.5.1 Definition of the Hilbert Transform

The Hilbert Transform (HT) is a fundamental mathematical operator in signal processing theory that provides a systematic means of constructing the analytic representation of any real-valued time series. For a real-valued signal $x(t)$ belonging to the Lp class, its Hilbert transform $y(t)$ is formally defined through the following Cauchy principal value integral [32, 33]:

Equation III.12. Hilbert Transform Definition:

$$y(t) = \frac{1}{\pi} P.V. \int_{-\infty}^{+\infty} \frac{x(\tau)}{t-\tau} d\tau \quad \text{(III.12)}$$

The Cauchy principal value P.V. of a singular integral is defined as the symmetric limit that removes the singularity at τ = t [32, 33]:

Equation III.13. Cauchy Principal Value:

$$P.V. \int_{-\infty}^{+\infty} \frac{g(\tau)}{t-\tau} d\tau = lim\, \varepsilon \to 0^{+} \left(\int_{-\infty}^{t-\varepsilon} \frac{g(\tau)}{t-\tau} d\tau + \int_{t+\varepsilon}^{+\infty} \frac{g(\tau)}{t-\tau} d\tau \right) \quad \textbf{(\textit{III}.13)}$$

The convolution operator (*) between two functions x(t) and h(t) is defined by:

Equation III.14. Convolution:

$$(x * h)(t) = \int_{-\infty}^{+\infty} x(\tau)\, h(t-\tau)\, d\tau \quad \textbf{(\textit{III}.14)}$$

Note that the Hilbert transform can equivalently be interpreted as the convolution of x(t) with the kernel h(t) = 1/(πt) [38]:

where P.V. denotes the Cauchy principal value of the singular integral, introduced to handle the singularity at $\tau = t$. By pairing the original signal *x(t)* with its Hilbert transform *y(t)* as the imaginary component, a complex-valued analytic signal is constructed as follows:

Equation III.15. Analytic Signal:

$$z(t) = x(t) + i \cdot y(t) = a(t) \cdot e^{i\theta(t)} \quad \text{(III.15)}$$

where the instantaneous amplitude *a(t)* and instantaneous phase *θ(t)* are respectively defined by Equations III.19 and III.20, presented below following the derivation of the inverse Hilbert transform.

The inverse of the Hilbert transform recovers the original signal x(t) from its transform y(t). Since the Hilbert transform is an anti-involution (applying it twice returns the negative of the original), the Inverse Hilbert Transform is given by [38]:

Equation III.16. Inverse Hilbert Transform:

$$x(t) = -\frac{1}{\pi} P.V. \int_{-\infty}^{+\infty} \frac{y(\tau)}{t-\tau} d\tau \quad \text{(III.16)}$$

The Hilbert transform has an important and elegant frequency-domain interpretation. Since H{x(t)} = x(t) * (1/πt), the convolution theorem gives the spectral form of the Hilbert filter [43, 44]:

Equation III.17. Spectral Representation of the Hilbert Transform:

$$Y(j\omega) = X(j\omega) \cdot [-j \cdot sgn(\omega)] \quad (\textbf{\textit{III}}.17)$$

This is an all-pass filter that shifts phase by −90° for positive frequencies and +90° for negative frequencies. The piecewise form is:

Equation III.18. Phase-Shifting Property:

$$Y(j\omega) = \begin{cases} -j\,X(j\omega), \omega > 0 \\ +j\,X(j\omega), \omega < 0 \end{cases} \quad (\text{III}.18)$$

The Hilbert transform result can also be recovered via the inverse Fourier Transform [43]:

Equation III.19. Hilbert via Inverse Fourier:

$$H\{x(t)\} = y(t) = \mathcal{F}^{-1}\{Y(j\omega)\} \quad (\text{III}.19)$$

Since applying H twice returns the negative of the original signal, the inverse satisfies [43]:

Equation III.20. Anti-Involution Property:

$$H^{-1}\{y(t)\} = -H\{y(t)\} \quad (\text{III}.20)$$

Equation III.21. Instantaneous Amplitude (Envelope) a(t) :

$$a(t) = \sqrt{x^2 + y^2} \quad (\text{III}.21)$$

Equation III.22. Phase θ(t) :

$$\theta(t) = arctan(\frac{y}{x}) \quad (\textbf{\textit{III}}.22)$$

The spectrum of the analytic signal $z_x(t)$ is related to the original signal spectrum by [43, 44]:

EquationIII.23. Analytic Signal Spectrum:

$$Z_x(j\omega) = X(j\omega) + jY(j\omega) = 2X(j\omega)U(\omega) \quad (\text{III}.23)$$

where U(ω) is the Heaviside unit step, which is zero for negative frequencies and unity for positive frequencies. The analytical signal thus suppresses all negative-frequency components, preserving the one-sided spectrum. The standard pairs of the Hilbert transform for common functions encountered in vibration analysis are given in Table III.1:

Signal u(t)	Hilbert Transform H{u}(t)
Sin(t)	−cos(t)

Signal u(t)	Hilbert Transform H{u}(t)
Cos(t)	Sin(t)
Sin (ωt + φ)	−cos (ωt + φ)
1 / (t² + 1)	t / (t² + 1)
Sin(t) / t	[1 − cos(t)] / t
δ(t)	1 / (πt)

Table III.1. Standard Hilbert Transform pairs [43, 44]

Figure III.1 illustrates the block diagram for computing the instantaneous amplitude (AI) and instantaneous frequency (FI) from a signal x(t) via the analytic signal $z_x(t)$:

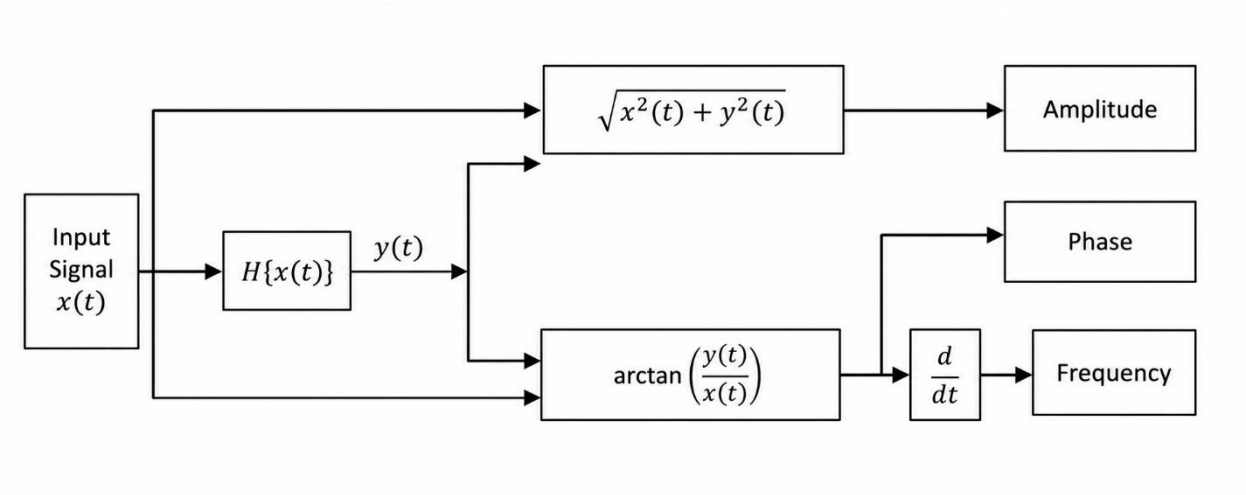


Figure III.1. Principle of estimation of instantaneous frequency (FI) and instantaneous amplitude (AI) via the analytic signal $z_x(t)$ of x(t) [44].

It is important to emphasize that the physical meaningfulness of the instantaneous frequency derived from the Hilbert transform requires the analysed signal to be a purely oscillatory, monocomponent function with a zero mean reference level. As demonstrated by Huang et al. [32], the application of the Hilbert transforms to multi-component signals or to signals riding on a non-zero mean may yield unphysical negative frequency values. This fundamental limitation directly motivated the subsequent development of the Empirical Mode Decomposition (EMD) as an indispensable preprocessing step.

III.5.2 Instantaneous Features

The instantaneous frequency *ω(t)* is obtained by differentiating the instantaneous phase function *θ(t)* with respect to time:

Equation III.24. Instantaneous Frequency:

$$\omega(t) = \frac{d\theta(t)}{dt} \quad \text{(III.24)}$$

Unlike the conventional Fourier frequency (which is a constant value characterizing the global spectral behavior of a signal over its entire duration) the instantaneous frequency is a time-varying quantity that reflects the local oscillatory behavior at each time instant. This property renders it particularly suitable for analysing non-stationary signals whose spectral content evolves over time, as commonly encountered in rotating machinery vibration signals under varying operational conditions [33].

With both the instantaneous amplitude *a(t)* and instantaneous frequency *ω(t)* defined as functions of time, the energy distribution of the signal can be represented in the joint time–frequency domain through the Hilbert spectrum H (ω, t). The marginal Hilbert spectrum is then defined as the integral of H (ω, t) over the full temporal domain [0, T] [33]:

Equation III.25. Marginal Hilbert Spectrum:

$$h(\omega) = \int_0^T H(\omega, t)\, dt \quad \textbf{(\textit{III}.25)}$$

The marginal spectrum provides a measure of the total energy contribution from each frequency value accumulated over the entire observation window, serving as a physically meaningful alternative to the classical Fourier power spectrum. Unlike the latter, it is derived from instantaneous rather than global frequency estimates, thereby yielding a more faithful representation of the signal's spectral energy content.

III.5.3 Applications in Fault Diagnosis — Envelope Detection

One of the most significant applications of the Hilbert transform in the context of rotating machinery fault diagnosis is the envelope detection technique, also known as amplitude demodulation analysis [36, 37]. This technique is particularly effective for detecting localized defects in rolling element bearings, where the fault manifests as a series of periodic impulses that amplitude-modulate a high-frequency structural resonance carrier signal. Each contact between a rolling element and a damaged surface excites the structural resonance of the bearing housing, producing a signal of the form in this equation:

Equation III.26. Amplitude-Modulated Signal Model:

$$x(t) = A(t) \cdot cos(2\pi f_c t + \varphi) \quad \textbf{(\textit{III}.26)}$$

where *fc* denotes the structural resonance (carrier) frequency, *A(t)* is the time-varying envelope carrying the fault-related information at the characteristic defect frequency, and φ is an initial phase. The envelope detection procedure consists of the following sequential steps [36, 37]:

- **Band-pass filtering:** the raw vibration signal is filtered around the structural resonance frequency band to isolate the amplitude-modulated component and suppress extraneous contributions.
- **Hilbert transform:** the Hilbert transform is applied to the filtered signal to construct the analytic signal z(t) = x(t) + iy(t).
- **Envelope extraction:** the instantaneous amplitude (envelope) a(t) = |z(t)| is computed.
- **Envelope spectrum:** the FFT of the squared envelope $a^2(t)$ yields the Envelope Spectrum. Diagnostic peaks at the fault characteristic frequencies (BPFI, BPFO, BSF, FTF) directly identify and localize the defective bearing element.

III.5.4 Discrete Hilbert Transform

In the discrete-time setting, the signal x(t) must be causal [x(t) = 0 for t < 0] and the sampled sequence x[n] is a real, non-periodic, causal series. In this case, the associated complex analytic series has a spectrum that is non-zero only over the interval of positive frequencies. The discrete Hilbert transform (DHT) is computed algorithmically by the following procedure [43, 44]:

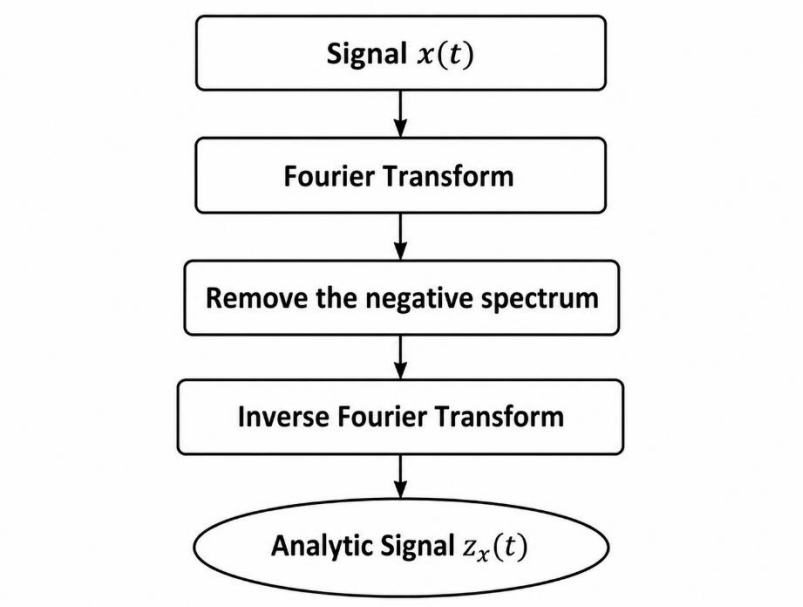


Figure III.2. Block diagram of the DHT computation algorithm: Fourier Transform, zeroing of the negative spectrum, and Inverse Fourier Transform [44]

The algorithm computes the DFT of the signal, zeros the negative-frequency coefficients, doubles the positive-frequency coefficients, and applies the inverse DFT. The result is a complex signal whose real part is the original sequence and whose imaginary part is the Hilbert-transformed sequence [43].

Figure III.3 shows the computation of the analytic signal for a sinusoidal signal using the DHT algorithm:

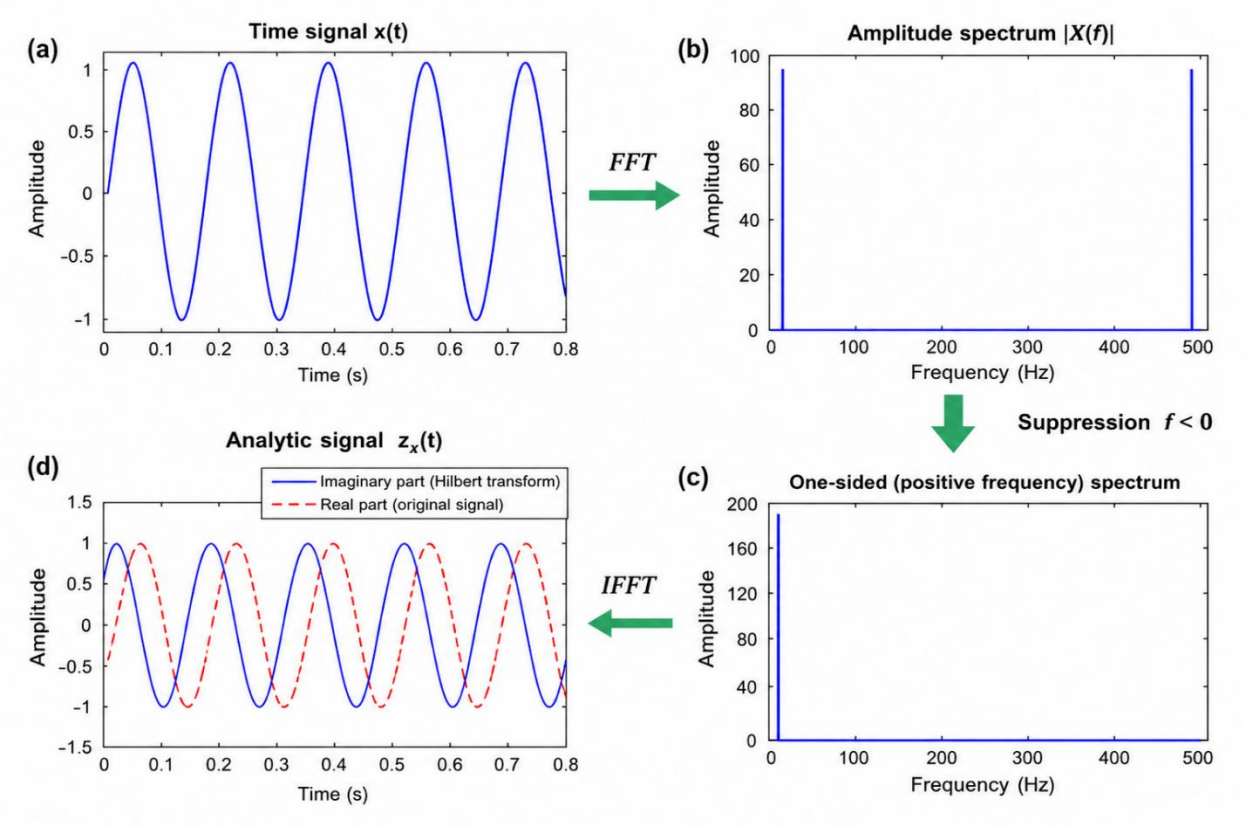


Figure III.3.Computation of the analytic signal for a sinusoidal signal: (a) original signal, (b) FFT spectrum, (c) spectrum with negative frequencies zeroed, (d) reconstructed analytic signal [44]

III.5. The Hilbert–Huang Transform (HHT)

III.6.1 Motivation

The classical signal analysis methods reviewed in Section III.4 (the Fourier Transform, the STFT, and the Wavelet Transform) rest upon fundamental assumptions of linearity and stationarity. The Fourier approach decomposes a signal onto a predefined set of trigonometric basis functions of constant frequency and amplitude, thereby implicitly assuming that the underlying process is stationary. Although mathematically rigorous, this framework generates spurious

harmonics when applied to genuinely nonlinear signals and fails to track spectral variations that evolve over time [38].

As argued by Huang and Wu [33], the physical world is intrinsically neither linear nor stationary. Real-world vibration signals from rotating machinery exhibit both nonlinear dynamics arising from contact mechanics and material nonlinearities, and non-stationary behavior due to load fluctuations, speed variations, and the transient character of fault-related impulses. As the identification of early-stage faults necessarily relies on the detection of subtle changes in the signal characteristics, an analysis method capable of handling nonlinearity and non-stationarity simultaneously is essential.

To address these limitations, Huang et al. [32] proposed an entirely adaptive, data-driven approach subsequently designated by NASA as the Hilbert–Huang Transform (HHT). In contrast to all prior methods employing *a priori* defined basis functions, the HHT derives its basis *a posteriori* directly from the data, without imposing any assumptions of linearity or stationarity. The method consists of two sequential components: the Empirical Mode Decomposition (EMD) and the Hilbert Spectral Analysis (HSA), which together enable a physically meaningful time–frequency–energy representation of complex signals.

III.6.2 Empirical Mode Decomposition and Hilbert Spectral Analysis

The central component of the HHT is the Empirical Mode Decomposition (EMD), an iterative, fully adaptive algorithm that decomposes any arbitrary signal $x(t)$ into a finite set of oscillatory components called Intrinsic Mode Functions (IMFs). Each IMF must satisfy two conditions [32, 33] :

- **Condition 1:** The total number of extrema (maxima and minima) and the total number of zero-crossings must either be equal or differ by at most one throughout the entire data length.
- **Condition 2:** At any data point, the mean value of the envelope defined by the local maxima and the envelope defined by the local minima must be identically zero.

These conditions ensure that each IMF represents a locally symmetric, physically meaningful oscillatory mode, for which the Hilbert transform yields a well-defined instantaneous frequency. The decomposition proceeds through the sifting process :

- **(i)** Identify all local maxima and minima of $x(t)$.
- **(II)** Fit cubic splines through the maxima and minima to form the upper and lower envelopes $e$max(t) and $e$min(t).

- **(III)** Compute the local mean $m_1(t)$ per **Equation** III**.26**, and subtract it from the signal to obtain the proto-IMF.
- **(iv)** Repeat the sifting on the proto-IMF until the IMF conditions are satisfied, yielding the first IMF $c_1(t)$. Extract the residue $r_1(t) = x(t) - c_1(t)$, and iterate on the residuals until the final residue is monotonic.

The sifting algorithm is summarized in Table III.2, which shows all steps of the decomposition procedure [32, 33]:

EMD Sifting Algorithm
1. Initialisation : Set c(t) = x(t), residue r(t) = x(t)
2. Sifting process: Set h(t) = c(t), then repeat: (a) Identify all local maxima and minima of h(t) (b) Fit cubic splines to compute upper $e_{max}(t)$ and lower $e_{min}(t)$ envelopes (c) Compute local mean : $m(t) = [e_{max}(t) + e_{min}(t)] / 2$ (d) Update : $h(t) = h(t) - m(t)$ Repeat (a)–(d) until h(t) satisfies the IMF conditions (stopping criterion)
3. IMF extraction : $IMF_i(t) = h(t)$
4. Residue update : $c(t) = c(t) - IMF_i(t)$
5. Iterate: Repeat steps 2–4 on the residue c(t) until c(t) has at most two extrema
6. Final residue : r(t) = c(t) (monotonic trend)

Table III.2. EMD Sifting Process Algorithm [32, 33]

The stopping criterion for the sifting process ensures that each extracted IMF is genuinely oscillatory while avoiding over-sifting. A practical criterion proposed by Huang et al. [32] replaces the strict zero-mean condition with the following inequality, evaluated at every time instant t within the observation window [a, b] [32, 33]:

Equation III.27. IMF Stopping Criterion:

$$|U(t) + L(t)| \leq \varepsilon |U(t) - L(t)| \qquad (\boldsymbol{III.27})$$

where U(t) is the upper envelope, L(t) is the lower envelope, and ε is a small positive threshold (typically 0.2). This criterion prevents the envelopes from being overly constrained whilst ensuring that the IMF remains symmetric about the zero axis. The number of sifting iterations required to satisfy this criterion varies depending on the complexity of the signal.

To illustrate the EMD decomposition, consider a test signal x(t) composed of three sinusoidal components at f_1 = 60 Hz, f_2 = 25 Hz, and f_3 = 10 Hz [44]:

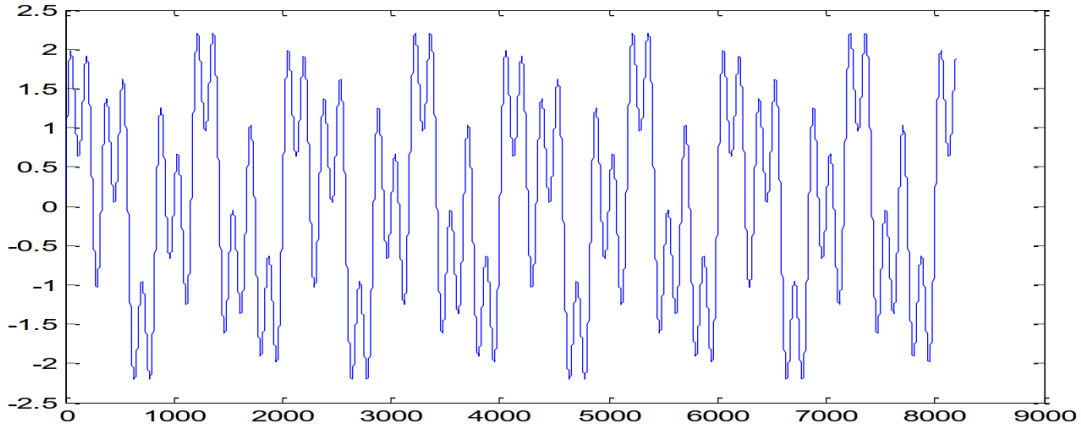


Figure III.4. Composite test signal $x(t) = x_1(t) + x_2(t) + x_3(t)$ used to illustrate the EMD algorithme [44]

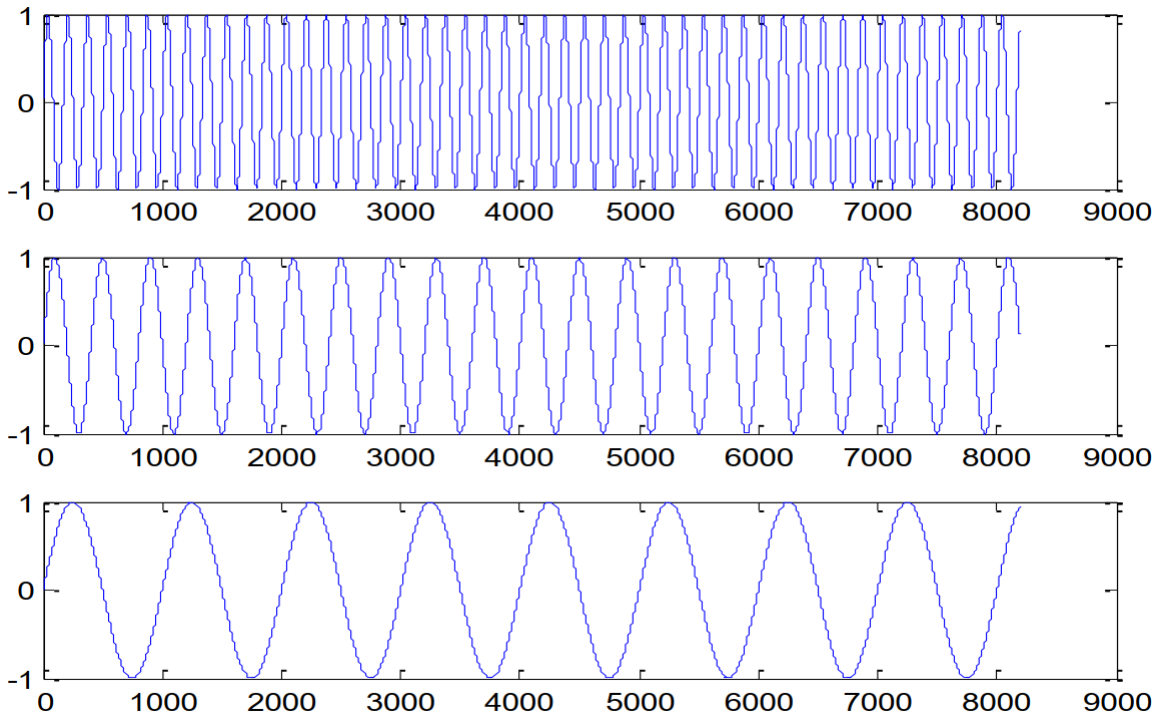


Figure III.5. The three sinusoidal components $x_1(t)$, $x_2(t)$, and $x_3(t)$ constituting the test signal [44].

The upper and lower envelopes of the signal are computed by cubic spline interpolation through the local maxima and minima, respectively. The local mean m(t) is defined as their semi-sum (Equation III.26). Figure III.6 illustrates the envelope computation for the test signal:

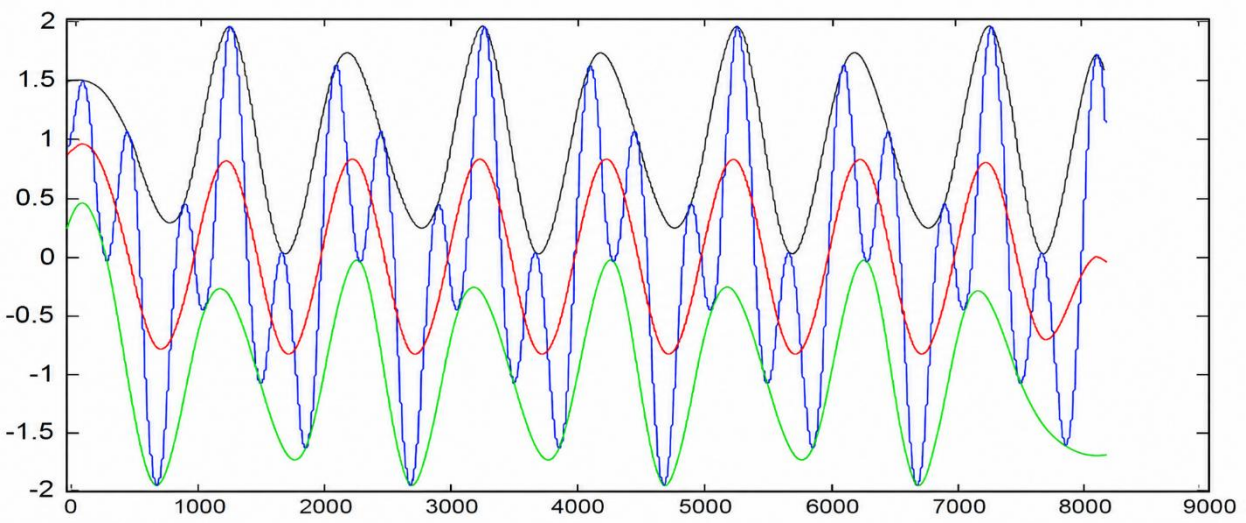


Figure III.6. Upper envelope (black), lower envelope (green), and local mean m(t) (red) computed for the test signal by cubic spline interpolation [44]

Figure III.7 shows the first iteration (iteration 0) of the sifting process: the signal before sifting (proto-IMF with its envelopes) and after subtracting the local mean, along with the resulting residue:

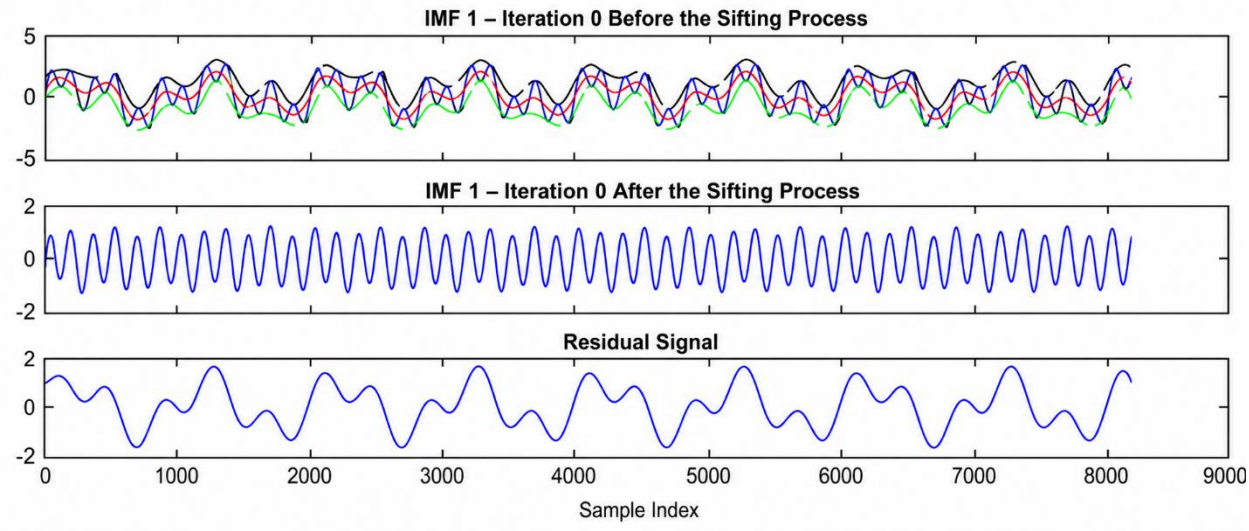


Figure III.7. Sifting process iteration 0: (top) proto-IMF with envelopes before sifting, (middle) result after subtracting local mean, (bottom) residue [44]

Three successive sifting iterations are typically required to extract the first IMF component from the test signal, as illustrated in Figure III.8:

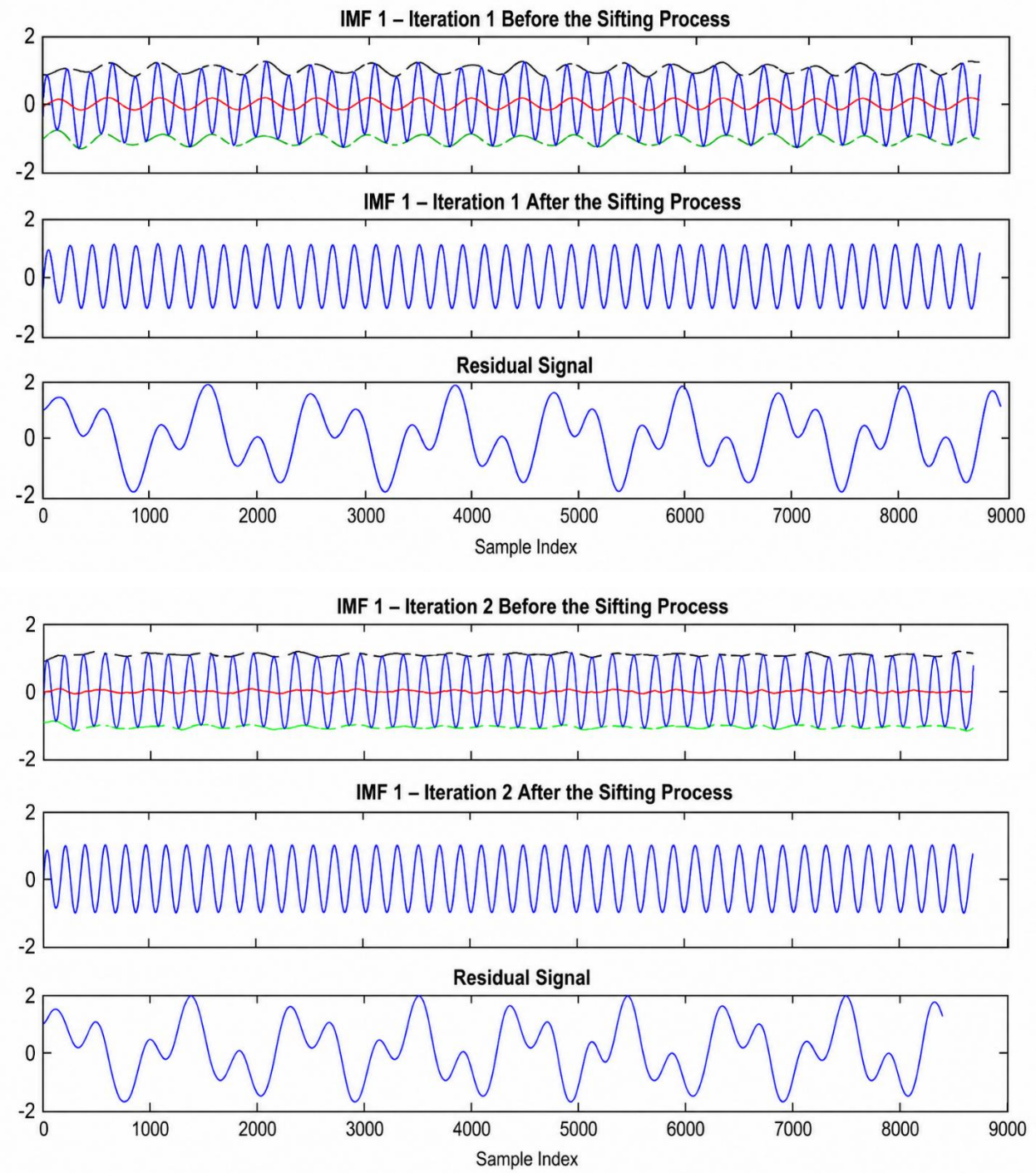


Figure III.8. Three successive sifting iterations for the extraction of IMF_1: before sifting (left column) and after sifting (right column) at each iteration, with residue (bottom) [44].

At the end of the sifting process, the first IMF (IMF1) is recovered. This first component is then subtracted from the original signal; the signal resulting from this operation is called the residue. Figures (III.9) and (III.10) show the shapes of the first component IMF1 and the residue. The residue signal is then used in the sifting process in place of the original signal to extract the second IMF component (IMF2).

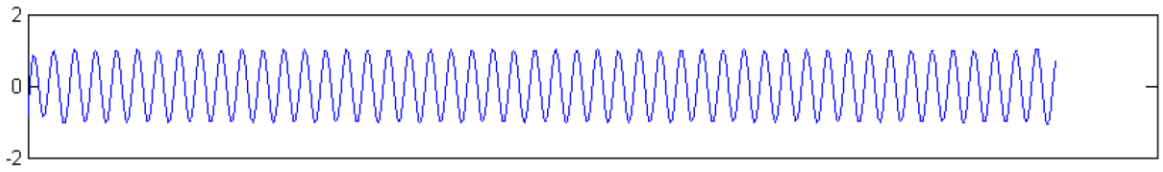


Figure III.9. Representation of IMF1

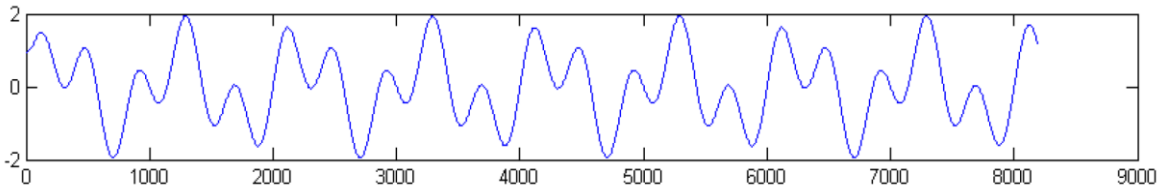


Figure III.10. Representation of the residue after extraction of IMF1

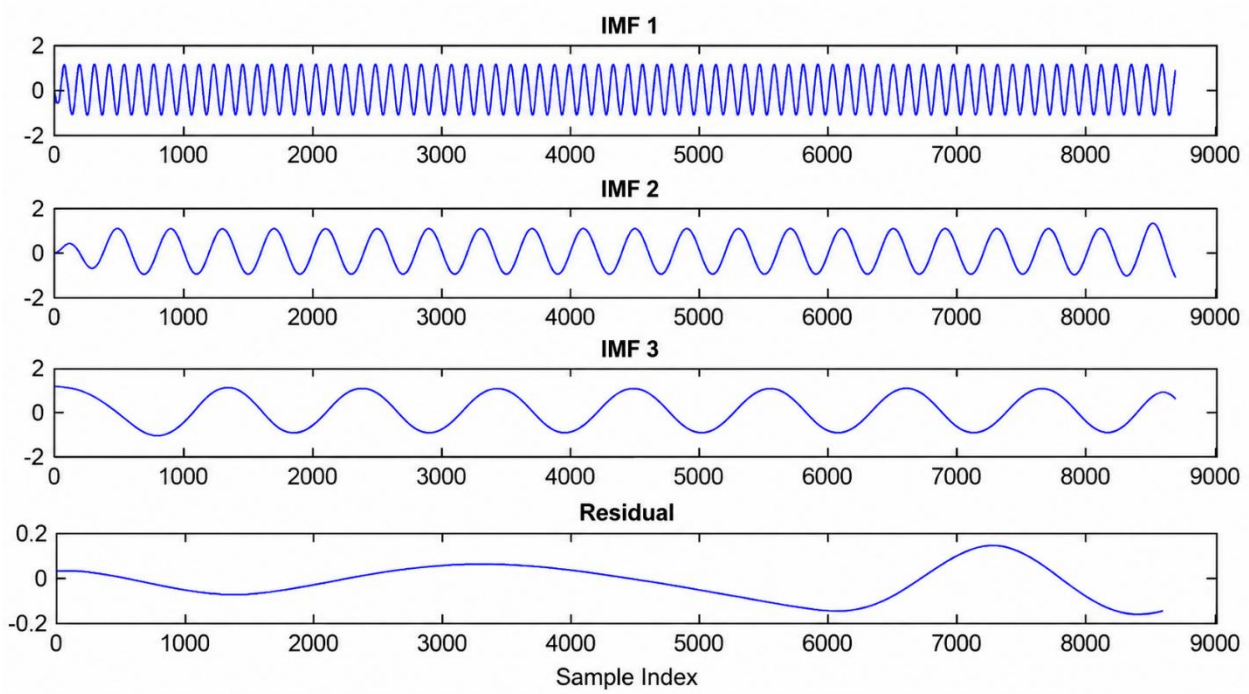


Figure III.11. All IMFs and the final residue of the signal x(t).

Figure III.11 shows the appearance of IMF2. The subtraction and sifting operation of the residue is then repeated until a stopping criterion is satisfied. The last IMF is called the final residue. Figure III.11 shows all the IMFs and the final residue obtained from the signal in figure III.4. The first 3 IMFs are similar to the three signals making up the original signal x(t).

In figure III.11, it can be noted that the first 03 IMFs are equal to the three signals constituting the signal x(t), and the last IMF represents the residue.

The mean envelope at each sifting step is given by:

Equation III 0.28. Local Mean Envelope (EMD Sifting):

$$m_1(t) = \frac{e_{max}(t) + e_{min}(t)}{2} \quad \text{(III.28)}$$

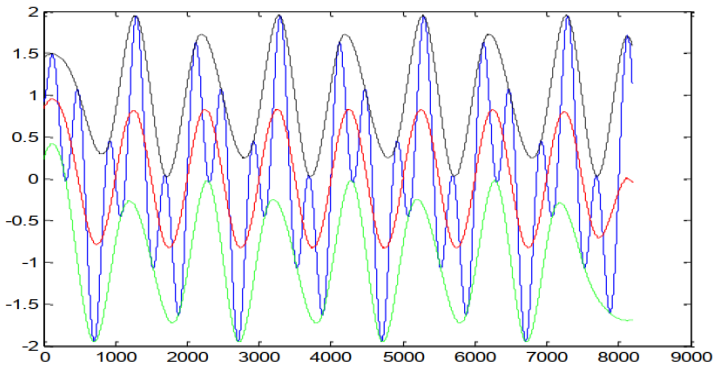


Figure III.12. Representation of the upper and lower envelopes as well as the mean of a signal.

The final EMD decomposition of the signal is expressed as:

Equation III.29. EMD Final Decomposition:

$$x(t) = \sum_{j=1}^{n} c_j(t) + r_n(t) \quad \text{(III.29)}$$

where $c_j(t)$ are the IMFs ordered from highest to lowest frequency, and $r_n(t)$ is the final residual representing the overall trend of the signal. The EMD operates entirely in the time domain and imposes no a priori basis, rendering the decomposition fully adaptive to the local characteristics of the data [32, 34].

Following decomposition, the Hilbert transform is applied to each IMF $c_j(t)$ to extract the corresponding instantaneous amplitude and frequency. The original signal is then represented as [33]:

Equation III.30. Hilbert Spectral Analysis (HSA):

$$x(t) = Re\left\{\sum_{j=1}^{n} a_j(t) \cdot e^{i\omega_j(t)\,dt}\right\} \quad \text{(III.30)}$$

This expression constitutes the Hilbert Spectral Analysis (HSA). Unlike the Fourier expansion (in which both amplitude and frequency are constants) the HHT expansion allows both quantities to vary with time. This fundamental generalization lifts the restriction of constant frequency and enables the method to capture the intrawave frequency modulation characteristic of nonlinear oscillators, without resorting to spurious harmonics [33].

III.6.3 The Hilbert Spectrum

The Hilbert Spectrum H (ω, t) is constructed by distributing the instantaneous energy $a^2_j(t)$ of each IMF at its corresponding instantaneous frequency $\omega_j(t)$ across the time–frequency plane. The result is a three-dimensional representation that simultaneously encodes energy, frequency, and time, providing a high-resolution picture of the spectral evolution of the signal [33].

Integrating the Hilbert Spectrum over the observation interval yields the marginal Hilbert spectrum (**Equation III.23**), which represents the total accumulated energy at each frequency. Whereas the Fourier spectrum smears the energy of a time-localized event across all frequencies due to its global convolution basis, the Hilbert spectrum attributes energy contributions precisely to the correct frequency and time instant, yielding a sharper and more physically representative estimate.

A comparative summary of the key characteristics of the three primary signal processing approaches considered in this chapter is presented in Table III.3. As demonstrated by Huang and Wu [33], the HHT consistently yields sharper results than traditional methods and is uniquely capable of capturing the intrawave frequency modulation arising from nonlinear dynamics without spurious harmonic artefacts.

Criterion	Fourier (FFT)	Hilbert Transform	HHT (EMD+HSA)
Basis	A priori (fixed)	A priori (fixed)	Adaptive (a posteriori)
Stationarity	Required	Partially relaxed	Not required
Nonlinearity	No	No	Yes
Time resolution	None	Partial (envelope)	Full (instantaneous)
Freq. resolution	High (global)	Moderate	High (instantaneous)
Spurious harmonics	Yes	Possible	No
Feature extraction	Limited	Envelope-based	Comprehensive
Computational cost	Low	Low – Moderate	High
Theoretical base	Complete	Complete	Empirical

Table III..3 Comparative Analysis: Fourier, Hilbert, and HHT Methods [33]

Despite its demonstrated effectiveness, the HHT currently lacks a complete and rigorous mathematical foundation, a limitation explicitly acknowledged by Huang and Wu [33]. Outstanding issues include the formal proof of convergence of the sifting process and the uniqueness of the resulting IMF set. A significant practical concern is the phenomenon of mode

mixing, wherein a single IMF may contain oscillations of widely disparate scales. This issue has been partially addressed through the Ensemble EMD (EEMD) [35], a noise-assisted variant that improves the physical interpretability of the decomposition through ensemble averaging over multiple realizations with added white noise.

III.7. Conclusion

This chapter has presented the theoretical framework underpinning the signal analysis methodology adopted in this work for rotating machinery fault diagnosis. Beginning with a lumped-parameter mechanical model that establishes the physical relationship between structural faults and vibration signatures, the chapter systematically reviewed the principal signal processing techniques from classical to adaptive methods.

The Fourier Transform provides a rigorous decomposition of stationary signals but fails to track temporal variations in spectral content. The Short-Time Fourier Transform (STFT) partially addresses this limitation at the cost of a fixed time–frequency resolution trade-off governed by Heisenberg's uncertainty principle. The Continuous Wavelet Transform (CWT) offers multi-resolution analysis but remains constrained by its a priori choice of basis function, which may not faithfully represent the nonlinear dynamics present in machinery signals.

The Hilbert Transform was introduced as a fundamental operator for constructing the analytic signal, enabling the extraction of physically meaningful instantaneous amplitude and instantaneous frequency. Its principal application in fault diagnosis (envelope detection) was detailed, demonstrating how bearing defect frequencies are revealed in the envelope spectrum following band-pass filtering and amplitude demodulation.

Finally, the Hilbert–Huang Transform (HHT) was presented as a fully adaptive, data-driven framework composed of Empirical Mode Decomposition (EMD) and Hilbert Spectral Analysis (HSA). Unlike all preceding methods, the HHT imposes no a priori basis functions and requires no assumptions of linearity or stationarity, making it uniquely suited to the analysis of the nonlinear, non-stationary vibration signals generated by faulty rotating machinery. The theoretical foundations established in this chapter directly inform the signal processing methodology applied in the subsequent experimental analysis.

Chapter IV

Application of the FFT and the HHT to Rolling Bearing Fault Diagnosis

IV.1 Introduction

A rolling bearing is a fundamental component that provides a mobile connection between two elements of a mechanism rotating relative to one another. Its function is to allow the relative rotation of these elements under load, with precision and minimal friction. Rolling bearings are found in a wide range of applications, including industrial machinery, automotive systems, aeronautics, and robotics.

Bearings are distinguished by the shape and arrangement of their rolling elements. Each model exhibits specific performance characteristics and is therefore suited to a particular application. For example, roller bearings support higher loads compared to ball bearings of equivalent size, because the contact between the rolling elements and the raceways is linear. However, they operate at lower rotational speeds.

IV.2 Bearing Under Study

The bearing selected for this study is the SKF 6205-2RS JEM deep-groove ball bearing. The general structure of rolling bearings (comprising inner ring, outer ring, rolling elements, and cage) as well as the fault degradation mechanisms and the four-stage wear progression model, were presented in detail in Chapter II (Sections II.6.3). The reader is referred to that chapter for the theoretical background. The present section focuses on the specific geometric parameters of the SKF 6205 bearing and the experimental dataset used for fault diagnosis.

IV.3 Bearing System Under Study

IV.3.1 Bearing Data Center" Bearing Test Rig"

The vibration signals (accelerations) used in this study were obtained from the publicly available dataset provided by the **Case Western Reserve University (CWRU) Bearing Data Center** [23]. The signals were measured at a sampling frequency of Fe = 48 kHz over a duration of 10 seconds, using a three-phase electric motor rated at 1.5 kW, coupled to a mechanical load that determines its operating speed. The data acquisition system is equipped with anti-aliasing low-pass filters at the input stage. Since the maximum frequency of the vibration signals does not exceed 5 kHz, the chosen sampling frequency is adequate.

The data were acquired from rolling bearings under various load conditions and different bearing health states. As illustrated in Figure IV.1, the ball bearings are installed in an induction motor driven by a mechanical system.

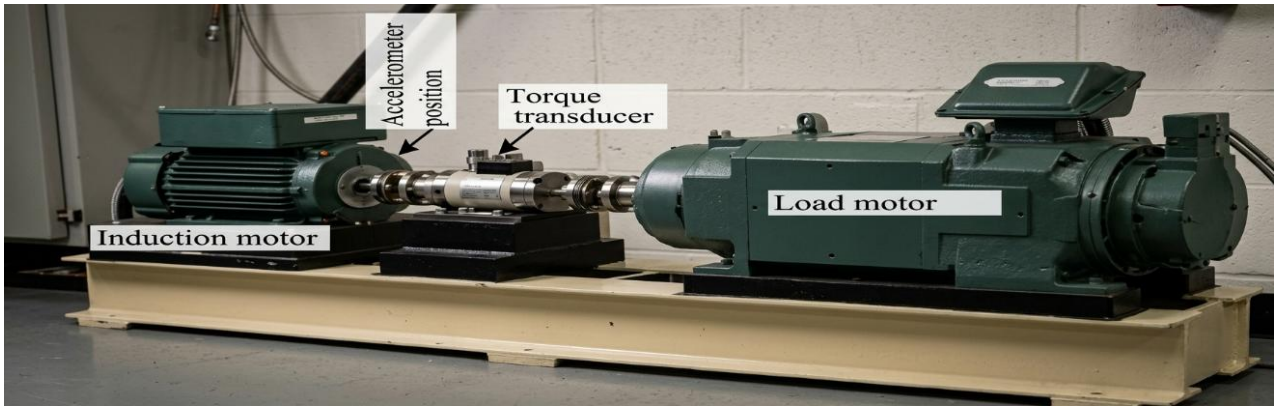


Figure IV.1 Bearing test rig.

The bearings used in this study are SKF 6205 deep-groove ball bearings.

Inner race, outer race, and ball defects were introduced into the bearings using Electrical Discharge Machining (EDM). EDM is a metal processing technique used for hard metals or mechanical components that cannot be penetrated by conventional machining methods. The resulting defect takes the form of a circular pit, whose size is defined by its diameter. The defect diameters are 0.178 mm, 0.356 mm, 0.533 mm, and 0.711 mm, corresponding to incipient, moderate, severe, and very severe faults, respectively.

Each bearing was tested under four different load conditions (0, 1, 2, and 3 HP). For these four load conditions, the signals were measured at rotational speeds of approximately 1797 rpm, 1772 rpm, 1750 rpm, and 1730 rpm, respectively. All data were acquired using accelerometers mounted on the motor housing via magnets, under four different operating conditions: normal state, ball fault (BF), inner race fault (IRF), and outer race fault (ORF).

The sensors are placed at the 12 o'clock position (vertical) for ball faults and inner ring faults. Since outer race defects are stationary, the angular position of the defect relative to the bearing load zone directly influences the vibratory response of the motor-bearing system. To account for this effect, tests were conducted with outer race defects placed at the 3 o'clock (directly in the load zone), 6 o'clock (orthogonal to the load zone), and 12 o'clock positions, as illustrated in Figure IV.2.

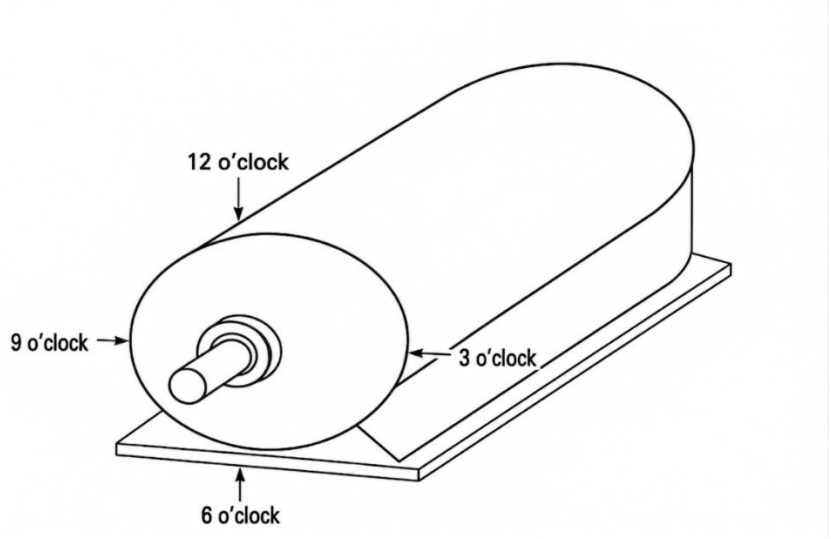


Figure IV.2 Sensor placement positions.

Figure IV.3 shows sample time-domain vibration signals for both healthy and defective bearings.

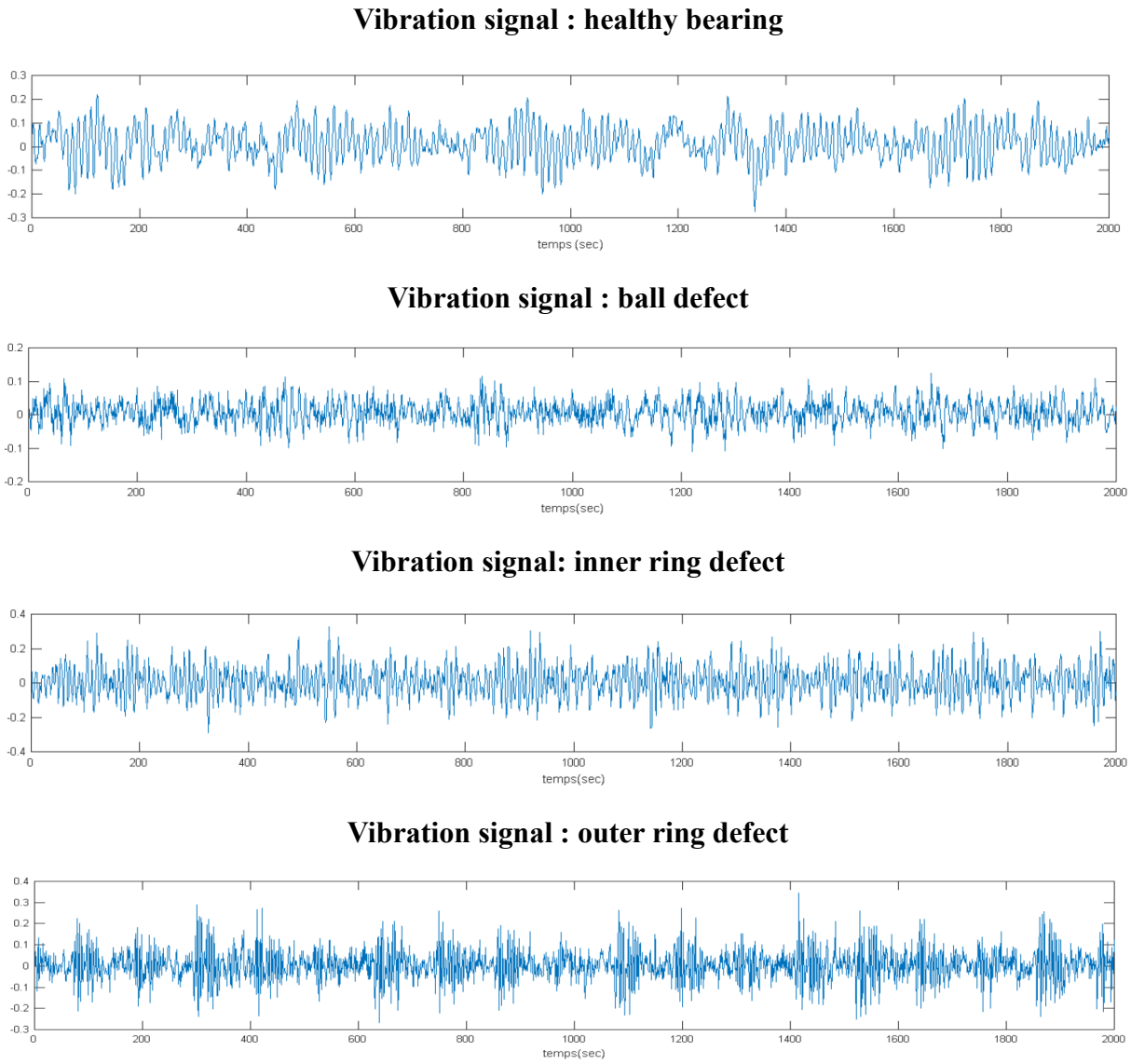


Figure IV.3 Vibration signals for healthy and defective bearings.

IV.3.2 Dataset Construction

The objective of this work is the detection of bearing faults, which requires a sufficiently rich dataset. As previously mentioned, the Case Western Reserve University (CWRU) database is used with the following specifications:

- **Single load case:** rotational speed of 1797 rpm (0 HP) and 1730 rpm (3 HP), used for the FFT-based spectral analysis The HHT analysis to evaluate performance under same operating conditions.
- **Sampling frequency : 48** kHz.
- **Three bearing health conditions:** Normal, Inner Race Fault, Outer Race Fault.

- **Two fault diameters:** 0.178 and 0.356.

With a recording duration of approximately 10 seconds and a sampling frequency of 48,000 samples/second.

IV.4 Analysis Methods

Various vibration analysis tools exist to detect and diagnose the onset of faults in rolling bearings. Numerous publications synthesize these different methods and tools. They are generally classified into two broad families.

IV.4.1 Frequency-Domain Descriptors

Frequency-domain descriptors are among the most widely used indicators for identifying the location of a fault. Defective bearings generate vibrations at frequencies equal to the rotational speeds of each bearing component.

Figure IV.4 illustrates the manufacturing dimensions of a bearing:

- **BD :** Ball Diameter.
- **PD :** Pitch Diameter.
- θ **:** Contact Angle (the angle between the bearing contact line and the radial direction ; $\theta = 0$).
- **n:** Number of rolling elements (n = 9).

The rotational frequency f_r for a rotational speed of

N (0HP) = 1797 rpm is $f_r = N / 60 = 29.95$ Hz

N (3HP) = 1730 rpm is $f_r = N / 60 = 28.83$ Hz

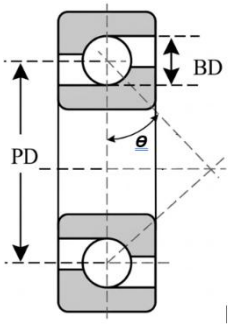


Figure IV.4 Geometric characteristics of a rolling bearing.

IV.5 Characterization of Spectral Signatures of Bearing Faults

Based on the characteristics of the SKF 6205-2RS JEM bearing given in Table IV.1:

Inner Diameter (mm)	Outer Diameter (mm)	Thickness (mm)	Ball Diameter BD (mm)	Pitch Diameter PD (mm)
25	52	15	8	39

Table IV.1 Bearing characteristics and fault frequencies.

The Theoretical frequencies are determined from the bearing geometry and the machine kinematics. They are given by the **Equation II:1. to Equation II.2.**:

Load	$BPFO$ (Hz)	BPFI(Hz)
0 (HP)	107.12	162 .42
3 (HP)	103.12	156.34

Table IV.2 Theoretical frequencies of the SKF 6205-2RS JEM bearing.

Since most bearing vibrations are periodic, it is straightforward to extract frequency-domain descriptors using the Fourier transform via the well-known FFT algorithm.

As previously mentioned, the dataset used consists of signals each containing 2000 samples acquired at a sampling frequency of 12 kHz. The Fourier transform procedure with a 2048-point FFT is expressed as the next equation:

Equation IV.1. Fast Fourier Transform (FFT):

$$D(k) = \sum_{n=0}^{N-1} d(n) \cdot e^{-j2\pi kn/N}, \quad k = 0,1, \dots, N-1 \qquad \textbf{(IV.1)}$$

The Power Spectral Density (PSD) is obtained the next equation:

Equation IV.2. (PSD) DC Component:

$$P(0) = |D(0)|^2 \qquad \textbf{(IV.2)}$$

Where D (0) is the zeroth FFT coefficient, equal to the sum of all N signal samples. No scaling factor is applied because the DC component has no symmetric counterpart in the negative-frequency half of the spectrum. In practice, since vibration signals are zero-meaned prior to analysis, P (0) is negligible and carries no fault-diagnostic information.

Equation IV.3. (PSD – General Term:

$$P(k) = |D(k)|^2 + |D(N-k)|^2, \quad k = 1,2, \dots, \frac{N}{2} - 1 \qquad \textbf{(IV.3)}$$

where D(k) and D (N − k) are the FFT coefficients at the positive and negative frequency bins respectively. Since the signal is real-valued, D (N − k) is the complex conjugate of D(k), and both terms carry equal energy. Summing them explicitly combines the contributions of both symmetric

halves of the two-sided spectrum into a single one-sided estimate. This equation is the central tool of the spectral analysis performed in this chapter: peaks in P(k) at frequencies coinciding with the theoretical bearing fault frequencies (BPFO, BPFI, BSF) indicate the presence of the corresponding defect.

Equation IV.4. (PSD) Nyquist Component:

$$P\left(\frac{N}{2}\right) = \left|D\left(\frac{N}{2}\right)\right|^2 \quad \textbf{(IV.4)}$$

The Nyquist component uses only a single squared magnitude term because the frequency bin at k = N/2 corresponds exactly to $f_s/2$, whose negative-frequency mirror image falls on the same point and is therefore not a distinct component. Adding a second identical term as in Equation IV.3 would incorrectly double its energy contribution. In the present study, with a sampling frequency of 12 kHz, the Nyquist frequency is 6 kHz (well above the bearing fault characteristic frequencies, which lie below 200 Hz) so this component plays no role in the diagnostic interpretation and is included solely for mathematical completeness of the PSD estimator.

Frequency signatures are then derived to represent the various vibrations emanating from the bearings. These descriptors, representing the fundamental frequencies, are constructed from the power spectral density, with amplitudes depending on the fault present. To account for spectral leakage during descriptor computation, a frequency band of 5 Hz is considered around each fundamental frequency Band $= [f - 2.5,\ f + 2.5]$ Hz, here f is the fundamental frequency. For each characteristic frequency, the spectral amplitude is expressed as the next equation:

Equation IV.5. Spectral Amplitude Descriptor:

$$A(f) = \sum_{f_k=f-2.5}^{f+2.5} P\left(\left[\frac{f_k}{\Delta f}\right]\right), \quad \Delta f = \frac{1}{N \cdot T_e} \quad \textbf{(IV.5)}$$

where Te is the sampling period and N is the total number of samples used. The spectral amplitudes at frequencies BPFO and BPFI are denoted X_{BPFO} and X_{BPFI} respectively.

IV.5.1 Spectral Signature of the Healthy Bearing (No-Load Condition)

In this first step, the spectrum of the bearing vibration signal in its healthy, no-load state is analyzed. This spectrum is used as the reference for all subsequent tests.

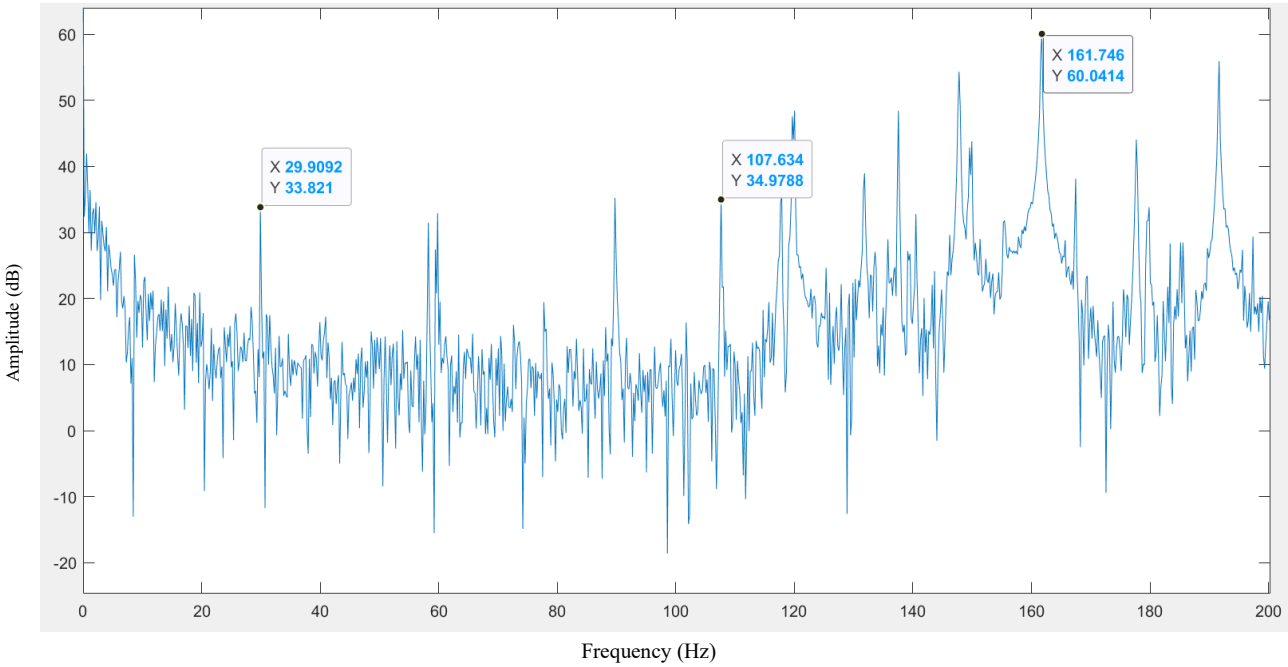


Figure IV.5 Spectrum of the healthy bearing (no-load) with the characteristic fault frequencies.

The figure presents the spectrum of the healthy no-load bearing. It shows spectral lines at the following characteristic frequencies:

- **fr = 29.9 Hz:** motor rotational frequency.
- **BPFI= 161.74 Hz:** characteristic frequency of the inner race; amplitude = **60.04 dB.**
- **BPFO = 107.63 Hz:** characteristic frequency of the outer race; amplitude = **34.97 dB.**

Remark: For fault detection and identification, it is sufficient to compare the spectra obtained in each case with the reference spectrum. This comparison reveals any variation in the amplitude of certain spectral lines or the appearance of new frequencies.

IV.5.2 Spectral Signature of the Outer Race Fault

Figure IV.6 presents the spectrum of the bearing vibration signal with an outer race fault (no-load condition) for a fault diameter of 0.178 mm. Comparing this spectrum with the reference reveals a variation in the spectral line amplitude at BPFO = 107,614 Hz, which shifts from **34.97** dB in the healthy state to **42.98** dB in the faulty state. This increase in amplitude confirms the presence of an outer race defect with a diameter of 0.178 mm.

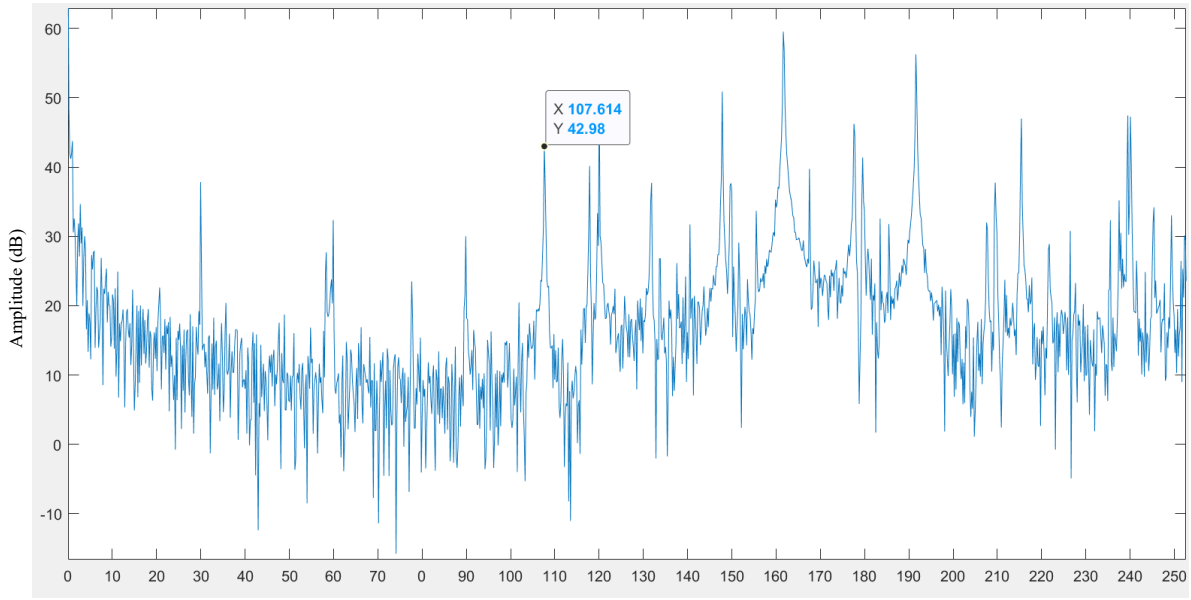


Figure IV.6 Spectrum of the bearing with outer race fault (no-load) for a fault diameter of 0.178 mm on 6 o'clock position.

IV.5.3 Spectral Signature of the Inner Race Fault

Figure IV.7 presents the spectrum of the bearing vibration signal with an inner race fault (no-load condition) for a fault diameter of 0.178 mm. Comparison with the reference spectrum shows a variation in the spectral line amplitude at BPFI = 161,74 Hz, shifting from **60.04** dB in the healthy state to **66.58** dB in the faulty state. This amplitude change is consistent with the presence of an inner race defect with a diameter of 0.178 mm, suggesting the onset of a detectable fault at this frequency.

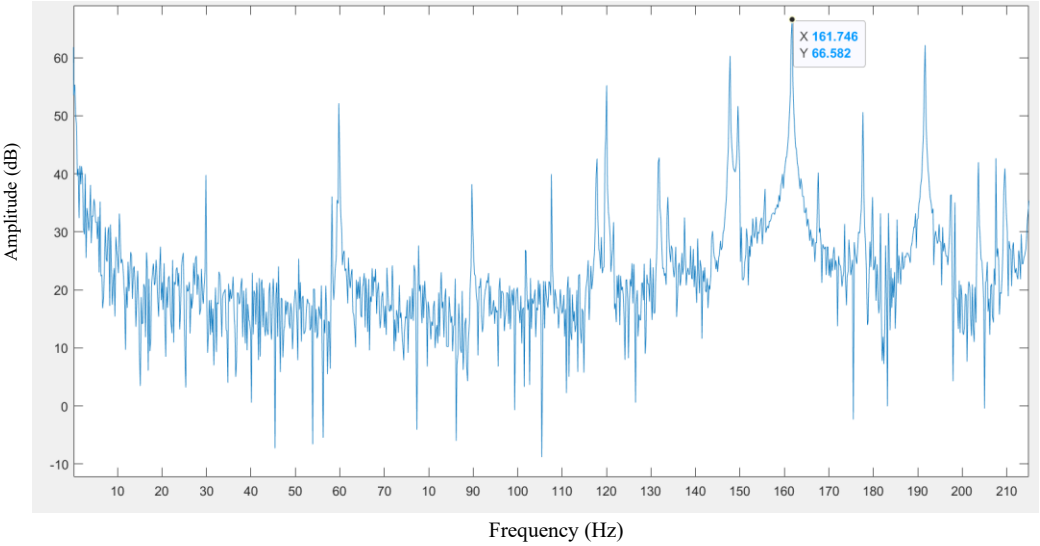


Figure IV.7 Spectrum of the bearing with inner race fault (no-load) for a fault diameter of 0.178 mm.

Fault Type	Theoretical (Hz)	Experimental Healthy (Hz)	Experimental Faulty (Hz)	Healthy Amplitude (dB)	Faulty Amplitude (dB)	Difference (dB)
Inner Race	162.42	161.74	161,74	60.04	66.58	6.54
Outer Race	107.12	107.63	107,614	34.97	42.98	8.01

Table IV.3 Theoretical and experimental frequencies and amplitudes values (no-load), fault diameter: 0.178 mm.

The experimental values correspond closely to the theoretical values. These results confirm the presence of the defect in the outer race and inner race,

IV.5.4 Spectral Signature of the Healthy Bearing Under Load (3 HP)

In this step, the vibration signal spectrum of the bearing in its healthy state under a load of 3 HP is analyzed.

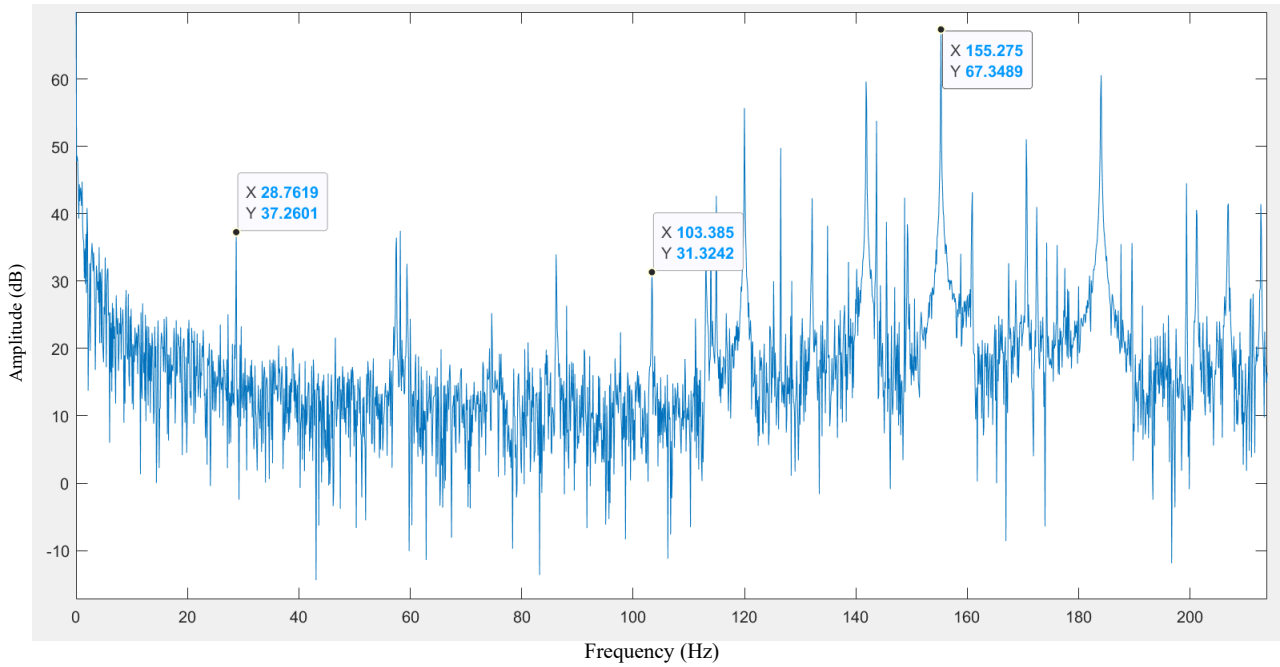


Figure IV.8 Spectrum of the healthy bearing under 3 HP load with characteristic fault frequencies.

The figure presents the spectrum of the healthy bearing under load. It shows spectral lines at the following characteristic frequencies:

- **Fr = 28.76 Hz:** motor rotational frequency.
- **BPFI= 155.27 Hz:** characteristic frequency of the inner race; amplitude = **67.34 dB.**
- **BPFO = 103.38 Hz:** characteristic frequency of the outer race; amplitude = **31.32 dB.**

Remark: For fault detection and identification, it is sufficient to compare the spectra obtained in each case with the reference spectrum.

IV.5.5 Spectral Signature of the Outer Race Fault Under Load (3 HP)

Figure IV.9 presents the spectrum of the bearing with an outer race fault under a 3 HP load for a fault diameter of 0.356 mm. Comparing this spectrum with the reference reveals a variation in the amplitude of the spectral line at BPFO = 103.26 Hz, the observed amplitude increase from 31.32 dB to 38.21 dB is consistent with the presence of an outer race defect with a diameter of 0.356 mm.

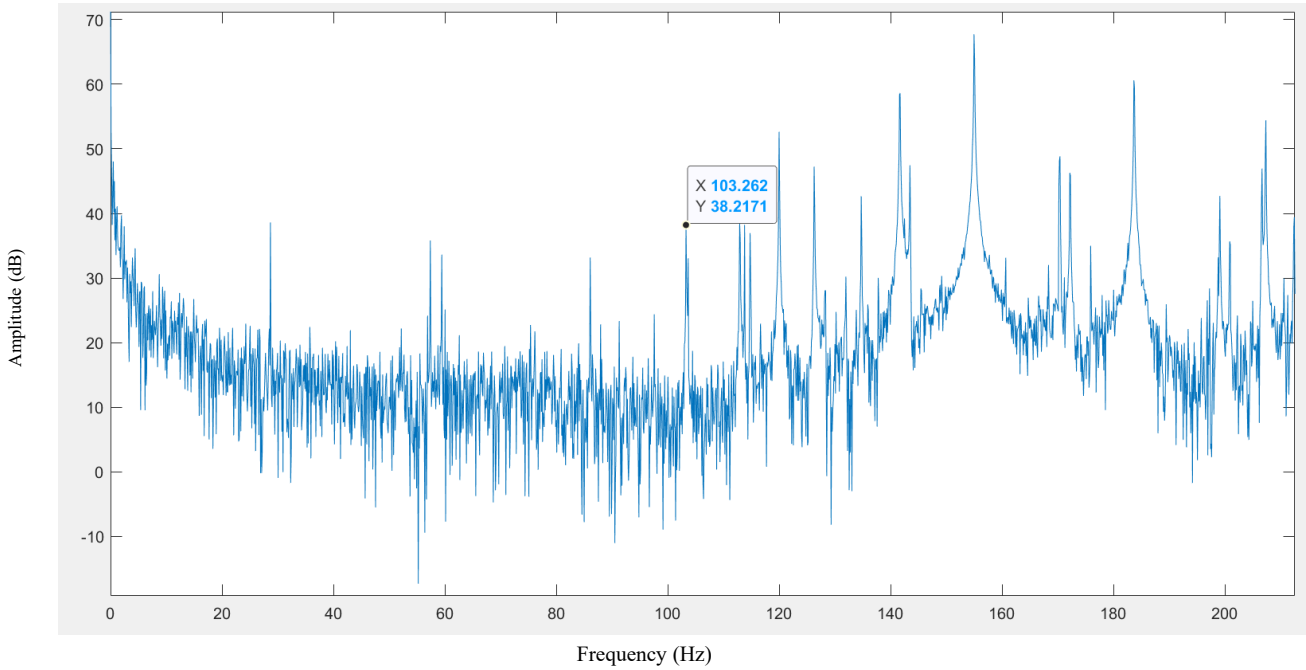


Figure IV.9 Spectrum of the bearing with outer race fault under 3 HP load, fault diameter: 0.356 mm on 6 o'clock position.

IV.5.6 Spectral Signature of the Inner Race Fault Under Load (3 HP)

Figure IV.10 presents the spectrum of the bearing with an inner race fault under a 3 HP load for a fault diameter of 0.356 mm. Comparison with the reference spectrum shows that the amplitude of the spectral line at BPFI = 155.36Hz remained nearly unchanged, exhibiting only a slight increase from 67.34 dB to 67.78 dB. This minor variation indicates that the FFT analysis was not sufficiently sensitive to clearly reveal the presence of the defect at this fault size.

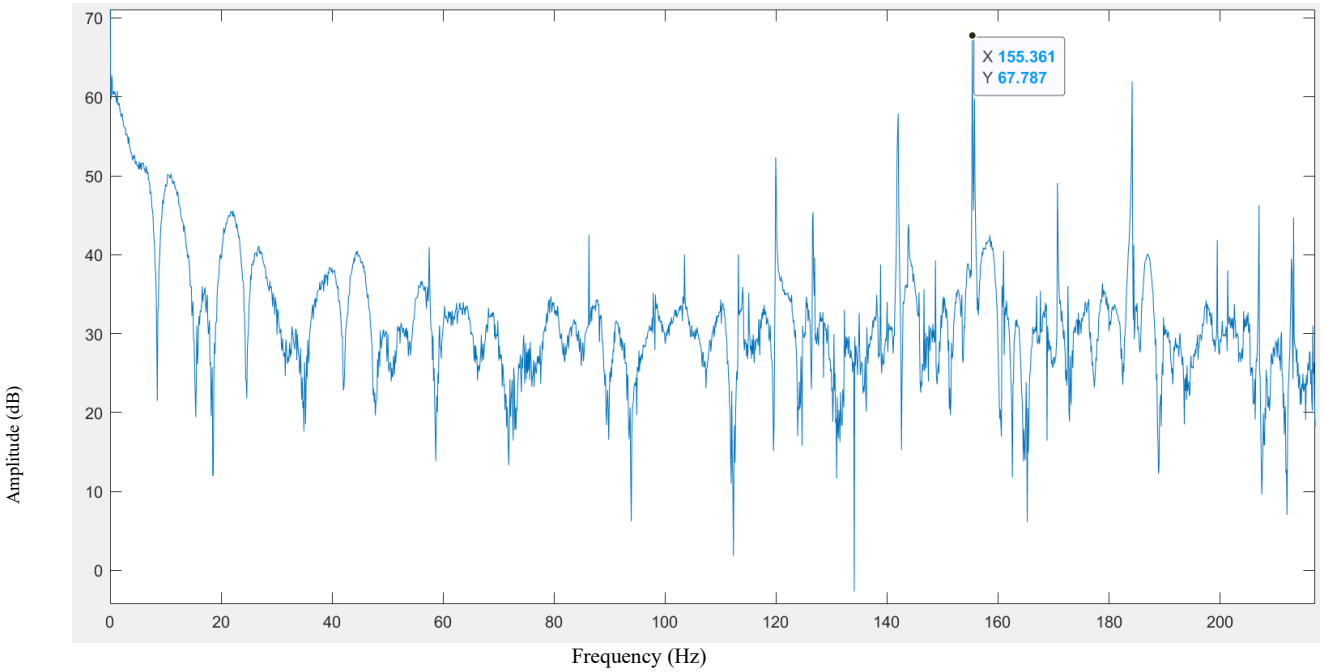


Figure IV.10 Spectrum of the bearing with inner race fault under 3 HP load, fault diameter: 0.356 mm.

Fault Type	Theoretical (Hz)	Experimental Healthy (Hz)	Experimental Faulty (Hz)	Healthy Amplitude (dB)	Faulty Amplitude (dB)	Difference (dB)
Inner Race	156.34	155.27	157.58	67.34	67.78	0.44
Outer Race	103.12	103.38	103.26	31.32	38.21	6.89

Table IV.4 Theoretical and experimental harmonic values under load (3 HP), fault diameter: 0.356 mm.

The experimental results are consistent with the theoretical values, confirming the outer race fault indicators. However, the inner race fault was not clearly identified using the FFT analysis under the considered operating conditions.

IV.6 Fault Signal Analysis Using the Hilbert-Huang Method

Figures IV.11- IV.13 show the time-domain signatures corresponding respectively to a healthy bearing and bearings with different fault diameters (0.178 mm and 0.356 mm).

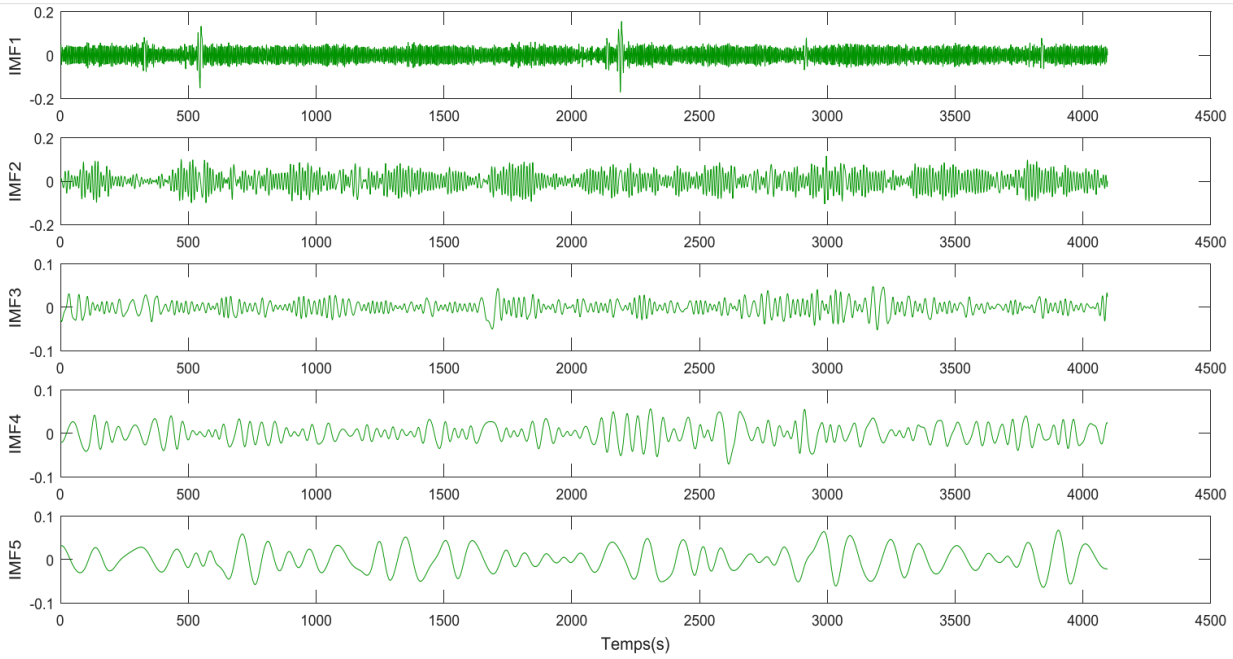


Figure IV.11 IMFs of the healthy bearing signal.

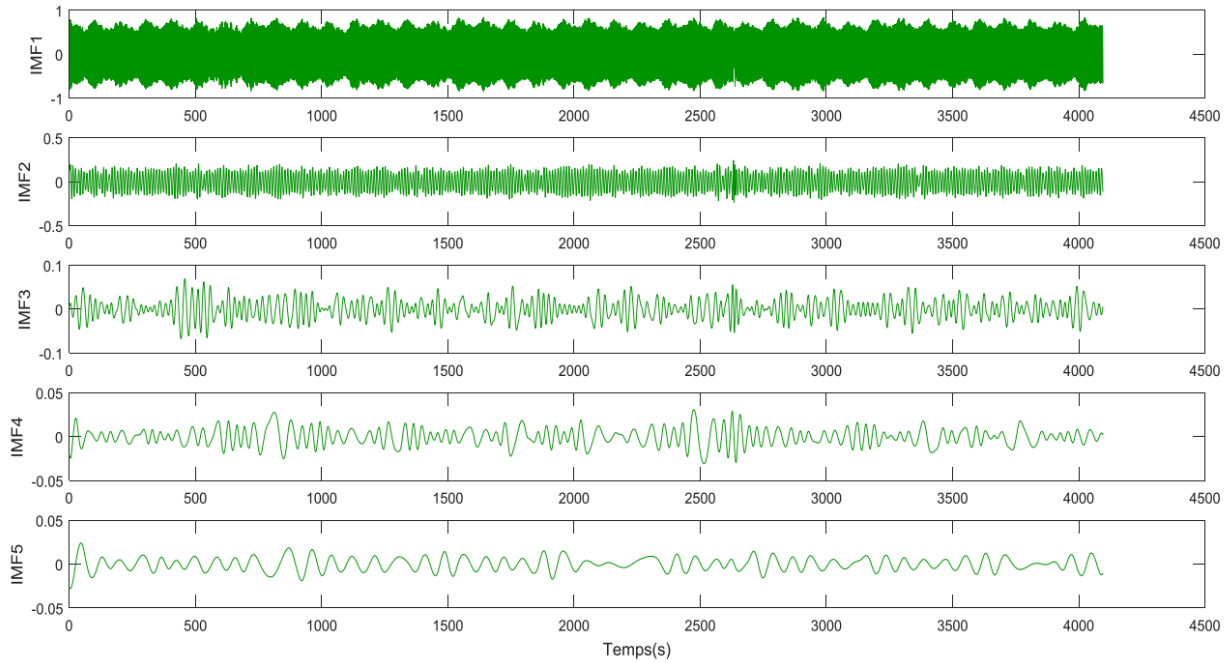


Figure IV.12 IMFs of the inner race fault signal.

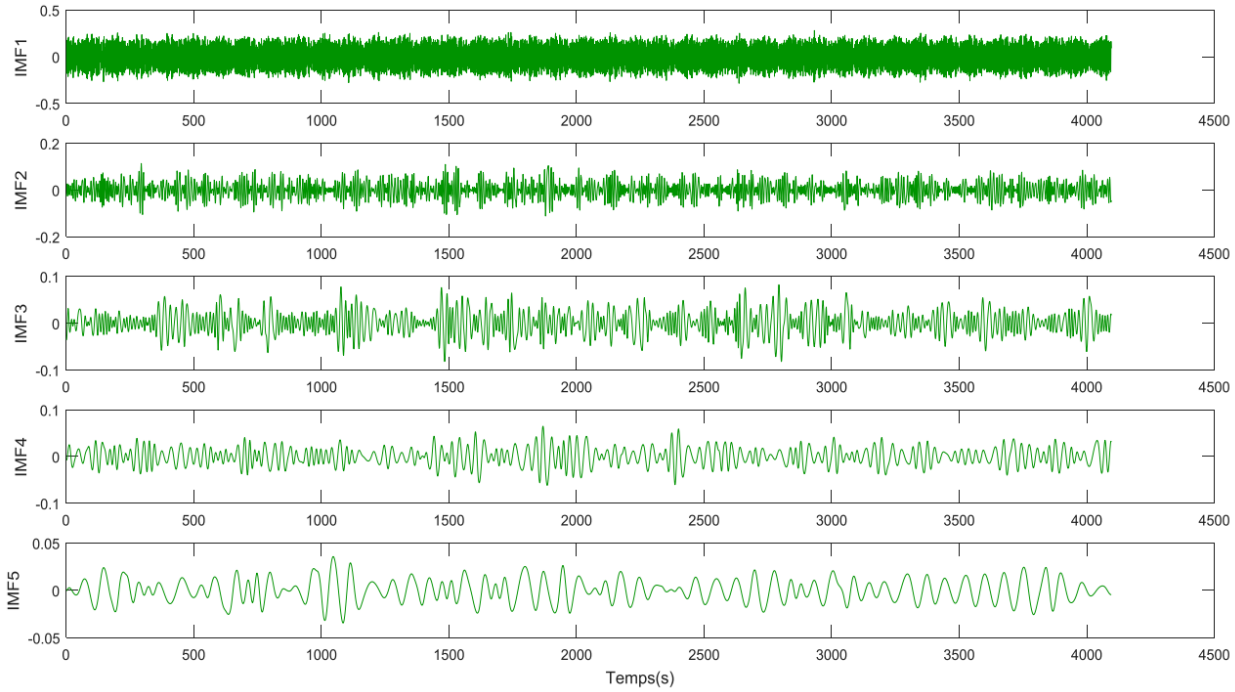


Figure IV.13 IMFs of the outer race fault signal on 6 o'clock position.

The EMD decomposes the signals into several Intrinsic Mode Functions (IMFs) across different frequency bands. Figures IV.11- IV.13 show the first five IMFs of the decomposition for the four bearing signals corresponding respectively to: healthy state, inner race fault and outer race fault, for a fault diameter of 0.178 mm.

IV.6.1 Fault Signature Evaluation via the Hilbert Spectrum

This method involves performing EMD decomposition of the various fault signals, then computing the spectrum of the relevant IMFs (in this case IMF1 and IMF2).

To evaluate the proposed method, measurements were collected at speeds of 1797 rpm (Fr=29.95 Hz) under no-load (0 HP) and 1730 rpm (Fr=28.83Hz) under a load of 3 HP, for different fault diameters (0.178 mm and 0.356 mm.

The data acquisition sampling frequency is 12,000 Hz and the number of samples per signal is 4096 points. This longer record length (compared to the 2000-sample segments used in the FFT analysis of Section IV.5) is selected to provide finer frequency resolution in the Hilbert spectrum, which is particularly important for resolving closely spaced fault frequency sidebands.

The theoretical fault frequencies for these bearing defects are calculated using Equation 0.1. and Equation 0.2. and are summarized in Table IV.5.

Fault Diameter	Fault Type	Motor Load (HP)	Motor Speed (rpm)	Shaft Frequency fr (Hz)	Fault Frequency (Hz)
0.178 mm	Outer Race Fault	0	1797	29.95	107.12
0.356 mm	Outer Race Fault	3	1730	28.83	103.12
0.178 mm	Inner Race Fault	0	1797	29.95	162.42
0.356 mm	Inner Race Fault	3	1730	28.83	156.34

Table IV.5 Bearing fault frequencies.

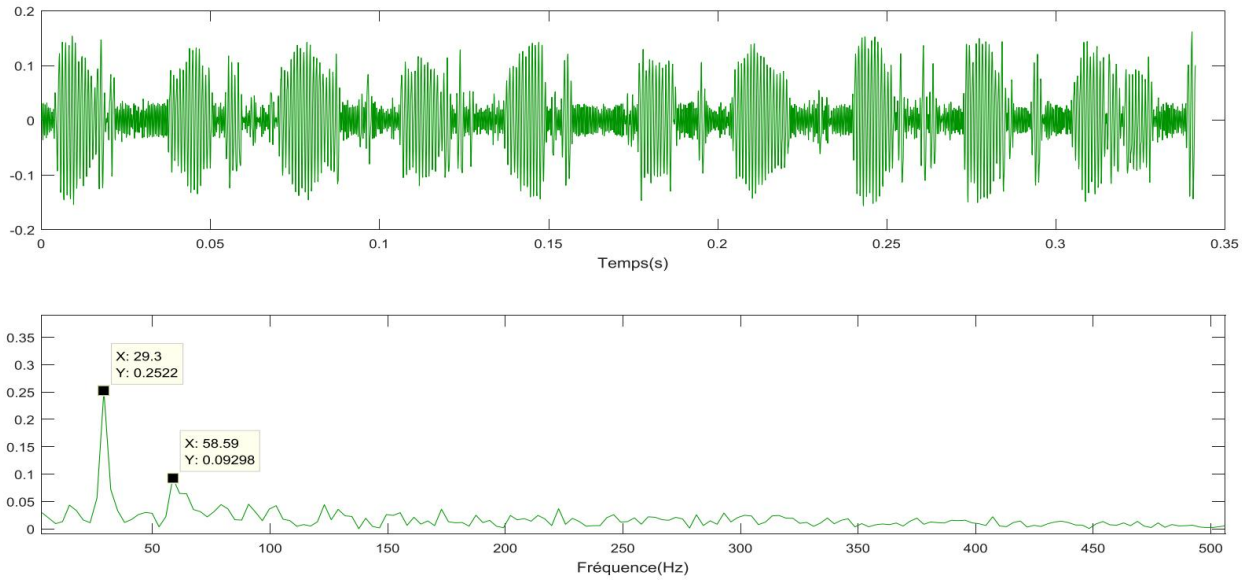


Figure IV.14 Hilbert spectrum of IMF1 for the healthy bearing signal.

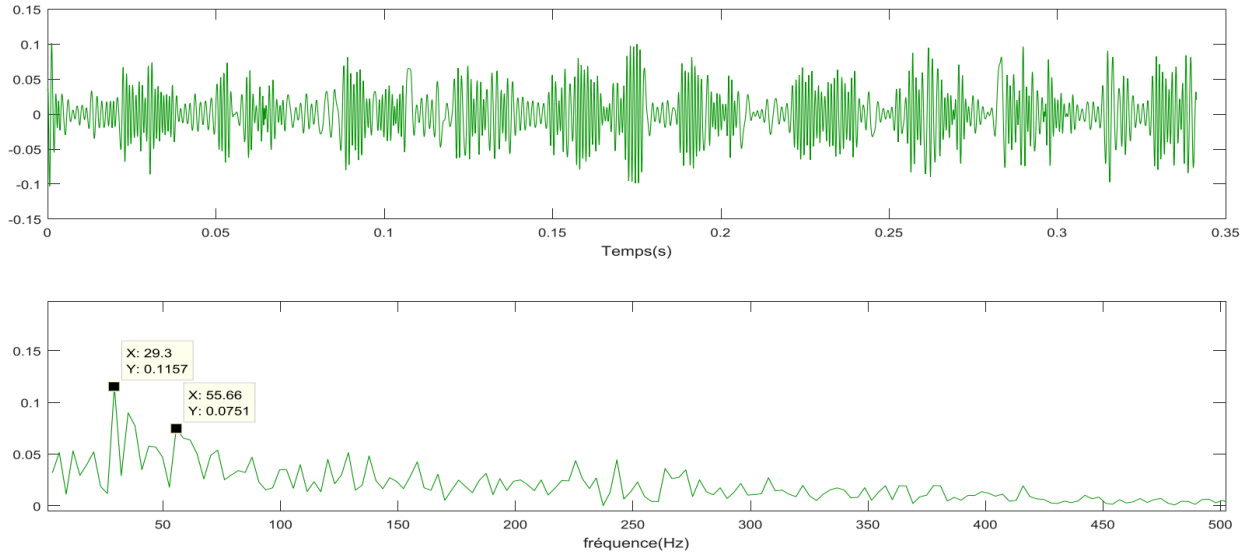


Figure IV.15 Hilbert spectrum of IMF2 for the healthy bearing signal.

Figures IV.14 and IV.15 show the Hilbert spectra of the first two IMFs of the healthy bearing signal. The rotational frequency and its harmonics are clearly readable from the spectra. The complete absence of any fault frequency is observed.

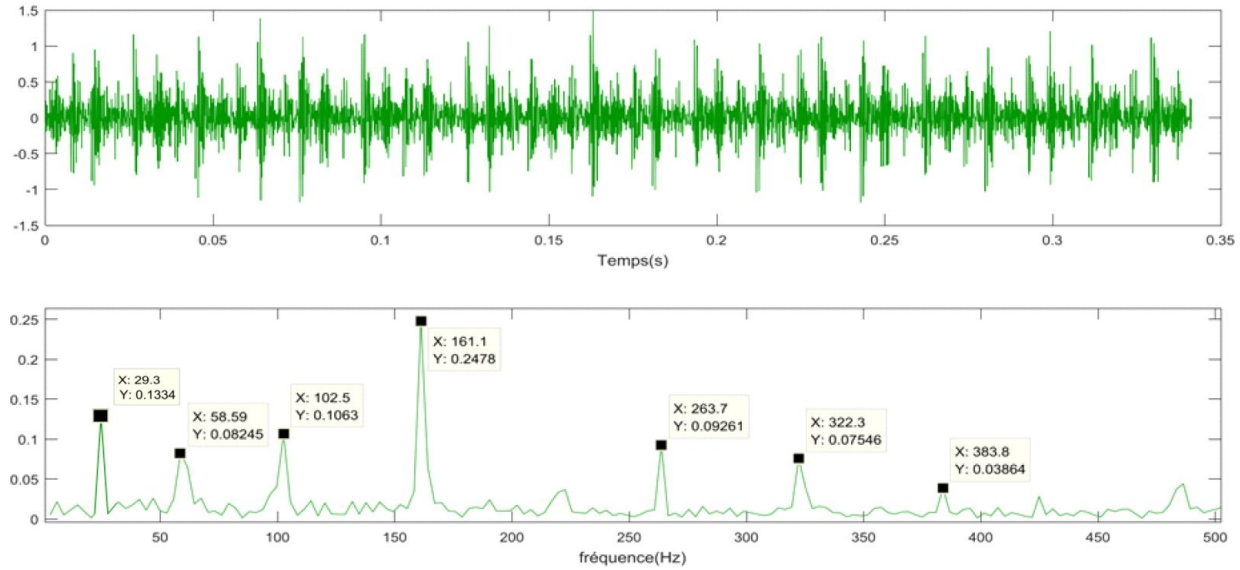


Figure IV.16 Hilbert spectrum of IMF1 for a 0.178 mm inner race fault (no-load).

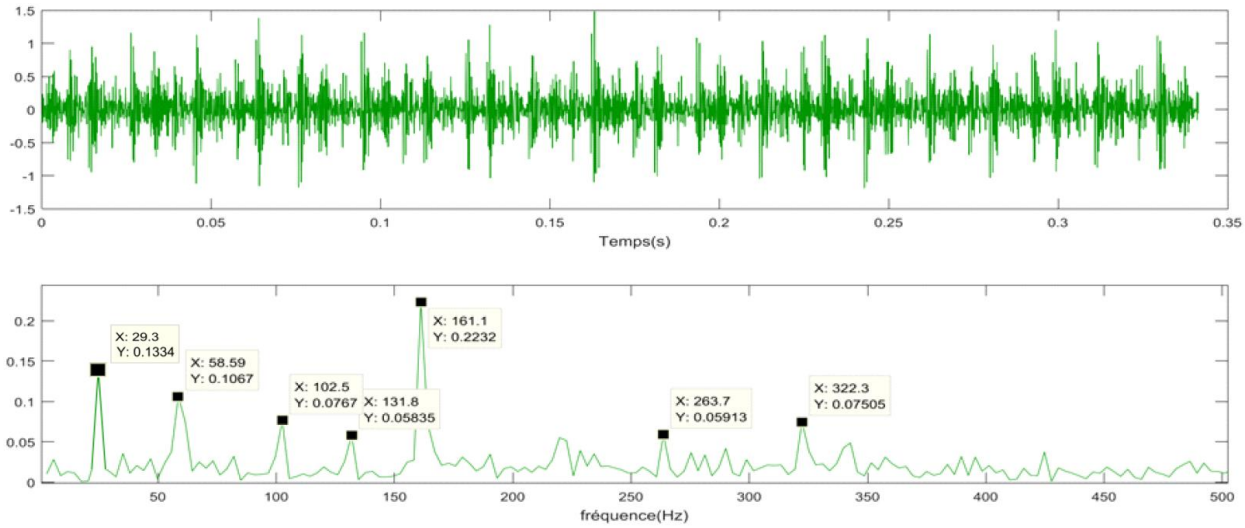


Figure IV.17 Hilbert spectrum of IMF2 for a 0.178 mm inner race fault (no-load).

Figures IV.16 and IV.17 show the Hilbert spectra of the first two IMFs of the bearing signal with a 0.178 mm diameter fault. These figures allow clear identification of the first harmonic of the rotational frequency at 58.6 Hz, the inner race fault frequency at 161.1 Hz, and its harmonics. The fault frequency is surrounded by sidebands resulting from amplitude modulation, with a modulation frequency equal to the shaft rotational frequency.

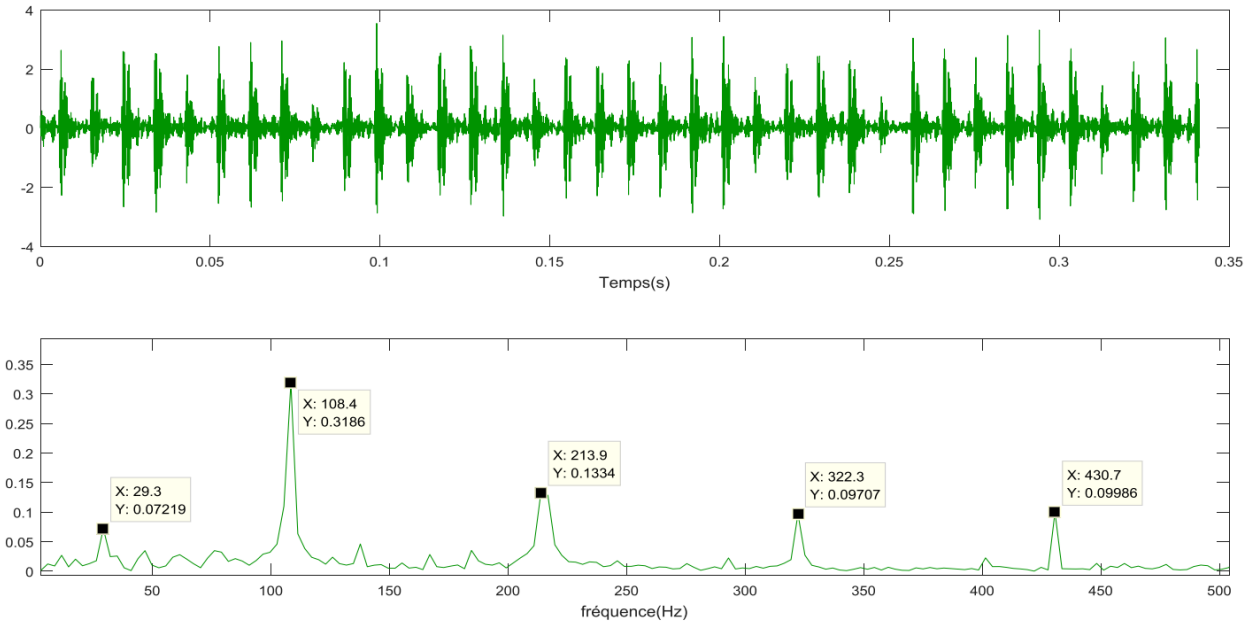


Figure IV.18 Hilbert spectrum of IMF1 for a 0.178 mm outer race fault (no-load- on 6 o'clock position).

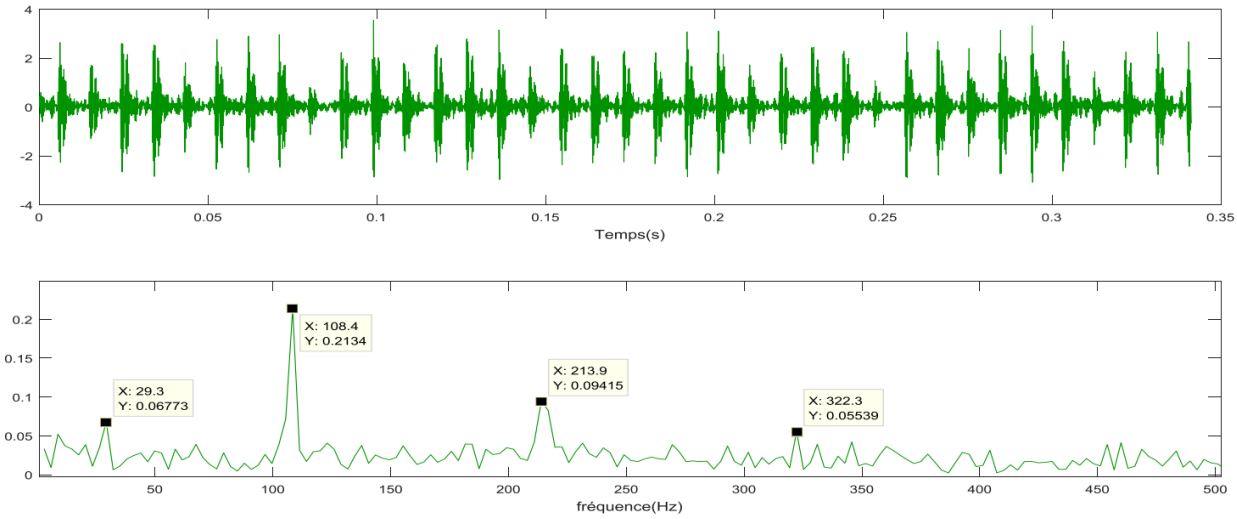


Figure IV.19 Hilbert spectrum of IMF2 for a 0.178 mm outer race fault (no-load on 6 o'clock position).

Figures IV.18 and IV.19 show the Hilbert spectra of the first two IMFs of the outer race fault signal. The rotational frequency at 29.3 Hz and the fault frequency at 108.4 Hz, surrounded by modulation sidebands, are clearly identifiable.

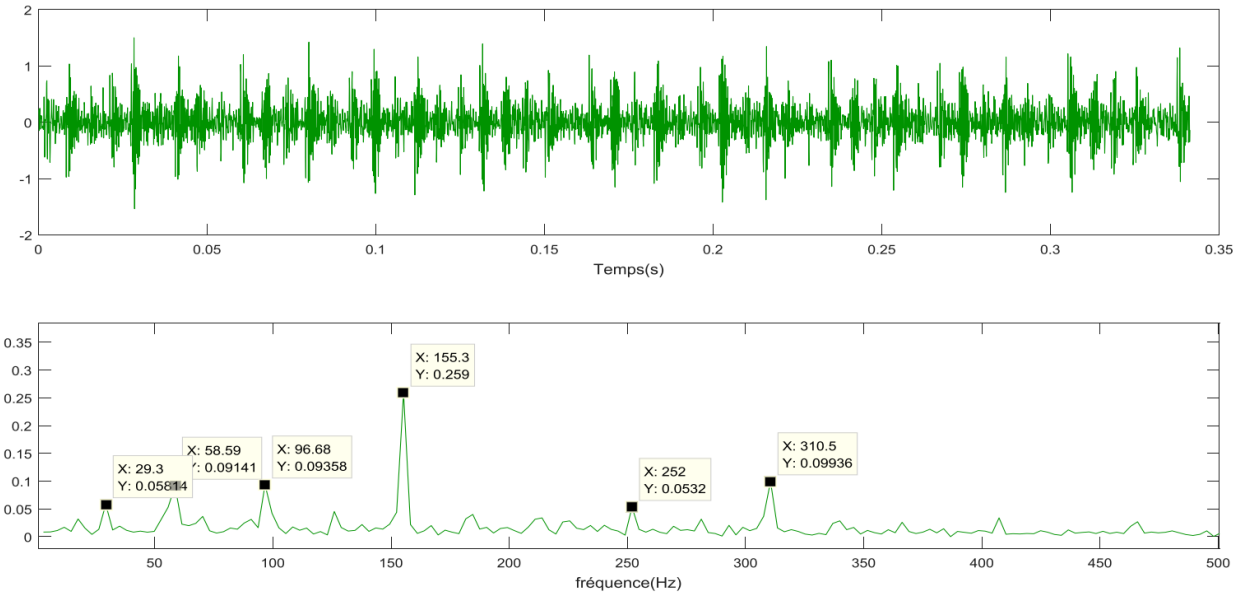


Figure IV.20 Hilbert spectrum of IMF1 for a 0.356 mm inner race fault under 3 HP load.

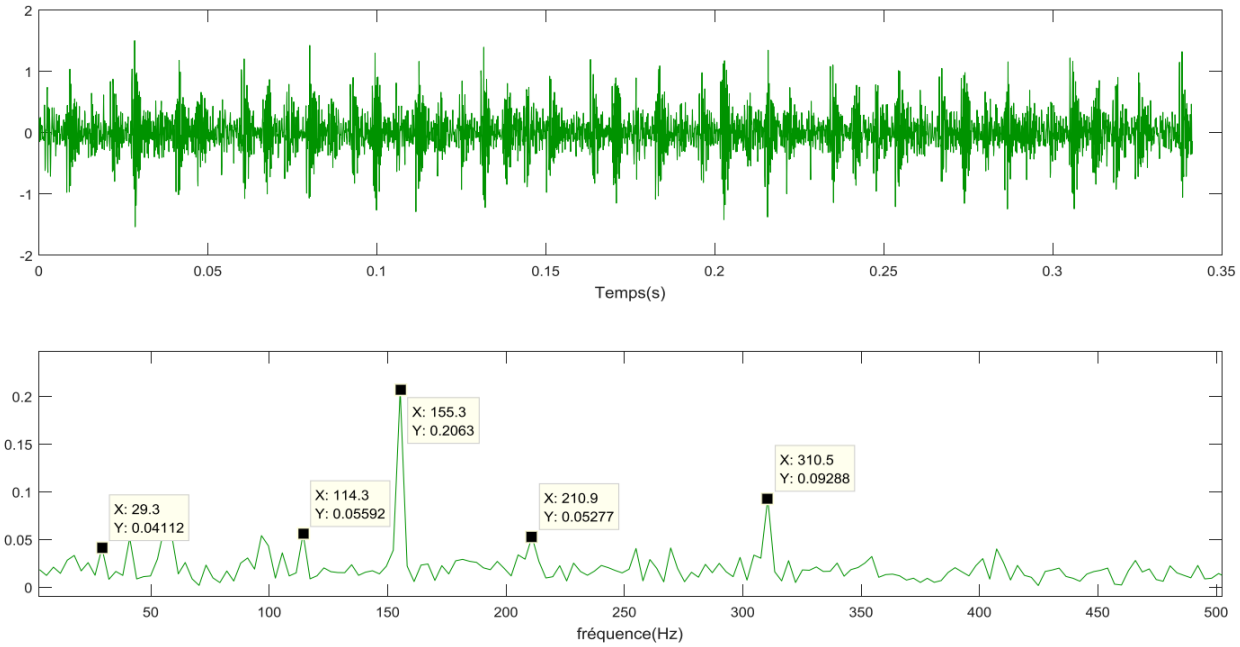


Figure IV.21 Hilbert spectrum of IMF2 for a 0.356 mm inner race fault under 3 HP load.

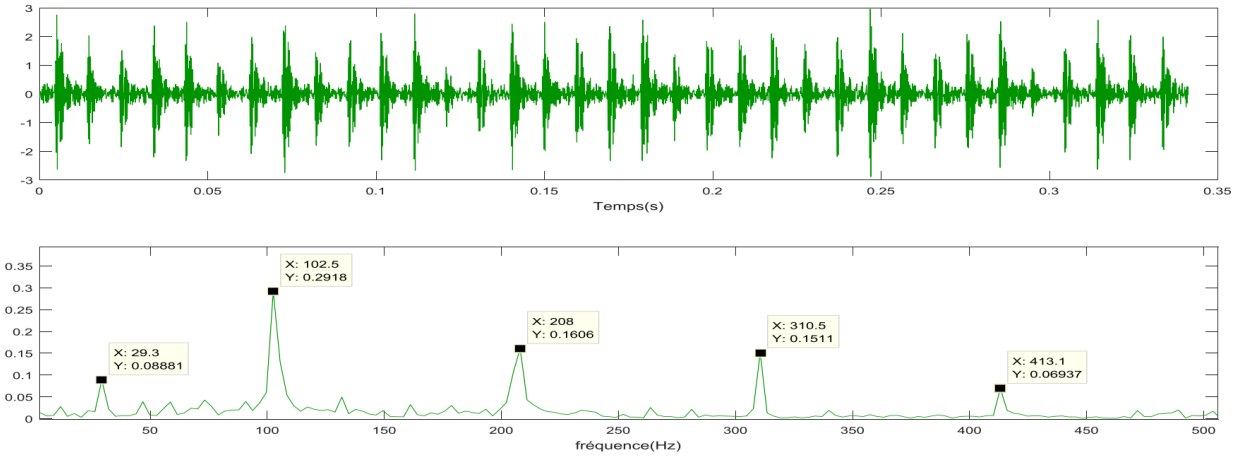


Figure IV.22 Hilbert spectrum of IMF1 for a 0.356 mm outer race fault under 3 HP load on 6 o'clock position.

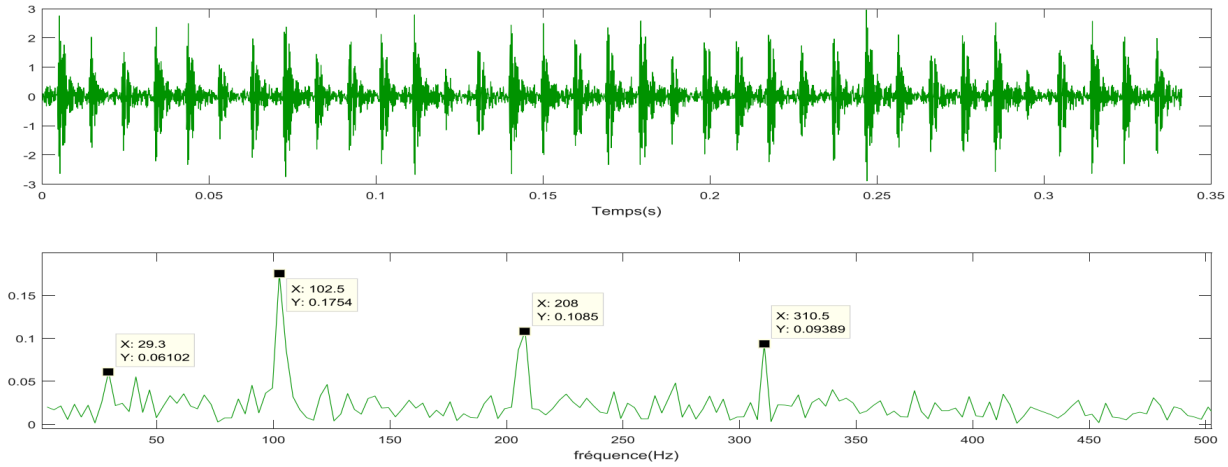


Figure IV.23 Hilbert spectrum of IMF2 for a 0.356 mm outer race fault under 3 HP load on 6 o'clock position.

Figures IV.20- IV.23 show the Hilbert spectra of the first two IMFs for the inner race and outer race faults under a 3 HP load. In both fault cases, the rotational frequency at 29.3 Hz is identified, along with the inner race fault frequency at 155.3 Hz and the outer race fault frequency at 102.5 Hz.

IV.7 Conclusion

In this chapter, two complementary signal processing approaches were applied to real vibration signals acquired from the CWRU bearing test rig for the SKF 6205-2RS JEM bearing under no-load and loaded operating conditions. In the first part, FFT-based spectral analysis successfully identified the outer race fault frequency with a frequency error lower than 1 Hz. The inner race fault was successfully detected under the no-load condition. However, under the 3 HP load condition, the FFT analysis failed to clearly extract or reveal the inner race fault, as the amplitude variation at the corresponding fault frequency remained very small compared with the healthy condition. In the second part, the HHT-based analysis (combining EMD decomposition and Hilbert spectral analysis) was applied to the same signals. The Hilbert spectra of IMF1 and IMF2 revealed the fault-characteristic frequencies, their harmonics, and the amplitude-modulation sidebands spaced at the shaft rotational frequency, under both no-load (1797 rpm) and loaded (1730 rpm, 3 HP) conditions. As summarized in Table IV.6, the HHT provided clearer identification of fault-related spectral features compared to the classical FFT approach, particularly in terms of sideband resolution and harmonic visibility.

Table IV.6 summarizes the results obtained by both methods *FFT and HHT*.

Fault Type	Method	Sidebands visible?	Harmonics visible?	Fault Detection
Inner Race	FFT	No	No	**Partial**
Inner Race	HHT	Yes	Yes	**yes**
Outer Race	FFT	No	No	**yes**
Outer Race	HHT	Yes	Yes	**yes**

Table IV.6. Comparative between FFT and HHT

GENERAL CONCLUSION

This work investigated the application of two signal processing approaches, namely the Fast Fourier Transform (FFT) and the Hilbert–Huang Transform (HHT), to the diagnosis of rolling bearing faults in rotating machinery, with the aim of evaluating their respective diagnostic performances under realistic operating conditions.

First, the industrial context of the study and the main fault categories affecting rotating machinery were presented, together with the theoretical foundations of vibration-based diagnosis and the principal signal analysis techniques used for fault detection.

Subsequently, the mathematical foundations of the Hilbert–Huang Transform were developed, beginning with the Fourier Transform and its limitations in the analysis of non-stationary signals, followed by the Hilbert Transform and the analytic signal framework, and finally the Empirical Mode Decomposition (EMD) algorithm and Hilbert Spectral Analysis (HSA).

The practical part focused on the analysis of real vibration signals extracted from the CWRU database using the SKF 6205-2RS JEM bearing under both no-load and loaded operating conditions. The FFT demonstrated good effectiveness in identifying the outer race fault frequency; however, its capability to clearly detect the inner race fault under loaded conditions remained limited. In contrast, the HHT successfully identified the characteristic fault frequencies, their harmonics, and the associated sidebands under all operating conditions, providing higher spectral resolution and clearer diagnostic signatures than the FFT.

Overall, the experimental results confirm that the Hilbert–Huang Transform constitutes a more effective tool than the Fast Fourier Transform for rolling bearing fault diagnosis under non-stationary and variable-load operating conditions. Its fully adaptive and data-driven nature, combined with its ability to capture intrawave frequency modulation without generating spurious harmonics, makes it particularly suitable for real industrial environments where operating conditions vary and fault signatures may remain subtle.

References

[1] Kumar, S., Raj, K. K., Cirrincione, M., Cirrincione, G., Franzitta, V., & Kumar, R. R. (2024). *A comprehensive review of remaining useful life estimation approaches for rotating machinery. Energies*, 17(22), 5538. https://doi.org/10.3390/en17225538

[2] Chen, J., Lin, C., Peng, D., & Ge, H. (2020). Fault diagnosis of rotating machinery: A review and bibliometric analysis. *IEEE Access*, 8, 224985–225003. https://doi.org/10.1109/ACCESS.2020.3043743

[3] Das, O., Das, D. B., & Birant, D. (2023). Machine learning for fault analysis in rotating machinery: A comprehensive review. *Heliyon*, 9(6), e17584. https://doi.org/10.1016/j.heliyon.2023.e17584

[4] Girdhar, P., & Scheffer, C. (2004). *Practical machinery vibration analysis and predictive maintenance*. Elsevier/Newnes.

[5] [Video]. (n.d.). *Rotating machinery vibration fundamentals* [Video]. YouTube. https://youtu.be/qpOprYh7lck?si=DVq8959jn5de6Gt3

[6] Lei, Y., Lin, J., He, Z., & Zuo, M. J. (2013). A review on empirical mode decomposition in fault diagnosis of rotating machinery. *Mechanical Systems and Signal Processing*, 35(1–2), 108–126. https://doi.org/10.1016/j.ymssp.2012.09.015

[7] Li, J., Zheng, C., Wu, Z., Chen, H., Wang, X.-B., & Yang, Z.-X. (2026). Review of fault diagnosis for rotating machinery: Prior knowledge integration in data-driven methods benefits model interpretability and generalizability. *Mechanical Systems and Signal Processing*, 242, 113623. https://doi.org/10.1016/j.ymssp.2025.113623

[8] Kumar, P., & Tiwari, R. (2024). Additive fault diagnosis techniques in rotor systems: A state-of-the-art review. *Sādhanā*, 49, 207. https://doi.org/10.1007/s12046-024-02543-7

[9] Rezazadeh, N., De Luca, A., & Perfetto, D. (2022). Unbalanced, cracked, and misaligned rotating machines: A comparison between classification procedures throughout the steady-state operation. *Journal of the Brazilian Society of Mechanical Sciences and Engineering*, 44, 450. https://doi.org/10.1007/s40430-022-03750-1

[10] Tavner, P. (2008). Review of condition monitoring of rotating electrical machines. *IET Electric Power Applications*, 2(4), 215–247. https://doi.org/10.1049/iet-epa:20070280

[11] Kafeel, A., Aziz, S., Awais, M., Khan, M. A., Afaq, K., Idris, S. A., Alshazly, H., & Mostafa, S. M. (2021). An expert system for rotating machine fault detection using vibration signal analysis. *Sensors*, 21(22), 7587. https://doi.org/10.3390/s21227587

[12] Chaudhary, A., Thakur, A., & Joshi, I. C. (2025). A review – BearMath: Bearing fault diagnostics using machine learning. *International Journal for Multidisciplinary Research*, 7(2). https://www.ijfmr.com/papers/2025/2/39641.pdf

[13] Vazifehdan, M. A. S., Chalabi, S., & Saadat, S. (2025). Comparative study of classical and deep learning methods for bearing fault diagnosis of electrical machines. In *Proceedings of the IEEE International Symposium on Industrial Electronics (ISIE)* (pp. 1–6). IEEE.

[14] Abdullah, A. T., Hussein, H. M., Sabeeh, R. S., & Hussien, M. J. (2025). A comprehensive review of machine learning algorithms for fault diagnosis and prediction in rotating machinery. *Journal of University of Babylon for Engineering Sciences*, 33(4), 110–127. https://doi.org/10.29196/jubes.v33i4.5891

[15] Garcia, J., Rios-Colque, L., Peña, A., & Rojas, L. (2025). Condition monitoring and predictive maintenance in industrial equipment: An NLP-assisted review of signal processing, hybrid models, and implementation challenges. *Applied Sciences*, 15(10), 5465. https://doi.org/10.3390/app15105465

[16] Ahmad, Z., Nguyen, T., Ahmad, S., Nguyen, C., & Kim, J. (2024). Multireceptive field graph convolutional networks for machine fault diagnosis. *IEEE Transactions on Industrial Electronics*, 71(3), 2956–2965. https://doi.org/10.1109/TIE.2022.3229343

[17] Saeed, M., Khan, M., Habib, A., & Islam, Q. U. (2024). Rolling bearing fault diagnosis under variable conditions using convolutional neural network and transfer learning. *IEEE Access*, 12, 45201–45215. https://doi.org/10.1109/ACCESS.2024.3381234

[18] Kelly, S. G. (1992). *Fundamentals of mechanical vibrations*. McGraw-Hill.

[19] Wowk, V. (1991). *Machinery vibration: Measurement and analysis*. McGraw-Hill.

[20] Bagri, I., Tahiry, K., Hraiba, A., Touil, A., & Mousrij, A. (2024). Vibration signal analysis for intelligent rotating machinery diagnosis and prognosis: A comprehensive systematic literature review. *Vibration*, 7(4), 1013–1062. https://doi.org/10.3390/vibration7040054

[21] Chu, T., Nguyen, T., Yoo, H., & Wang, J. (2024). A review of vibration analysis and its applications. *Heliyon*, 10(5), e26282. https://doi.org/10.1016/j.heliyon.2024.e26282

[22] Wang, K., Xu, Z.-J., Gong, Y., & Du, K.-L. (2022). Mechanical fault prognosis through spectral analysis of vibration signals. *Algorithms*, 15(3), 94. https://doi.org/10.3390/a15030094

[23] Loparo, K. A. (n.d.). *Bearings vibration data set*. Case Western Reserve University Bearing Data Center. https://engineering.case.edu/bearingdatacenter

[24] Al-Badour, F., Sunar, M., & Cheded, L. (2011). Vibration analysis of rotating machinery using time-frequency analysis and wavelet techniques. *Mechanical Systems and Signal Processing*, 25(6), 2083–2101. https://doi.org/10.1016/j.ymssp.2011.01.017

[25] Gupta, P. K. (1984). *Advanced dynamics of rolling elements*. Springer-Verlag.

[26] Mohd Ghazali, M. H., & Rahiman, W. (2021). Vibration analysis for machine monitoring and diagnosis: A systematic review. *Shock and Vibration*, 2021, Article 9469318. https://doi.org/10.1155/2021/9469318

[27] Zhang, K., Chen, P., Yang, M., Song, L., & Xu, Y. (2022). The Harmogram: A periodic impulses detection method and its application in bearing fault diagnosis. *Mechanical Systems and Signal Processing*, 165, 108374. https://doi.org/10.1016/j.ymssp.2021.108374

[28] Li, C., Ge, W., Xu, C., Li, H., & Hu, F. (2024). Analysis on mechanism and characteristic of vibration fault on new large capacity synchronous condenser. *Journal of Physics: Conference Series*, 2771, 012016. https://doi.org/10.1088/1742-6596/2771/1/012016

[29] Scheffer, C., & Girdhar, P. (2004). *Practical machinery vibration analysis and predictive maintenance*. Elsevier/Newnes. ISBN: 978-0-7506-5939-8.

[30] Nguyen, V.-T., & Diep, Q. B. (2025). Vibration-based gearbox fault diagnosis using a multi-scale convolutional neural network with depth-wise feature concatenation. *PLOS ONE*, 20(7), e0324905. https://doi.org/10.1371/journal.pone.0324905

[31] Bently, D. E., & Hatch, C. T. (2002). *Fundamentals of rotating machinery diagnostics*. Bently Pressurized Bearing Press.

[32] Huang, N. E., Shen, Z., Long, S. R., Wu, M. C., Shih, H. H., Zheng, Q., Yen, N.-C., Tung, C. C., & Liu, H. H. (1998). The empirical mode decomposition and the Hilbert spectrum for nonlinear and nonstationary time series analysis. *Proceedings of the Royal Society of London, Series A: Mathematical, Physical and Engineering Sciences*, 454(1971), 903–993. https://doi.org/10.1098/rspa.1998.0193

[33] Huang, N. E., & Wu, Z. (2008). A review on Hilbert-Huang transform: Method and its applications to geophysical studies. *Reviews of Geophysics*, 46, RG2006. https://doi.org/10.1029/2007RG000228

[34] Huang, N. E., Shen, Z., & Long, S. R. (1999). A new view of nonlinear water waves: The Hilbert spectrum. *Annual Review of Fluid Mechanics*, 31, 417–457. https://doi.org/10.1146/annurev.fluid.31.1.417

[35] Wu, Z., & Huang, N. E. (2008). Ensemble empirical mode decomposition: A noise-assisted data analysis method. *Advances in Adaptive Data Analysis*, 1(1), 1–41. https://doi.org/10.1142/S1793536909000047

[36] Randall, R. B., & Antoni, J. (2011). Rolling element bearing diagnostics—A tutorial. *Mechanical Systems and Signal Processing*, 25(2), 485–520. https://doi.org/10.1016/j.ymssp.2010.07.017

[37] Antoni, J. (2007). Cyclostationary by examples. *Mechanical Systems and Signal Processing*, 23(4), 987–1036. https://doi.org/10.1016/j.ymssp.2008.10.010

[38] Cohen, L. (1995). *Time-frequency analysis: Theory and applications*. Prentice-Hall.

[39] Mallat, S. (2009). *A wavelet tour of signal processing: The sparse way* (3rd ed.). Academic Press.

[40] Daubechies, I. (1992). *Ten lectures on wavelets*. SIAM.

[41] Djebaili, A. (2017). *Diagnostic des défauts des roulements par l'analyse de vibration* [Master's thesis, Université Badji Mokhtar Annaba, Algeria].

[42] Augeix, D. (n.d.). Technique de l'ingénieur: Traité génie mécanique — analyse vibratoire. *Techniques de l'Ingénieur*.

[43] Todoran, G., Holonec, R., & Iakab, C. (2008). Discrete Hilbert transform: Numeric algorithms. *Mediamira Science Publisher*, 4, 1–6.

[44] Cexus, J.-C. (2005). *Analyse des signaux non-stationnaires par Transformation de Huang, Opérateur de Teager-Kaiser, et Transformation de Huang-Teager (THT)* [Doctoral dissertation, Université de Rennes 1, France].

[45] Tandon, N., & Choudhury, A. (1999). A review of vibration and acoustic measurement methods for the detection of defects in rolling element bearings. *Tribology International*, 32(8), 469–480. https://doi.org/10.1016/S0301-679X(99)00077-8

[46] Feng, Z., Liang, M., & Chu, F. (2013). Recent advances in time–frequency analysis methods for machinery fault diagnosis: A review with application examples. *Mechanical Systems and Signal Processing*, 38(1), 165–205. https://doi.org/10.1016/j.ymssp.2013.01.017

[47] Harris, T. A., & Kotzalas, M. N. (2006). *Rolling bearing analysis* (5th ed.). CRC Press.